

NUMERICAL SIMULATIONS OF
ASYMPTOTICALLY ADS SPACETIMES

HANS BANTILAN

A DISSERTATION
PRESENTED TO THE FACULTY
OF PRINCETON UNIVERSITY
IN CANDIDACY FOR THE DEGREE
OF DOCTOR OF PHILOSOPHY

RECOMMENDED FOR ACCEPTANCE
BY THE DEPARTMENT OF
PHYSICS
ADVISER: PROFESSOR FRANS PRETORIUS

JUNE 2013

© Copyright by Hans Bantilan, 2013.

All rights reserved.

Abstract

In this dissertation, we introduce a numerical scheme to construct asymptotically anti-de Sitter spacetimes with Lorentzian signature, focusing on cases that preserve five-dimensional axisymmetry. We study the field theories that are dual to these spacetimes by appealing to the AdS/CFT correspondence in the regime where the gravity dual is completely described by Einstein gravity.

The numerical scheme is based on generalized harmonic evolution, and we begin by obtaining initial data defined on some Cauchy hypersurface. For the study described in this dissertation, we use a scalar field to source deviations from pure AdS₅, and obtain data that correspond to highly deformed black holes. We evolve this initial data forward in time, and follow the subsequent ringdown. What is novel about this study is that the initial horizon geometry cannot be considered a small perturbation of the final static horizon, and hence we are probing an initial non-linear phase of the evolution of the bulk spacetime.

On the boundary, we find that the dual CFT stress tensor behaves like that of a thermalized $\mathcal{N} = 4$ SYM fluid. We find that the equation of state of this fluid is consistent with conformal invariance, and that its transport coefficients match those previously calculated for an $\mathcal{N} = 4$ SYM fluid via holographic methods. Modulo a brief transient that is numerical in nature, this matching appears to hold from the initial time onwards.

We transform these solutions computed in global AdS onto a Minkowski piece of the boundary, and examine the temperature of the corresponding fluid flows. Under this transformation, the spatial profile of temperature at the initial time resembles a Lorentz-flattened pancake centered at the origin of Minkowski space. By interpreting the direction along which the data is flattened as the beam-line direction, our initial data can be thought of as approximating a head-on heavy ion collision at its moment of impact.

Acknowledgements

I would very much like to express my gratitude to Frans Pretorius, my research advisor, for his brilliant guidance and kind encouragement, and for keeping my sometimes reckless enthusiasm somehow very much alive. I would also very much like to thank Steve Gubser, for so many great conversations; I almost invariably leave with a deep insight after talking with him, about any topic ranging from how to find static AdS black hole solutions with scalar hair to the correct placement of spring-loaded climbing devices whilst rock-climbing. I would like to thank the people I have met during my years here at Princeton, most of whom have become friends and colleagues. In particular, I am grateful to my erstwhile yet constant officemates Miroslav Hejna, Arijeet Pal, and Bingkan Xue, each of whom has had a significant and lasting impact on my views. I would also like to thank my parents and brothers, who continue to provide a sort of grounding. The simulations presented in this dissertation were run on the **Woodhen** cluster at Princeton University.

To Mama and Papa.

Contents

Abstract	iii
Acknowledgements	iv
List of Tables	ix
List of Figures	x
1 Introduction	1
1.1 Heavy Ion Collisions	5
1.2 General Relativity	7
1.2.1 Einstein Field Equations	8
1.3 Generalized Harmonic Formalism	10
1.3.1 Einstein Field Equations in Generalized Harmonic Form	12
1.3.2 Generalized Harmonic Constraints	13
1.4 ADM Formalism	17
1.4.1 ADM Initial Data	18
1.4.2 Hamiltonian Constraint	20
1.5 Asymptotically Anti-de Sitter Spacetimes	24
1.5.1 AdS ₅ Spacetime	24
1.5.2 Boundary of AdS ₅	26
1.5.3 Asymptotically AdS ₅ Spacetimes	28
1.5.4 Scalar Fields in Asymptotically AdS ₅ Spacetimes	29

2	Numerical Evolution of Asymptotically AdS Spacetimes	33
2.1	Initial Data with Scalar Matter	34
2.2	Evolution Variables and Boundary Conditions	35
2.3	Source Functions	42
2.3.1	Gauge Choice	42
2.3.2	Implementing the Gauge Choice	47
2.3.3	Initializing the 5-metric at $t = 0$	49
2.4	Numerical Solution Methods	50
3	Reconstructing Boundary CFT Observables	53
3.1	The Stress Energy Tensor of the Dual CFT	53
3.2	Hydrodynamic Description of the Boundary CFT	55
3.2.1	Extracting Fluid Variables	55
3.2.2	Extracting Transport Coefficients	58
3.3	Passing to Minkowski Space	60
4	Dynamics of Deformed AdS Black Holes	65
4.1	Convergence Tests	66
4.2	Strong-field Solutions of the Hamiltonian Constraint	69
4.3	Quasinormal Ringing	72
4.3.1	Scalar Spherical Harmonics of the Metric	75
4.3.2	Scalar Spherical Harmonics of the Scalar Field	86
4.4	Dual Boundary CFT	90
4.4.1	Conserved and Traceless CFT Stress Tensor	90
4.4.2	Fluid Variables	97
4.4.3	Transport Coefficients	99
4.4.4	CFT on a Minkowski Piece of the Boundary	106

5 Conclusion	109
5.1 Discussion	109
5.2 Future Work	111
A Boundary Conditions for Linearized Gravitational Perturbations of AdS	112
B Effect of Scalar Backreaction on Metric Fall-off	115
C Finite Difference Stencils	118
Bibliography	119

List of Tables

4.1	The fundamental quasi-normal mode frequencies extracted from a metric variable	77
4.2	The first overtone quasi-normal mode frequencies extracted from a metric variable	77
4.3	The extracted parameters from a fit to a high harmonic quasinormal mode	79
4.4	The fundamental quasi-normal mode frequencies extracted from the scalar field	88
4.5	The first overtone quasi-normal mode frequencies extracted from the scalar field	89
C.1	A representative sample of second order accurate finite difference stencils	118

List of Figures

1.1	The conformal diagram of Minkowski space	31
1.2	The conformal diagram of anti-de Sitter space	32
4.1	The convergence of a representative deformed black hole solution . . .	67
4.2	The independent residuals for a representative deformed black hole solution	68
4.3	The maximum conformal factor vs. maximum amplitude of a repre- sentative scalar matter distribution at $t = 0$	70
4.4	The AdS mass vs. maximum amplitude of a representative scalar mat- ter distribution at $t = 0$	71
4.5	The ratio of proper equatorial to polar circumference of the apparent horizon versus time of a representative solution	73
4.6	The leading-order behavior of a metric variable near the boundary of a representative solution, projected onto the $\mathbb{S}(200)$ scalar harmonic .	80
4.7	The leading-order behavior of a metric variable near the boundary of a representative solution, projected onto the $\mathbb{S}(400)$ scalar harmonic .	81
4.8	The normalized residuals for the $\mathbb{S}(200)$ and $\mathbb{S}(400)$ fits of the leading- order behavior of the metric	82
4.9	The contributions of the $\mathbb{S}(200)$ and $\mathbb{S}(400)$ harmonics to the full leading-order behavior of the metric	83

4.10	The leading-order behavior of the scalar field variable near the boundary of a representative solution	87
4.11	The trace of the boundary stress tensor dual to a representative solution	91
4.12	The divergence of the boundary stress tensor dual to a representative solution	92
4.13	The energy density of the boundary stress tensor dual to a representative solution, the $w_y/w_x = 4$ case	93
4.14	The energy density of the boundary stress tensor dual to a representative solution, the $w_y/w_x = 32$ case	94
4.15	The S^2 component of the boundary stress tensor dual to a representative solution, the $w_y/w_x = 4$ case	95
4.16	The S^2 component of the boundary stress tensor dual to a representative solution, the $w_y/w_x = 32$ case	96
4.17	The velocity field v of the fluid describing the boundary CFT, the $w_y/w_x = 4$ case	100
4.18	The velocity field v of the fluid describing the boundary CFT, the $w_y/w_x = 32$ case	101
4.19	The boundary fluid equation of state at several resolutions	102
4.20	The boundary fluid equation of state at several resolutions, detail . .	102
4.21	The boundary fluid equation of state at the highest resolution with uncertainty	103
4.22	The boundary fluid equation of state at the highest resolution with uncertainty, detail	103
4.23	The mismatch between the CFT stress tensor and the reconstructed hydrodynamic stress tensor with viscous corrections, the $w_y/w_x = 4$ case	104

4.24	The mismatch between the CFT stress tensor and the reconstructed hydrodynamic stress tensor with viscous corrections, the $w_y/w_x = 32$ case	105
4.25	The fluid temperature in Minkowski space	108

Chapter 1

Introduction

It has been hoped since the beginnings of the AdS/CFT correspondence, first formulated in [1–3], that gauge-gravity dualities would eventually be used to relate gravitational calculations to experimentally testable predictions in gauge theory. Over the past several years, there has been a flurry of activity in applying AdS/CFT to problems in high energy and condensed matter physics, which began with the discovery of the strongly-coupled quark-gluon plasma formed in heavy ion collisions. Recent proposals have suggested application to other systems, including those that exhibit superconductivity, the quantum hall effect, and superfluidity. For some review articles see [4–11]. Though conformal field theories (CFTs) cannot model the exact properties of all of these physical phenomena, it is hoped that they nevertheless capture aspects of the essential physics. In the strong coupling limit of the boundary CFT, the duality maps CFT states to bulk gravity configurations in an asymptotically anti-de Sitter (AdS) spacetime, and there are many cases where the latter theory is more tractable than the former. In many if not most of the model problems studied to date, the gravity description has involved black holes; aside from the interesting philosophical questions this poses, the implication is that one needs to study bulk solutions within the strong-field regime of general relativity. In situations where exact solutions are

not known, or perturbative expansions about known solutions are inadequate to capture the non-linear dynamics, numerical solution of the Einstein field equations for an asymptotically AdS spacetime is required.

Numerical relativity has seen significant progress in recent years modeling dynamical, strong-field geometries, though the majority of applications have been to compact object collisions in asymptotically flat spacetimes. For some review articles see [12–15]. The asymptotic structure of AdS is drastically different from that of flat space; in particular the boundary of AdS is time-like and in causal contact with bulk geometric structures, on time scales relevant to the boundary physics. This poses unique challenges for numerical evolution. The majority of existing literature on numerical solution in AdS has focused on black hole formation in spherically-symmetric spacetimes i.e. $1 + 1$ dimensional simulations where the boundary is a single point, significantly simplifying its treatment. This was done in 3 dimensions [16–18], 4 dimensions [19], 5-dimensions [20] and in the general D -dimensional [21, 22] case. A notable exception is a study of colliding shockwaves in 5-dimensional AdS (AdS_5), with application to heavy ion collisions [23] (and see [24, 25] for follow-up studies). Planar symmetry was imposed in two spatial dimensions, reducing the problem to a $2 + 1$ dimensional simulation. Their approach was based on a null (characteristic) evolution scheme which is well-adapted to describing such colliding plane waves. This method simplifies the treatment of the AdS_5 boundary, though is difficult to generalize to situations with less symmetry. A more recent related study of boundary hydrodynamics via numerical solution of the full field equations in the bulk was presented in [26]; though the evolution was effectively $1 + 1$ dimensional, the space-plus-time decomposition, as used here, in principle allows for a straightforward extension to situations with less symmetry.

Inspired by the growing success of gauge/gravity dualities, we are initiating a new program to solve the Einstein field equations in asymptotically AdS_5 spacetimes,

based on the generalized harmonic (GH) evolution scheme presented in [27, 28]. These methods were introduced in the context of asymptotically flat spacetimes, and it turns out to be a rather non-trivial exercise to adapt them to AdS_5 . The main purpose of this dissertation is to describe, in detail, the steps taken towards achieving a stable Cauchy evolution code in spacetimes that are asymptotically AdS_5 . We will focus on a first study, published in [29], where we impose an $SO(3)$ symmetry for simplicity. Since the method we use is based on Cauchy evolution, it should be straightforward to relax this symmetry restriction for future studies, at the expense of computational complexity. As a sample application, we study the quasi-normal ringdown of initial data describing highly distorted black holes formed from scalar field collapse, and extract the stress energy tensor of the dual conformal field theory defined on the $\mathbb{R} \times S^3$ boundary. The $SO(3)$ symmetry we impose here is precisely the one identified in [30–33] to study generalizations of Bjorken flow.

To make more sense of this entire program, the opening discussion in Chapter 1 will begin by motivating the effort in terms of the heavy ion physics it is intended to clarify. This will be followed by a didactic discussion of general relativity, including the GH formulation that we will use to write the Einstein field equations in a manifestly hyperbolic form, and the formulation attributed to Arnowitt, Deser, and Misner (ADM) that we will use to construct initial data based on a conformal decomposition, restricted to time-symmetric initial conditions. We end Chapter 1 with relevant facts about asymptotically AdS_5 spacetimes.

We will begin Chapter 2 by writing down the explicit initial data equation for scalar field matter, since we will be using a scalar field to source deviations from pure AdS_5 . We will then describe an explicit implementation of the GH formalism. Crucial to the stability of this scheme is the asymptotic nature of the so-called *source functions* that in GH evolution are traditionally associated with coordinate degrees of freedom. Here, in contrast to asymptotically flat spacetimes, we will find that

their asymptotic form can *not* be freely specified if the metric deviation is to be non-singular in the approach to the AdS_5 boundary. This and other subtleties related to evolution will be clarified and addressed here. We discretize the field equations using finite difference methods, and the details of the numerical methods that we use to solve the initial data and evolution equations will be discussed.

Each solution we obtain will be a global spacetime that is asymptotically AdS_5 , which we will describe by $(t, r, \chi, \theta, \phi)$ spherical coordinates adapted to its $\mathbb{R} \times S^3$ boundary. The solutions we consider will be axisymmetric in the sense of an $SO(3)$ symmetry that acts to rotate the 2-spheres parametrized by θ, ϕ . In the boundary CFT, we will see that the way in which this symmetry manifests itself hinges on the way we choose to embed Minkowski space in $\mathbb{R} \times S^3$. We will work out this embedding in detail in Chapter 3, where we will also discuss how to reconstruct the boundary CFT stress tensor, as well as how to determine the extent to which this CFT stress tensor behaves hydrodynamically.

Results from a study of highly deformed black holes, their subsequent evolution and ringdown, and the stress tensor of the corresponding states in the dual boundary CFT, will be presented in Chapter 4. First, we will find that we can solve for arbitrarily strong initial data: the initial slice can be made to contain an apparent horizon, and this horizon can be made arbitrarily large by adjusting (for example) the amplitude of the initial scalar field profile. What is novel about the subsequent evolution of this initial data is that the horizon geometry cannot be considered a small perturbation of the final static horizon, and hence we will be probing an initial non-linear phase of the evolution of the bulk spacetime. Shortly after the initial time, the metric can be described by a combination of quasi-normal modes and what appear to be gauge modes. We will find frequencies that are consistent with the linear modes found in perturbative studies of static black holes, and in modes at higher angular number, we will find evidence of non-linear mode-coupling. On the boundary, the

dual CFT stress tensor behaves like that of a thermalized $\mathcal{N} = 4$ super-Yang-Mills (SYM) fluid. We will find that the equation of state $\epsilon = 3P$ of this fluid is consistent with conformal invariance (here, ϵ and P are the rest frame density and pressure of the fluid, respectively), and that its transport coefficients match those previously calculated for an $\mathcal{N} = 4$ SYM fluid via holographic methods. Modulo a brief transient that is numerical in nature, this matching appears to hold from $t = 0$ onwards.

Finally, we will transform solutions computed in global AdS onto a Minkowski piece of the boundary, and examine the temperature of the corresponding fluid flows. Under this transformation, the spatial profile of temperature at the initial time resembles a Lorentz-flattened pancake centered at the origin of Minkowski space. By interpreting the direction along which the data is flattened as the beam-line direction, this initial data can be thought of as an approximate gravity dual description of a head-on heavy ion collision at its moment of impact. We will conclude in Chapter 5 with a summary of our findings and a discussion of future work.

Appendix A, contains a discussion of how our asymptotic metric boundary conditions relate to the boundary conditions derived in [34] for linearized gravitational perturbations on an AdS background that lead to well-defined dynamics. Appendix B contains some technical details on the effect of matter backreaction on the asymptotic metric fall-off, and Appendix C contains a representative sample of the finite difference stencils we use to represent first and second derivatives. Throughout, we use geometric units where Newton's constant G and the speed of light c are set to 1.

1.1 Heavy Ion Collisions

The approach of applying gauge-gravity dualities to real-world experiments was pioneered in heavy ion physics, the leading facility for which is the Relativistic Heavy Ion Collider (RHIC) at the Brookhaven National Laboratory. At RHIC, gold atoms

are boosted to relativistic speeds with Lorentz factors in excess of hundreds, and are collided with a variety of impact parameters. In this dissertation, we will focus on the zero impact parameter case of head-on heavy ion collisions. Following the moment of impact, the constituent quarks and gluons form a thermal state with a peak temperature $T \approx 300 \text{ MeV}$ ¹. The resulting state of matter is called the *quark-gluon plasma*.

The collective motions of this plasma were found to be consistent with a relativistic fluid with very low viscosity[36–39]. In particular, hydrodynamic fits to RHIC data were found to be consistent with a very small ratio of shear viscosity to entropy density $\eta/s \ll 1$. The first attempts to analytically describe the hydrodynamical expansion of this fluid resulted in the *Bjorken flow* model[40]. Letting the head-on collision take place along the x_3 axis, this model is defined by rotational symmetry about the x_3 axis, translation symmetry along the transverse radius x_\perp from the x_3 axis, and boost invariance in the x_3 direction. This boost invariance along x_3 completely fixes the *longitudinal flow* to be $v_3 = x_3/t$ in the Bjorken model, where v_3 is the velocity profile in the x_3 direction and t is the time from impact. Meanwhile, the translational symmetry along x_\perp makes *radial flow* impossible in this model. Of course, in a real quark-gluon plasma, both longitudinal flow and radial flow are present, and as this flow progresses, the plasma expands and cools. Wherever the plasma has cooled sufficiently, its constituents revert back into a gas of hadrons. We can estimate the time scale for this to occur: the radius of a gold atom at rest is approximately 7 fm, so we can expect the plasma to have fully hadronized at times much later than 7 fm/c.

Many of the most interesting heavy ion collision processes are not accessible via perturbative calculations in QCD, and the time evolution of the quark-gluon plasma lies squarely in this class of processes. To get a handle on this system, an alternative

¹For a reference energy scale, note that lattice quantum chromodynamics (QCD) estimates place the critical temperature T_c above which QCD deconfines at about[35] $T_c \approx 170 \text{ MeV}$.

description in terms of gravity is highly desirable. Unfortunately, QCD has no known gravity dual description. Known concrete realizations of the gauge/gravity duality, such as the *AdS/CFT correspondence*, typically involve a quantum field theory with conformal symmetry: a CFT. In the absence of an AdS/QCD correspondence, we will instead take advantage of the AdS/CFT correspondence, which is a conjecture that provides a one-to-one dictionary between a 5-dimensional asymptotically AdS spacetime with an excited state of the conformal field theory $\mathcal{N} = 4$ SYM. To do so, we will “approximate” QCD by a CFT toy model in the form of $\mathcal{N} = 4$ SYM.

Our strategy in this dissertation is as follows: 1) we will first numerically construct the gravity side of the duality, 2) use it to reconstruct the boundary CFT using the AdS/CFT dictionary, 3) then compare the results of this gravity model to real-world quark-gluon plasma flows. Ideally, this comparison should be made using a dual gravity process that results in a dynamical collision, in order to most closely mimic a head-on heavy ion collision while keeping the number of tunable parameters at a minimum. In an ideal gravity model, essentially the only tunable parameters should be the choice of collision participants that would act as proxies for gold atoms, and the choice of speed at which the collision occurs. This dissertation represents a first step towards this goal: we will prepare gravitational initial data that approximately describes a head-on heavy ion collision at its moment of impact, then follow its time evolution according to the Einstein field equations of general relativity.

1.2 General Relativity

General relativity describes the physics of gravity, and is based on the key insight that the effects of gravity are indistinguishable from accelerated motion. This equivalence principle makes it natural to suggest that gravity and acceleration are one and the same phenomenon. The theory of general relativity takes this phenomenon to be

geometric in nature: matter impinges upon the geometry of space and time, and experiences accelerated motion as a consequence of that change in geometry, in a sense that we will now make precise.

1.2.1 Einstein Field Equations

In the theory of general relativity, space-time is a differential manifold M equipped with a metric g . The metric encodes the geometry of the space-time, specifically by enabling us to measure the lengths of local vectors defined on a tangent space T_pM at some point $p \in M$, and the angles between such vectors. Each point $p \in M$ can be locally specified by coordinates x^μ , and each vector in T_pM can be written down in terms of basis vectors $\partial/\partial x^\mu$, whose cotangent vectors dx^μ (or *one-forms*) in T_p^*M are such that $dx^\mu(\partial/\partial x^\nu) = \delta_\nu^\mu$.

In local coordinates, the metric takes the form of a non-degenerate symmetric matrix

$$ds^2 = g_{\mu\nu} dx^\mu dx^\nu \tag{1.1}$$

whose inverse $g^{\mu\nu}$ is such that $g^{\mu\alpha} g_{\alpha\nu} = \delta_\nu^\mu$. Lengths and angles of vectors $v, w \in T_pM$ are determined via an inner product induced by the metric²

$$v^\alpha w_\alpha = g_{\mu\nu} v^\mu w^\nu. \tag{1.2}$$

A vector v is time-like if $v^\alpha v_\alpha < 1$, space-like if $v^\alpha v_\alpha > 1$, and null if $v^\alpha v_\alpha = 0$.

On a differentiable manifold, there are many ways of defining the derivative of vector fields or other tensors such that it is invariant under a change of coordinates $x^\mu \rightarrow x^{\mu'}$. For our purposes, we need only consider one possibility known as the Levi-Civita connection, or metric compatible covariant derivative. It can be defined via its effect on the basis vectors of T_pM . The covariant derivative of $\partial/\partial x^\nu$ in the

²This justifies the line element notation “ ds^2 ” for the metric.

$\partial/\partial x^\mu$ direction is

$$\nabla_{\frac{\partial}{\partial x^\mu}} \frac{\partial}{\partial x^\nu} = \Gamma^\kappa{}_{\mu\nu} \frac{\partial}{\partial x^\kappa}. \quad (1.3)$$

The coefficients $\Gamma^\kappa{}_{\mu\nu}$ are known as the Christoffel symbols, which take the local form³

$$\Gamma^\kappa{}_{\mu\nu} = \frac{1}{2} g^{\kappa\alpha} (g_{\nu\alpha,\mu} - g_{\mu\nu,\alpha} + g_{\alpha\mu,\nu}). \quad (1.4)$$

This covariant derivative allows a notion of curvature that takes the difference between infinitesimally transporting a vector $\partial/\partial x^\mu$ either along $\partial/\partial x^\nu$ then along $\partial/\partial x^\lambda$, or along $\partial/\partial x^\lambda$ then along $\partial/\partial x^\nu$. More concisely,

$$\left(\nabla_{\frac{\partial}{\partial x^\lambda}} \nabla_{\frac{\partial}{\partial x^\nu}} - \nabla_{\frac{\partial}{\partial x^\nu}} \nabla_{\frac{\partial}{\partial x^\lambda}} \right) \frac{\partial}{\partial x^\mu} = R^\kappa{}_{\mu\lambda\nu} \frac{\partial}{\partial x^\kappa}. \quad (1.5)$$

The coefficients $R^\kappa{}_{\mu\lambda\nu}$ are the components of the Riemann curvature tensor, which takes the local form

$$R^\kappa{}_{\mu\lambda\nu} = \Gamma^\kappa{}_{\nu\mu,\lambda} - \Gamma^\kappa{}_{\lambda\mu,\nu} + \Gamma^\kappa{}_{\lambda\beta} \Gamma^\beta{}_{\nu\mu} - \Gamma^\kappa{}_{\nu\beta} \Gamma^\beta{}_{\lambda\mu}, \quad (1.6)$$

whose contraction forms the Ricci tensor

$$R_{\mu\nu} = R^\alpha{}_{\mu\alpha\nu}, \quad (1.7)$$

which can be further contracted to form the Ricci scalar

$$R = g^{\mu\nu} R_{\mu\nu}. \quad (1.8)$$

The Einstein field equations is the relation that couples matter to the geometry of space-time, as encoded in the metric. Writing the stress tensor of matter as $T_{\mu\nu}$,

³Here, we write $\partial f/\partial x^\mu = f_{,\mu}$ for the derivative of f with respect to x^μ .

and the cosmological constant as Λ , the field equations are

$$R_{\mu\nu} - \frac{1}{2}Rg_{\mu\nu} + \Lambda g_{\mu\nu} = 8\pi T_{\mu\nu}. \quad (1.9)$$

These equations can be derived from a variation principle, arising as the Euler-Lagrange equations of the Einstein-Hilbert action with cosmological constant and matter contributions, whose Lagrangian density is simply

$$\mathcal{L} = \frac{1}{16\pi} (R - 2\Lambda) + \mathcal{L}_m. \quad (1.10)$$

This Lagrangian density is consistent with the principle that physics should be independent of a coordinate description, since R and Λ transform as scalars under coordinate transformations $x^\mu \rightarrow x^{\mu'}$, and the Lagrangian density of matter \mathcal{L}_m also does so by construction. In D dimensions, this diffeomorphism invariance of the theory manifests itself as D functions-worth of redundancies in (1.9), which must first be fixed via a choice of coordinates, called a *gauge choice*, before (1.9) can be solved.

1.3 Generalized Harmonic Formalism

Generalized harmonic formalism is based on a choice of coordinates x^μ where each coordinate satisfies a scalar wave equation with a source function H^μ :⁴

$$\square x^\mu = \frac{1}{\sqrt{-g}} \frac{\partial}{\partial x^\alpha} (\sqrt{-g} g^{\alpha\mu}) = -g^{\alpha\beta} \Gamma_{\alpha\beta}^\mu \equiv H^\mu, \quad (1.11)$$

⁴As can be seen from (1.11) H^μ is not a vector in the sense of its properties under a coordinate transformation, rather it transforms as the trace of the metric connection. For more details see [12, 27, 41, 42]. One can introduce additional geometric structure in the form of a background metric and connection to write the GH formalism in terms of “standard” tensorial objects. However, in a numerical evolution one must always choose a concrete coordinate system, and hence the resulting equations that are eventually discretized are the same regardless of the extra mathematical structure introduced at the formal level.

where g is the determinant of the metric, and $\Gamma_{\alpha\beta}^{\mu}$ are the Christoffel symbols. To see why this has proven to be so useful for Cauchy evolution, where a solution for the metric $g_{\mu\nu}$ is solved for given data at some initial Cauchy hypersurface supplemented by boundary conditions at spatial infinity, let us begin by rewriting the field equations (1.9) in trace-reversed form

$$R_{\mu\nu} = \bar{T}_{\mu\nu}, \quad (1.12)$$

where

$$\bar{T}_{\mu\nu} = -\frac{2}{2-D}\Lambda_d g_{\mu\nu} + 8\pi \left(T_{\mu\nu} - \frac{1}{D-2} T^{\alpha}{}_{\alpha} g_{\mu\nu} \right) \quad (1.13)$$

When viewed as a set of second-order differential equations for the metric $g_{\mu\nu}$, the field equations in the form (1.12) do not have any well-defined mathematical character (namely hyperbolic, elliptic or parabolic), and in fact are ill-posed. Fixing this character requires choosing a coordinate system. Cauchy evolution is well-posed if and only if the evolution equations are strongly hyperbolic, and a well-known way to arrive at a set of strongly hyperbolic equations is to impose *harmonic coordinates*, namely (1.11) with $H^{\mu} = 0$. Specifically, this condition (and its gradient) can be substituted into the field equations to yield a wave equation for the principal part of each metric element, $g^{\alpha\beta}\partial_{\alpha}\partial_{\beta}g_{\mu\nu} + \dots = 0$, where the ellipses denote lower order terms.

One potential problem with harmonic coordinates, in particular in a highly dynamical, strong-field spacetime evolved via a Cauchy scheme, is that beginning from a well-defined initial data surface $t = \text{const.}$ which is everywhere space-like, there is no guarantee that t , subject to the harmonic condition, will remain time-like throughout the spacetime as evolution proceeds. If $\partial/\partial t$ becomes null or space-like at a point, standard numerical techniques will break down. A solution to this, first suggested in [41], is to make use of source functions (as originally introduced in [43]). Note that *any* spacetime in *any* coordinate system can be written in GH form; the cor-

responding source functions are simply obtained by evaluating the definition (1.11). Thus, trivially, if there is a well-behaved, non-singular coordinate chart that covers a given spacetime, then there is a GH description of it. The difficulty in a Cauchy evolution is that this chart is not known *a-priori*, and the source functions H^μ must be treated as independent dynamical fields. Finding a well-behaved coordinate chart then amounts to supplementing the Einstein field equations with a set of evolution equations for H^μ .

1.3.1 Einstein Field Equations in Generalized Harmonic Form

We begin by writing out the left-hand side of 1.12 explicitly

$$\begin{aligned}
R_{\mu\nu} &= \Gamma^\alpha_{\nu\mu,\alpha} - \Gamma^\alpha_{\alpha\mu,\nu} + \Gamma^\alpha_{\alpha\beta}\Gamma^\beta_{\nu\mu} - \Gamma^\alpha_{\nu\beta}\Gamma^\beta_{\alpha\mu} \\
&= -\frac{1}{2}g^{\alpha\beta}g_{\mu\nu,\alpha\beta} + g^{\alpha\beta}g_{\beta(\mu,\nu)\alpha} + \frac{1}{2}g^{\alpha\beta}_{,\alpha}(g_{\alpha\beta,\nu} - g_{\nu\mu,\beta} + g_{\beta\nu,\mu}) \\
&\quad - (\log \sqrt{-g})_{,\mu\nu} + (\log \sqrt{-g})_{,\beta}\Gamma^\beta_{\mu\nu} - \Gamma^\alpha_{\nu\beta}\Gamma^\beta_{\alpha\mu}.
\end{aligned} \tag{1.14}$$

We now use the fact that

$$H^\nu \equiv \square x^\nu = g^{\alpha\nu}\Gamma^\beta_{\alpha\beta} + g^{\alpha\nu}_{,\alpha}$$

or equivalently

$$H_\mu \equiv g_{\mu\nu}H^\nu = \Gamma^\beta_{\mu\beta} + g_{\mu\nu}g^{\alpha\nu}_{,\alpha} = \Gamma^\beta_{\mu\beta} - g^{\alpha\beta}g_{\mu\beta,\alpha}. \tag{1.15}$$

Computing the covariant derivative of (1.15) and comparing to (1.14) reveals that⁵

$$\begin{aligned}
H_{(\mu,\nu)} &= (\log \sqrt{-g})_{,\mu\nu} - g^{\alpha\beta}{}_{,(\nu} g_{\mu)\beta,\alpha} - g^{\alpha\beta} g_{\beta(\mu,\nu)\alpha} \\
&= -R_{\mu\nu} - \frac{1}{2} g^{\alpha\beta} g_{\mu\nu,\alpha\beta} - \Gamma^\alpha{}_{\nu\beta} \Gamma^\beta{}_{\alpha\mu} - g^{\alpha\beta}{}_{,(\mu} g_{\nu)\alpha,\beta} \\
&\quad + (\log \sqrt{-g})_{,\beta} \Gamma^\beta{}_{\mu\nu} + \frac{1}{2} g^{\alpha\beta}{}_{,\alpha} (g_{\alpha\beta,\nu} - g_{\nu\mu,\beta} + g_{\beta\nu,\mu}) \\
&= -R_{\mu\nu} - \frac{1}{2} g^{\alpha\beta} g_{\mu\nu,\alpha\beta} - \Gamma^\alpha{}_{\nu\beta} \Gamma^\beta{}_{\alpha\mu} - g^{\alpha\beta}{}_{,(\mu} g_{\nu)\alpha,\beta} + H_\alpha \Gamma^\alpha{}_{\mu\nu}. \quad (1.16)
\end{aligned}$$

The field equations in GH form are the trace-reversed field equations (1.12) with $\bar{T}_{\mu\nu}$ given by (1.13) and $R_{\mu\nu}$ given by (1.16):

$$\begin{aligned}
&-\frac{1}{2} g^{\alpha\beta} g_{\mu\nu,\alpha\beta} - g^{\alpha\beta}{}_{,(\mu} g_{\nu)\alpha,\beta} - H_{(\mu,\nu)} + H_\alpha \Gamma^\alpha{}_{\mu\nu} - \Gamma^\alpha{}_{\beta\mu} \Gamma^\beta{}_{\alpha\nu} \\
&= \frac{2}{3} \Lambda_5 g_{\mu\nu} + 8\pi \left(T_{\mu\nu} - \frac{1}{3} T^\alpha{}_\alpha g_{\mu\nu} \right). \quad (1.17)
\end{aligned}$$

The full GH system of equations thus consist of (1.17), together with the relevant evolution equations for the matter, and a set of equations for the source functions which we write symbolically as

$$\mathcal{L}^\mu[H^\mu] = 0. \quad (1.18)$$

1.3.2 Generalized Harmonic Constraints

Even though H^μ are now treated as independent functions, we are only interested in the *subset* of solutions to the expanded system (1.17),(1.18) that satisfy the GH constraints (1.11). Introducing

$$C^\mu \equiv H^\mu - \square x^\mu, \quad (1.19)$$

⁵Here we have used the identity $(\log \sqrt{-g})_{,\alpha} = \Gamma^\beta{}_{\alpha\beta}$.

we seek solutions to (1.17),(1.18) for which $C^\mu = 0$. It is thus in our interests to determine the conditions under which a Cauchy evolution satisfies $C^\mu = 0$ for all time.

To do this, first notice that an equivalent way of obtaining (1.17) from (1.12) is to subtract $\nabla_{(\mu}C_{\nu)}$ from $R_{\mu\nu}$, so that

$$R_{\mu\nu} - \nabla_{(\mu}C_{\nu)} - \bar{T}_{\mu\nu} = 0. \quad (1.20)$$

The effect of this subtraction becomes obvious when we rewrite the Ricci tensor, as we have done in (1.14), explicitly in terms of $\square x^\mu$

$$R_{\mu\nu} = -\frac{1}{2}g^{\alpha\beta}g_{\mu\nu,\alpha\beta} - g^{\alpha\beta}{}_{,(\mu}g_{\nu)\alpha,\beta} - \nabla_{(\mu}\square x_{\nu)} - \Gamma^\alpha{}_{\beta\mu}\Gamma^\beta{}_{\alpha\nu}. \quad (1.21)$$

We see that the subtraction of $\nabla_{(\mu}C_{\nu)}$ is simply designed to replace the $\nabla_{(\mu}\square x_{\nu)}$ term in $R_{\mu\nu}$ by an equivalent $\nabla_{(\mu}H_{\nu)}$ term. We also see that a solution of the Einstein field equations (1.12) is also a solution of (1.20), as long as the constraints $C^\mu = 0$ are satisfied.

Taking the divergence of (1.20), we obtain

$$\nabla^\mu R_{\mu\nu} - \frac{1}{2}\square C_\nu - \frac{1}{2}\nabla^\mu\nabla_\nu C_\mu - \nabla^\mu\bar{T}_{\mu\nu} = 0. \quad (1.22)$$

To simplify this expression, we use the contraction of the second Bianchi identity

$$\begin{aligned} \nabla^\mu R_{\mu\nu} &= \frac{1}{2}\nabla_\nu R \\ &= \frac{1}{2}\nabla_\nu [\nabla^\alpha C_\alpha + \bar{T}^\alpha{}_\alpha] \\ &= \frac{1}{2}\nabla_\nu\nabla^\alpha C_\alpha + \frac{1}{2}\nabla_\nu\bar{T}^\alpha{}_\alpha \end{aligned} \quad (1.23)$$

and the definition (1.5) of the Riemann tensor to commute covariant derivatives

$$\begin{aligned}
\nabla^\mu \nabla_\nu C_\mu &= g^{\alpha\beta} \nabla_\alpha \nabla_\nu C_\beta \\
&= g^{\alpha\beta} [\nabla_\nu \nabla_\alpha C_\beta - R^\gamma_{\beta\alpha\nu} C_\gamma] \\
&= \nabla_\nu \nabla^\alpha C_\alpha + C^\mu R_{\mu\nu} \\
&= \nabla_\nu \nabla^\alpha C_\alpha + C^\mu [\nabla_{(\mu} C_{\nu)} + \bar{T}_{\mu\nu}] \\
&= \nabla_\nu \nabla^\alpha C_\alpha + C^\mu \nabla_{(\mu} C_{\nu)} + C^\mu \bar{T}_{\mu\nu}.
\end{aligned} \tag{1.24}$$

The divergence (1.22) of the GH evolution equations then becomes

$$\square C_\nu = -C^\mu \nabla_{(\mu} C_{\nu)} - C^\mu \bar{T}_{\mu\nu} - 2\nabla^\mu \bar{T}_{\mu\nu} + \nabla_\nu \bar{T}^\alpha{}_\alpha. \tag{1.25}$$

To simplify this expression, we note from (1.13) that

$$\nabla^\mu \bar{T}_{\mu\nu} = 8\pi \left(-\frac{1}{D-2} \nabla_\nu \bar{T}^\alpha{}_\alpha \right) \tag{1.26}$$

and that

$$\nabla_\nu \bar{T}^\alpha{}_\alpha = 8\pi \left(-\frac{2}{D-2} \nabla \bar{T}^\alpha{}_\alpha \right). \tag{1.27}$$

We thus see that the last two terms in (1.25) exactly cancel, revealing that C^μ satisfies the following hyperbolic equation:

$$\square C_\nu = -C^\mu \nabla_{(\mu} C_{\nu)} - C^\mu \bar{T}_{\mu\nu}. \tag{1.28}$$

For a Cauchy evolution of the system (1.17),(1.18), we need to specify initial data in the form

$$g_{\mu\nu}|_{t=0}, \quad \partial_t g_{\mu\nu}|_{t=0}, \tag{1.29}$$

subject to the constraints

$$C^\mu|_{t=0} = 0, \quad \partial_t C^\mu|_{t=0} = 0. \quad (1.30)$$

Thus, if we imagine (analytically) solving (1.17),(1.18) using initial data satisfying (1.30) supplemented with boundary conditions consistent with $C^\mu = 0$ on the boundary for all time, then (1.28) implies that C^μ will remain zero in the interior for all time.

At the level of the discretized equations, however, C^μ is only zero up to truncation error. This is not *a priori* problematic: numerically one only ever gets a solution approximating the continuum solution to within truncation error. However, experience with asymptotically-flat simulations suggest that in some strong-field spacetimes, equation (1.28) for C^μ admits exponentially growing solutions (the so-called “constraint-violating modes”). At any practical resolution, this severely limits the amount of physical time for which an accurate solution to the desired $C^\mu = 0$ Einstein equations can be obtained. In asymptotically flat spacetimes, supplementing the GH harmonic equations with *constraint-damping* terms as introduced in [44] suppresses these unwanted solutions. Anticipating similar problems in AAdS spacetimes, and that constraint damping will similarly help, we add the same terms to (1.17), and arrive at the final form of our evolution equations

$$\begin{aligned} & - \frac{1}{2} g^{\alpha\beta} g_{\mu\nu,\alpha\beta} - g^{\alpha\beta}{}_{,(\mu} g_{\nu)\alpha,\beta} - H_{(\mu,\nu)} + H_\alpha \Gamma^\alpha{}_{\mu\nu} - \Gamma^\alpha{}_{\beta\mu} \Gamma^\beta{}_{\alpha\nu} \\ & - \kappa (2n_{(\mu} C_{\nu)} - (1 + P) g_{\mu\nu} n^\alpha C_\alpha) \\ & = \frac{2}{3} \Lambda_5 g_{\mu\nu} + 8\pi \left(T_{\mu\nu} - \frac{1}{3} T^\alpha{}_\alpha g_{\mu\nu} \right). \end{aligned} \quad (1.31)$$

Here, the unit time-like one-form n_μ is defined as in (1.34), and the constraint damping parameters $\kappa \in (-\infty, 0]$ and $P \in [-1, 0]$ are arbitrary constants. In all simulations⁶ described here, we use $\kappa = -10$ and $P = -1$.

1.4 ADM Formalism

The ADM formalism [45] is based on a choice of coordinates that naturally arises from a *space + time* decomposition which casts the metric in the form

$$g_{\mu\nu}dx^\mu dx^\nu = -\alpha^2 dt^2 + \gamma_{ij}(dx^i + \beta^i dt)(dx^j + \beta^j dt). \quad (1.32)$$

Here, the latin indices i, j only sum over the spatial coordinates, and γ_{ij} is the d -metric induced on a space-like hypersurface Σ_t at some t . Its pullback to the full $D = d + 1$ dimensional spacetime takes the local form

$$\gamma_{\mu\nu} = g_{\mu\nu} + n_\mu n_\nu. \quad (1.33)$$

where

$$n_\mu = -\alpha \partial_\mu t \quad (1.34)$$

is the unit time-like one-form normal to the Σ_t hypersurface. In this formalism, the coordinate degrees of freedom are fixed via a choice of the lapse function α and the shift vector β^i that appear in (1.32). Again performing the pullback to the full $D = d + 1$ dimensional spacetime, the lapse and shift are geometrically related to the time-like vector $\partial/\partial t$ and the unit normal n_μ by

$$\left(\frac{\partial}{\partial t}\right)^\mu = \beta^\mu + \alpha n^\mu. \quad (1.35)$$

⁶We did not perform any systematic survey by varying κ or P , though with a little experimentation found the exact value of κ was not too important to achieve effective constraint damping, though we found that it was important to keep P close to -1 .

In this dissertation, we will use the ADM formalism to set initial data on $\Sigma_{t=0}$.

1.4.1 ADM Initial Data

Initial data for Cauchy evolution of the Einstein field equations (1.9) is not freely specifiable, but is subject to a set of D constraint equations: the $D - 1$ non-trivial components of the momentum constraints, and the Hamiltonian constraint. There are many conceivable ways of finding initial data that are consistent with these constraints; here, we adapt to AAdS₅ spacetimes the traditional ADM-based conformal decomposition approach often used in asymptotically flat spacetimes. See [46] for a recent review. To simplify the treatment here, we restrict initial data to a moment of time symmetry, and we use a scalar field to source non-trivial deviations from pure vacuum AdS₅.

Specifying time symmetric initial data is equivalent to demanding that the extrinsic curvature of the initial $t = 0$ slice $\Sigma_{t=0}$ vanishes. The extrinsic curvature of a constant t slice Σ_t of the spacetime is defined as

$$K_{\mu\nu} = -\gamma_{\mu}^{\alpha} \gamma_{\nu}^{\beta} \nabla_{(\alpha} n_{\beta)} = -\frac{1}{2} \mathcal{L}_n \gamma_{\mu\nu}. \quad (1.36)$$

The ADM constraint equations are found by contracting the Einstein field equations (1.9) once with the unit normal to the Σ_t surfaces n_{μ} , giving the local form

$$n^{\nu} \left(R_{\mu\nu} - \frac{1}{2} R g_{\mu\nu} - 8\pi T_{\mu\nu} \right) = 0. \quad (1.37)$$

To see how (1.37) is related to the GH constraints (1.30), one can show (see for e.g. [42]) that if (1.30) are satisfied, then (1.37) will also be satisfied at $t = 0$. To see this, notice from (1.20) that

$$R = g^{\alpha\beta} \nabla_{\alpha} C_{\beta} + 8\pi \left(-\frac{2}{D-2} T^{\alpha}_{\alpha} \right). \quad (1.38)$$

This can be used to rewrite (1.20) as

$$R_{\mu\nu} - \frac{1}{2}Rg_{\mu\nu} - 8\pi T_{\mu\nu} - \nabla_{(\mu}C_{\nu)} + \frac{1}{2}g^{\alpha\beta}\nabla_{\alpha}C_{\beta}g_{\mu\nu} = 0, \quad (1.39)$$

whose projection onto the Σ_t surface with normal one-form n_{μ} gives

$$n^{\nu} \left(R_{\mu\nu} - \frac{1}{2}Rg_{\mu\nu} - 8\pi T_{\mu\nu} \right) - \frac{1}{2}n^{\nu}\partial_{\nu}C_{\mu} - \frac{1}{2}n^{\nu}\Gamma^{\alpha}_{\mu\nu}C_{\alpha} + \frac{1}{2}n^{\nu} (g^{\alpha\beta}g_{\mu\nu} - g^{\alpha}_{\mu}g^{\beta}_{\nu}) \nabla_{\alpha}C_{\beta} = 0, \quad (1.40)$$

which implies the desired result.

Conversely, the relation (1.40) shows that if (1.37) are satisfied at $t = 0$ together with $C^{\mu}|_{t=0} = 0$ (this latter condition is satisfied trivially, since $H^{\mu}|_{t=0}$ is computed by substituting (1.29) into (1.11)), then $\partial_t C^{\mu}|_{t=0} = 0$. Thus, the problem of obtaining initial data that satisfy (1.30) is entirely equivalent to solving (1.37). Note that the new constraint damping terms that were introduced in (1.31) are homogeneous in C_{μ} , and hence do not alter these relations between solutions of the Einstein evolution equations and ADM constraints with those of the corresponding GH equations. The exception is that the constraint propagation equation (1.28) picks up additional terms, again homogeneous in C_{μ} (see for example [44]).

The $D - 1$ spatial components of (1.37) form the momentum constraints

$$D_{\nu}K^{\mu\nu} - \gamma^{\mu\nu}D_{\nu}K = 8\pi j^{\mu}, \quad (1.41)$$

where $D_{\mu} = \gamma_{\mu}^{\nu}\nabla_{\nu}$ is the derivative operator intrinsic to Σ_t , and

$$j^{\mu} = -T_{\alpha\beta}n^{\alpha}\gamma^{\mu\beta} \quad (1.42)$$

is the momentum of any matter in the spacetime. Time symmetry $K_{\mu\nu}|_{t=0} = 0$ requires that in order for (1.41) to be satisfied, it suffices to arrange for the matter

momentum density j^μ to vanish everywhere on $\Sigma_{t=0}$. The remaining time component of (1.37) forms the Hamiltonian constraint, the solution of which is the subject of the following.

1.4.2 Hamiltonian Constraint

The temporal component of (1.37) forms the Hamiltonian constraint

$${}^{(4)}R + K^2 - K_{\mu\nu}K^{\mu\nu} - 2\Lambda_5 = 16\pi\rho_E, \quad (1.43)$$

where ${}^{(4)}R$ is the Ricci scalar of the geometry intrinsic to Σ_t , and

$$\rho_E = T_{\mu\nu}n^\mu n^\nu \quad (1.44)$$

is the energy density on Σ_t . At a moment of time symmetry (1.43) simplifies to

$${}^{(4)}R - 2\Lambda_5 = 16\pi\rho_E. \quad (1.45)$$

Following the conformal approach, we will solve this equation by requiring that our spatial 4-metric γ_{ij} be conformal to the 4-metric $\hat{\gamma}_{ij}$ of a spatial slice of vacuum AdS₅

$$\begin{aligned} \gamma_{ij} &= \zeta^2 \hat{\gamma}_{ij} \\ \gamma^{ij} &= \zeta^{-2} \hat{\gamma}^{ij}, \end{aligned} \quad (1.46)$$

for some positive smooth function ζ on $\Sigma_{t=0}$ with boundary condition $\zeta|_{\partial\Sigma} = 1$.

The conformal form of the Hamiltonian constraint can be obtained as follows. First, consider the difference between the Christoffel symbols of the Levi-Civita connection D associated with the 4-metric γ_{ij} , and those of the Levi-Civita connection \hat{D} associated with the conformal 4-metric $\hat{\gamma}_{ij}$. The difference of these Christoffel symbols

forms the components of a tensor

$$C^k{}_{ij} = \Gamma_{ij}^k - \hat{\Gamma}_{ij}^k. \quad (1.47)$$

Given a tensor of rank (p, q) , the components of its covariant derivatives with respect to different connections are related in terms of $C^k{}_{ij}$ by

$$D_k T^{i_1 \dots i_p}{}_{j_1 \dots j_q} = \hat{D}_k T^{i_1 \dots i_p}{}_{j_1 \dots j_q} + \sum_{r=1}^{r=p} C^{i_r}{}_{ka} T^{\dots a \dots}{}_{j_1 \dots j_q} - \sum_{r=1}^{r=q} C^a{}_{kj_r} T^{i_1 \dots i_p}{}_{\dots a \dots}, \quad (1.48)$$

where D_i is the covariant derivative with respect to γ_{ij} , and \hat{D}_i is the covariant derivative with respect to $\hat{\gamma}_{ij}$.

Direct computation also reveals that the $C^k{}_{ij}$ components can be expressed as

$$C^k{}_{ij} = \frac{1}{2} \gamma^{kl} \left(\hat{D}_i \gamma_{lj} + \hat{D}_j \gamma_{il} - \hat{D}_l \gamma_{ij} \right). \quad (1.49)$$

Using (1.46), we can replace γ_{ij} and γ^{ij} in (1.49) with their corresponding expressions in terms of the conformal objects ζ , $\hat{\gamma}_{ij}$, and $\hat{\gamma}^{ij}$, giving

$$\begin{aligned} C^k{}_{ij} &= \frac{1}{2} \zeta^{-2} \hat{\gamma}^{kl} \left(\hat{D}_i (\zeta^2 \hat{\gamma}_{lj}) + \hat{D}_j (\zeta^2 \hat{\gamma}_{il}) - \hat{D}_l (\zeta^2 \hat{\gamma}_{ij}) \right) \\ &= \frac{1}{2} \zeta^{-2} \hat{\gamma}^{kl} \left(\hat{\gamma}_{lj} \hat{D}_i \zeta^2 + \hat{\gamma}_{il} \hat{D}_j \zeta^2 - \hat{\gamma}_{ij} \hat{D}_l \zeta^2 \right) \\ &= \frac{1}{2} \zeta^{-2} \left(\delta^k{}_j \hat{D}_i \zeta^2 + \delta^k{}_i \hat{D}_j \zeta^2 - \hat{\gamma}_{ij} \hat{\gamma}^{kl} \hat{D}_l \zeta^2 \right) \\ &= \delta^k{}_j \hat{D}_i \ln \zeta + \delta^k{}_i \hat{D}_j \ln \zeta - \hat{\gamma}^{kl} \hat{D}_l \ln \zeta \hat{\gamma}_{ij} \end{aligned} \quad (1.50)$$

where in the last line we have used the relation $\hat{D}_j \ln \zeta = \frac{1}{n} \zeta^{-n} \hat{D}_j \zeta^n$. A useful contraction can be computed by noting that $\hat{\gamma}^{ij} \hat{\gamma}_{ij} = \delta^i{}_i = 4$, so

$$\begin{aligned} C^k{}_{kj} &= \hat{D}_j \ln \zeta + 4 \hat{D}_j \ln \zeta - \hat{D}_j \ln \zeta \\ &= 4 \hat{D}_j \ln \zeta. \end{aligned} \quad (1.51)$$

Taking the definition for the Riemann curvature components (1.5) which we repeat here for some vector field with components V^i

$${}^{(4)}R^k{}_{lij}V^l = (D_i D_j - D_j D_i) V^k. \quad (1.52)$$

Tracing over its first and third indices, we can express the result in terms of \hat{D} using (1.48) to see that ${}^{(4)}R$ and ${}^{(4)}\hat{R}$ are related by

$${}^{(4)}R_{ij} = {}^{(4)}\hat{R}_{ij} + \hat{D}_k C^k{}_{ij} - \hat{D}_i C^k{}_{kj} + C^k{}_{ij} C^l{}_{lk} - C^k{}_{ia} C^a{}_{kj}. \quad (1.53)$$

Using (1.50) and (1.51), we can now eliminate all occurrences of $C^k{}_{ij}$ in (1.53), in favor of conformal objects

$$\begin{aligned} {}^{(4)}R_{ij} &= {}^{(4)}\hat{R}_{ij} + \left(2\hat{D}_i \hat{D}_j \ln \zeta - \hat{\gamma}^{kl} \hat{D}_k \hat{D}_l \ln \zeta \hat{\gamma}_{ij} \right) - \left(4\hat{D}_i \hat{D}_j \ln \zeta \right) \\ &\quad + \left(\delta^k{}_j \hat{D}_i \ln \zeta + \delta^k{}_i \hat{D}_j \ln \zeta - \hat{\gamma}^{kl} \hat{D}_l \ln \zeta \hat{\gamma}_{ij} \right) \left(4\hat{D}_k \ln \zeta \right) \\ &\quad - \left(\delta^k{}_a \hat{D}_i \ln \zeta + \delta^k{}_i \hat{D}_a \ln \zeta - \hat{\gamma}^{kl} \hat{D}_l \ln \zeta \hat{\gamma}_{ia} \right) \\ &\quad \left(\delta^a{}_j \hat{D}_k \ln \zeta + \delta^a{}_k \hat{D}_j \ln \zeta - \hat{\gamma}^{al} \hat{D}_l \ln \zeta \hat{\gamma}_{kj} \right) \\ &= {}^{(4)}\hat{R}_{ij} - 2\hat{D}_i \hat{D}_j \ln \zeta - \hat{\gamma}^{kl} \hat{D}_k \hat{D}_l \ln \zeta \hat{\gamma}_{ij} \\ &\quad + 2\hat{D}_i \ln \zeta \hat{D}_j \ln \zeta - 2\hat{\gamma}^{kl} \hat{D}_k \ln \zeta \hat{D}_l \ln \zeta \hat{\gamma}_{ij}. \end{aligned} \quad (1.54)$$

The relation between scalar curvatures ${}^{(4)}R$ and ${}^{(4)}\hat{R}$ can be found by contracting (1.54) with respect to $\gamma^{ij} = \zeta^{-2}\hat{\gamma}^{ij}$, and using

$$\begin{aligned}
\hat{D}_i \hat{D}_j \ln \zeta &= \hat{D}_i \left(\zeta^{-1} \hat{D}_j \zeta \right) \\
&= \zeta^{-1} \hat{D}_i \hat{D}_j \zeta + \hat{D}_i \zeta^{-1} \hat{D}_j \zeta \\
&= \zeta^{-1} \hat{D}_i \hat{D}_j \zeta - \zeta^{-2} \hat{D}_i \zeta \hat{D}_j \zeta \\
&= \zeta^{-1} \hat{D}_i \hat{D}_j \zeta - \hat{D}_i \ln \zeta \hat{D}_j \ln \zeta,
\end{aligned} \tag{1.55}$$

so that we have

$$\begin{aligned}
{}^{(4)}R &= \gamma^{ij} ({}^{(4)}R)_{ij} \\
&= \zeta^{-2} \hat{\gamma}^{ij} \left({}^{(4)}\hat{R}_{ij} - 2\hat{D}_i \hat{D}_j \ln \zeta - \hat{\gamma}^{kl} \hat{D}_k \hat{D}_l \ln \zeta \hat{\gamma}_{ij} \right. \\
&\quad \left. + 2\hat{D}_i \ln \zeta \hat{D}_j \ln \zeta - 2\hat{\gamma}^{kl} \hat{D}_k \ln \zeta \hat{D}_l \ln \zeta \hat{\gamma}_{ij} \right) \\
&= \zeta^{-2} \left({}^{(4)}\hat{R} - 2\hat{\gamma}^{kl} \hat{D}_k \hat{D}_l \ln \zeta - \hat{\gamma}^{kl} 4\hat{D}_k \hat{D}_l \ln \zeta \right. \\
&\quad \left. + 2\hat{\gamma}^{kl} \hat{D}_k \ln \zeta \hat{D}_l \ln \zeta - 2\hat{\gamma}^{kl} 4\hat{D}_k \ln \zeta \hat{D}_l \ln \zeta \right) \\
&= \zeta^{-2} \left({}^{(4)}\hat{R} - 6\hat{\gamma}^{kl} \hat{D}_k \hat{D}_l \ln \zeta - 6\hat{\gamma}^{kl} \hat{D}_k \ln \zeta \hat{D}_l \ln \zeta \right) \\
&= \zeta^{-2} ({}^{(4)}\hat{R}) - 6\zeta^{-3} \hat{\gamma}^{kl} \hat{D}_k \hat{D}_l \zeta.
\end{aligned} \tag{1.56}$$

The Hamiltonian constraint (1.45) can then be expressed as

$${}^{(4)}\hat{R} - 6\zeta^{-1} \hat{\gamma}^{\alpha\beta} \hat{D}_\alpha \hat{D}_\beta \zeta - \zeta^2 2\Lambda_5 = 16\pi\zeta^2 \rho_E, \tag{1.57}$$

where \hat{D}_α is the covariant derivative operator compatible with $\hat{\gamma}_{\mu\nu}$, and ${}^{(4)}\hat{R}$ is the corresponding Ricci scalar. ${}^{(4)}\hat{R}$ is readily computed from the spatial part of the AdS₅ metric (1.59), giving a constant ${}^{(4)}\hat{R} = -12/L^2 = 2\Lambda_5$. This lets us rewrite (1.57) as

$$\hat{\gamma}^{\alpha\beta} \hat{D}_\alpha \hat{D}_\beta \zeta - \frac{1}{3} \Lambda_5 \zeta + \frac{1}{3} (\Lambda_5 + 8\pi\rho_E) \zeta^3 = 0. \tag{1.58}$$

Notice that the Hamiltonian constraint (1.58) does not contain the lapse function α ; this is consistent with the understanding that unlike a specification of the lapse α , which encodes the manner in which data evolves away from the initial slice, the Hamiltonian constraint may only set data intrinsic to the initial slice itself. Furthermore, by restricting our attention to conformally AdS initial data, we have written this Hamiltonian constraint as a non-linear elliptic equation for the conformal factor ζ . This equation can be solved once the matter content is specified, which amounts to specifying ρ_E .

1.5 Asymptotically Anti-de Sitter Spacetimes

1.5.1 AdS₅ Spacetime

The metric of AdS₅ is the maximally symmetric vacuum solution of the Einstein field equations (1.9) in $D = 5$ dimensions, with a negative cosmological constant $\Lambda \equiv \Lambda_5 < 0$. In terms of the global coordinates $x^\mu = (t, r, \chi, \theta, \phi)$ that cover the whole spacetime, this solution is

$$\begin{aligned} ds^2 &\equiv \hat{g}_{\mu\nu} dx^\mu dx^\nu \\ &= -f(r) dt^2 + \frac{1}{f(r)} dr^2 + r^2 d\Omega_3^2 \end{aligned} \tag{1.59}$$

where we have defined $f(r) = 1 + r^2/L^2$ for convenience. Here, $d\Omega_3^2 = d\chi^2 + \sin^2 \chi (d\theta^2 + \sin^2 \theta d\phi^2)$ is the metric of the 3-sphere parametrized by angles χ, θ, ϕ , and L is the AdS radius of curvature, related to the cosmological constant by $\Lambda_5 = -(D-1)(D-2)/(2L^2) = -6/L^2$. We are free to set the AdS length scale L , which is the scale with respect to which all other lengths are measured. In the code we set $L = 1$, though we will continue to explicitly display L in all of the following, unless otherwise indicated.

Due to the significance of the AdS₅ boundary in the context of AdS/CFT, it is useful to introduce a “compactified” radial coordinate ρ so that the boundary is at a finite ρ . We choose

$$r = \frac{\rho}{1 - \rho/\ell}, \quad (1.60)$$

where ℓ is an arbitrary compactification scale, independent of the AdS length scale L , such that the AdS₅ boundary is reached when $\rho = \ell$. In our code and in all of the following, we set $\ell = 1$, though note that this scale is implicitly present since ρ has dimensions of length. Transforming to the ρ coordinate, the metric (1.59) takes the form:

$$ds^2 = \frac{1}{(1 - \rho)^2} \left(-\hat{f}(\rho) dt^2 + \frac{1}{\hat{f}(\rho)} d\rho^2 + \rho^2 d\Omega_3^2 \right) \quad (1.61)$$

where $\hat{f}(\rho) = (1 - \rho)^2 + \rho^2/L^2$.

AdS₅ can also be described as the universal cover of the hyperboloid X^A in $\mathbb{R}^{4,2}$ defined by the locus

$$-(X^{-1})^2 - (X^0)^2 + \sum_{i=1}^{i=4} (X^i)^2 = -L^2. \quad (1.62)$$

This space has symmetry group $SO(4,2)$ whose transformations preserve the quadratic form (1.62). The metric of AdS₅ is then the metric $\hat{g}_{\mu\nu}$ induced on the above hyperboloid from the flat metric \hat{G}_{AB} of an $\mathbb{R}^{4,2}$ ambient space. Here the metric \hat{G}_{AB} is simply given by $\hat{G} = \text{diag}(-1, -1, 1, 1, 1, 1)$. The hyperboloid can be more efficiently described in terms of embedding coordinates x^μ defined by a set of embedding functions $X^A(x^\mu)$, so that the induced metric $\hat{g}_{\mu\nu}$ on the hyperboloid is

$$\hat{g}_{\mu\nu} = \left(\frac{\partial X^A}{\partial x^\mu} \right) \left(\frac{\partial X^B}{\partial x^\nu} \right) \hat{G}_{AB}. \quad (1.63)$$

The global coordinates $x^\mu = (t, r, \chi, \theta, \phi)$ can then be thought of as corresponding to a choice of embedding functions

$$\begin{aligned}
X^{-1} &= \sqrt{r^2 + L^2} \cos(t/L) \\
X^0 &= \sqrt{r^2 + L^2} \sin(t/L) \\
X^1 &= r \sin \chi \sin \theta \sin \phi \\
X^2 &= r \sin \chi \sin \theta \cos \phi \\
X^3 &= r \sin \chi \cos \theta \\
X^4 &= r \cos \chi.
\end{aligned} \tag{1.64}$$

Notice that $t = 0$ and $t = 2\pi L$ are identified on the hyperboloid, so that there are closed time-like curves in this space. AdS_5 is defined as the hyperboloid's universal cover precisely to remove these closed time-like curves. This universal cover is obtained by unwrapping the S^1 parametrized by t on the hyperboloid, which would then run from $-\infty$ to ∞ in AdS_5 .

1.5.2 Boundary of AdS_5

The boundary of AdS_5 differs dramatically from that of asymptotically flat spacetimes. To see this, let us first remember how the analogous story unfolds in the familiar setting of Minkowski space, whose metric in polar coordinates $\eta_{\mu\nu} dx^\mu dx^\nu = -dt^2 + dr^2 + r^2 d\Omega^2$ can be rewritten through a series of coordinate transformations $u_\pm = t \pm r$, $\tilde{u}_\pm = \arctan u_\pm = (T \pm R)/2$ to read

$$ds^2 = \frac{1}{4 \cos^2 u_+ \cos^2 u_-} (-dT^2 + dR^2 + \sin^2 R d\Omega^2). \tag{1.65}$$

Through this conformal compactification, the infinite region $t \in (-\infty, \infty)$, $r \in [0, \infty)$ is mapped to the interior of a compact region defined by $|T \pm R| < \pi$. Given that

T is a time-like coordinate and $R > 0$ is a space-like coordinate, this region is the triangle $T \in [-\pi, \pi]$, $R \in [0, \pi]$ in the T, R plane—see Fig. 1.1. Consequently, the boundary consists of the two null surfaces of future/past null infinity, meeting at spatial infinity. Spatial infinity in Minkowski space is thus not in causal contact with its interior. Notice that the geometry of Minkowski space is conformal to a patch $T \in [-\pi, \pi]$ of the Einstein static universe.

The conformal compactification of AdS_5 is achieved⁷ by the spatial coordinate transformation $r/L = \tan R$, which brings its metric (1.59) into the form

$$ds^2 = \frac{L^2}{\cos^2 R} (-dt^2 + dR^2 + \sin^2 R d\Omega_3^2) \quad (1.66)$$

where the infinite region $r \in [0, \infty]$ is mapped to the interior of a compact region $R \in [0, \pi/2]$ —see Fig. 1.2. This halved range of R implies that anti-de Sitter space is conformal to one-half of the Einstein static universe. More crucially, we have not rescaled the time coordinate t in this compactification. The important consequence is a spatial infinity that runs along the t direction: it is time-like and thus causally connected to the interior.

A proper treatment of the AdS boundary is crucial to a solution of the Cauchy problem in an asymptotically AdS spacetime. Without some specification of boundary conditions at time-like infinity, only a small wedge to the causal future of an initial space-like foliation can be solved for. This is in contrast with asymptotically Minkowski spacetimes, where the specification of initial data on a slice that reaches spatial infinity is sufficient to evolve the entire interior. Such an approach to initial data is not useful in the asymptotically AdS case, particularly in problems that are relevant to AdS/CFT: for these problems, the time-like boundary must be included as part of the spacetime.

⁷In practice, we compactify using (1.60), but for the current didactic discussion we choose the compactification that most closely resembles its Minkowski space analog.

1.5.3 Asymptotically AdS₅ Spacetimes

An asymptotically AdS₅ (AAdS₅) spacetime is one that shares the boundary structure of AdS₅. In particular, it must have $SO(4, 2)$ as its asymptotic symmetry group. To write down the asymptotics of the fields in such a spacetime, let us decompose the metric by writing

$$g_{\mu\nu} = \hat{g}_{\mu\nu} + h_{\mu\nu} \tag{1.67}$$

where $h_{\mu\nu}$ is the deviation of the full metric $g_{\mu\nu}$ from the metric $\hat{g}_{\mu\nu}$ of AdS₅.

The matter-free asymptotics of $h_{\mu\nu}$ corresponding to an AAdS₅ spacetime were found in [47], by requiring that these deviations $h_{\mu\nu}$ satisfy boundary conditions at spatial infinity that i) are invariant under the $SO(4, 2)$ symmetry group of AdS₅, ii) include the AdS-Schwarzschild black hole metric as a special case, and iii) yield finite values for the conserved quantities associated with the spacetime. These results are also consistent with the Fefferman-Graham construction when mapped to a Poincaré patch [48] of AdS (see Appendix A). To describe these conditions, we begin by noting that a typical generator ξ^μ of $SO(4, 2)$ has components with asymptotics

$$\begin{aligned} \xi^m &= \mathcal{O}(1) \\ \xi^r &= \mathcal{O}(r) \\ \xi_{,r}^m &= \mathcal{O}(r^{-3}) \\ \xi_{,r}^r &= \mathcal{O}(1), \end{aligned} \tag{1.68}$$

where the index m denotes the non-radial coordinates (t, χ, θ, ϕ) . Since we need to ensure that $SO(4, 2)$ is an asymptotic symmetry, we are interested in satisfying the Killing equation in an asymptotic sense

$$\mathcal{L}_\xi g_{\mu\nu} = \mathcal{O}(h_{\mu\nu}), \tag{1.69}$$

so that for all generators ξ^μ of $SO(4, 2)$, the Lie derivative of each metric component along ξ^μ approaches zero with the appropriate power of r as $r \rightarrow \infty$. In other words, we are looking for an asymptotic form of the metric deviation $h_{\mu\nu} \sim r^{p_{\mu\nu}}$, such that this asymptotic form is preserved by the coordinate transformations that correspond to the generators ξ^μ . Direct calculation reveals that (1.69) holds when $p_{rr} = -D - 1$, $p_{rm} = -D$, $p_{mn} = -D + 3$. Since we are interested in the case of $D = 5$ dimensions, the vacuum boundary conditions read

$$\begin{aligned} h_{rr} &= f_{rr}(t, \chi, \theta, \phi) \frac{1}{r^6} + \mathcal{O}(r^{-7}) \\ h_{rm} &= f_{rm}(t, \chi, \theta, \phi) \frac{1}{r^5} + \mathcal{O}(r^{-6}) \\ h_{mn} &= f_{mn}(t, \chi, \theta, \phi) \frac{1}{r^2} + \mathcal{O}(r^{-3}). \end{aligned} \tag{1.70}$$

By construction, these boundary conditions are preserved under $SO(4, 2)$, are broad enough to encompass the $h_{\mu\nu}$ corresponding to AdS-Schwarzschild black holes, and always yield a finite spacetime mass. These boundary conditions are valid for vacuum AAdS₅ spacetimes, and as we shall see, for spacetimes containing localized matter distributions that fall-off sufficiently quickly near the boundary.

1.5.4 Scalar Fields in Asymptotically AdS₅ Spacetimes

As we will be coupling matter to gravity, it is important to know how the presence of matter alters the vacuum boundary conditions (1.70). To understand just the asymptotics, it suffices to consider a static spherically symmetric scalar $\phi = \phi(r)$ of mass m , for which the Klein-Gordon equation

$$\square\phi = m^2\phi \tag{1.71}$$

takes the form

$$\left[\frac{rD}{L^2} + \frac{D-2}{r} + \hat{g}^{rr} \frac{\partial}{\partial r} \right] \frac{\partial \phi}{\partial r} = m^2 \phi. \quad (1.72)$$

The static ansatz $\phi(r) \sim r^{-\Delta}$ yields a quadratic equation for Δ , whose solutions are the powers of allowed fall-offs. The asymptotics for a scalar field of mass m are thus described by

$$\phi = \frac{A}{r^{d-\Delta}} + \frac{B}{r^\Delta}, \quad (1.73)$$

$$\Delta = \frac{d}{2} + \sqrt{\left(\frac{d}{2}\right)^2 + L^2 m^2}, \quad (1.74)$$

which gives $\Delta = 2 + \sqrt{4 + m^2}$ in $D \equiv d + 1 = 5$ dimensions. The usual vacuum boundary conditions given in (1.70) can accommodate a scalar field with a vanishing $A = 0$. We show in Appendix B that such a scalar field does not alter the boundary conditions (1.70), essentially because it falls off sufficiently quickly near the boundary. Matter configurations studied in this dissertation involve only scalar fields of this type.

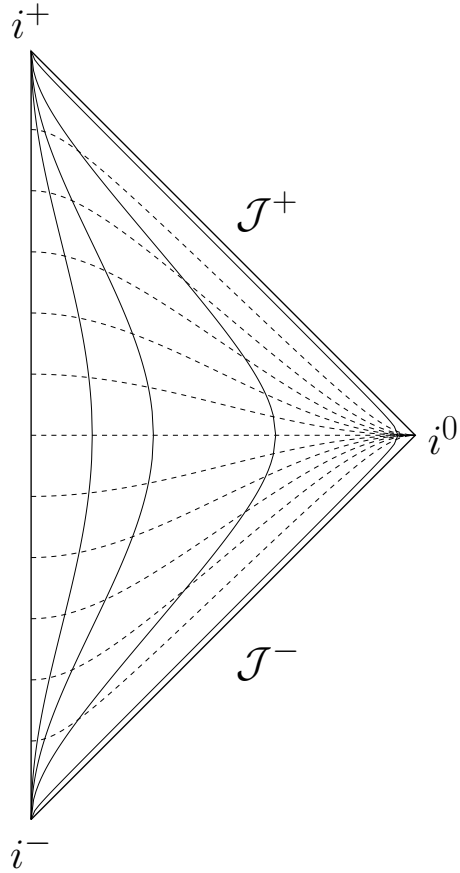


Figure 1.1: The conformal diagram of Minkowski space. The boundary consists of the point at spatial infinity i^0 , and the null surfaces at future null infinity \mathcal{J}^+ and past null infinity \mathcal{J}^- . In this compactification, future time-like infinity i^+ and past time-like infinity i^- are represented by points. Dashed lines are constant t surfaces, and solid lines are constant r surfaces.

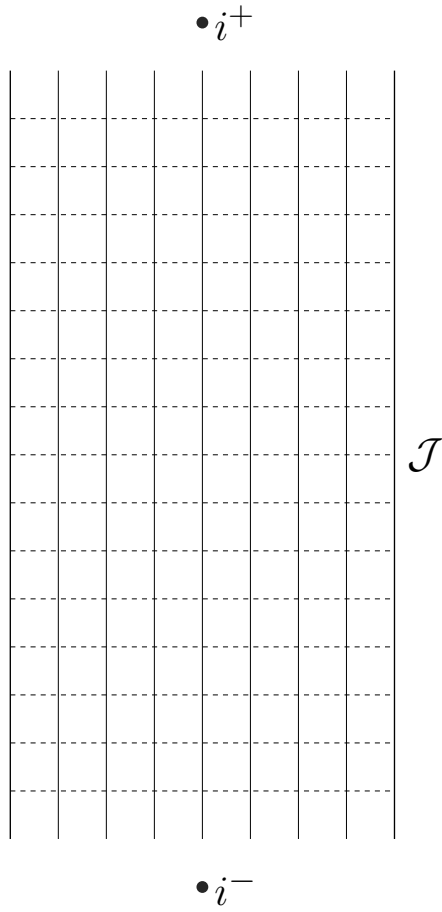


Figure 1.2: The conformal diagram of anti-de Sitter space. The boundary consists of the time-like surface \mathcal{J} ; past and future time-like infinity are represented by the points i^- and i^+ , respectively. Conventions used here are the same as those in Fig. 1.1

Chapter 2

Numerical Evolution of Asymptotically AdS Spacetimes

In this chapter we describe the ingredients we have found necessary to achieve stable evolution of AAdS₅ spacetimes within the GH formalism. The solutions in this initial study preserve an $SO(3)$ symmetry, which is sufficiently general to be physically relevant, as well as capture many of the problems and issues that need to be resolved for stable evolution. Chief among these are (a) decomposing the metric into a form that analytically factors out the AdS divergences, and dividing out sufficient powers of $1 - \rho$ from what remains, allowing us to set boundary conditions that impose the desired leading-order deviation from AdS, and (b) imposing an asymptotic gauge in terms of the source functions H^μ of the GH formalism that is consistent with the desired fall-off. These two issues are in fact intimately related in AAdS spacetimes—asking for coordinates where the leading-order metric deviations are non-singular in the approach to the boundary, together with a choice of the form of the background (singular) AdS metric, completely fixes any residual gauge freedom. The next few sections will address each of the ingredients of the GH formalism.

2.1 Initial Data with Scalar Matter

We begin by writing down an explicit form for the matter source term in (1.58) using scalar field matter content. Scalar fields are particularly convenient for our purposes, since their energy density constitutes a parameter with which we can tune the initial data. Considering cases of incrementally larger energy density then allows us to approach the dynamical, strong field regime in a controlled fashion.

The Lagrangian density of a scalar field ϕ with a potential $V(\phi)$ is given by

$$\mathcal{L}(\phi, \partial_\mu \phi) = -\frac{1}{2} g^{\alpha\beta} \partial_\alpha \phi \partial_\beta \phi - V(\phi). \quad (2.1)$$

Varying the action constructed from (2.1) with respect to the metric $g_{\alpha\beta}$ gives an energy-momentum tensor

$$T_{\mu\nu} = \partial_\mu \phi \partial_\nu \phi - g_{\mu\nu} \left(\frac{1}{2} g^{\alpha\beta} \partial_\alpha \phi \partial_\beta \phi + V(\phi) \right). \quad (2.2)$$

Substituting (1.34), (1.33), (1.46), and (2.2) into (1.44), then using the restriction of time-symmetry, which for the scalar field amounts to setting $\partial_t \phi|_{t=0} = 0$, we obtain

$$\rho_E = \zeta^{-2} \hat{\gamma}^{ij} \partial_i \phi \partial_j \phi + V(\phi). \quad (2.3)$$

The Hamiltonian constraint (1.58) thus takes the explicit form

$$\begin{aligned} \hat{\gamma}^{kl} \hat{D}_k \hat{D}_l \zeta - \frac{1}{3} (\Lambda_5 - 8\pi \hat{\gamma}^{ij} \partial_i \phi \partial_j \phi) \zeta \\ + \frac{1}{3} (\Lambda_5 + 8\pi V(\phi)) \zeta^3 = 0. \end{aligned} \quad (2.4)$$

The choice of ϕ on the spatial slice is completely arbitrary. For the tests and quasi-normal mode study described in this dissertation, we restrict ourselves to free, massless fields i.e. $V(\phi) = 0$. For the spatial profile of these fields, we use the following

5-parameter generalized Gaussian function:

$$\phi(\rho, \chi) = q^4(1 + \rho)^4 A_0 \exp\left(-\frac{(R(\rho, \chi) - R_0)^2}{\delta^2}\right) \quad (2.5)$$

where

$$\begin{aligned} R(\rho, \chi) &= \sqrt{\frac{x(\rho, \chi)^2}{w_x^2} + \frac{y(\rho, \chi)^2}{w_y^2}} \\ x(\rho, \chi) &= \rho \cos \chi \\ y(\rho, \chi) &= \rho \sin \chi. \end{aligned} \quad (2.6)$$

Here, A_0 is the maximum amplitude, R_0 fixes the radial position of the maximum, δ sets the overall compactness of the profile, and w_x, w_y can be adjusted to set the relative compactness of the profile in the x, y directions. The q^4 factor ensures that this profile has the correct fall-off for a massless scalar field, consistent with (1.73) and (1.74)¹; this is supplemented by a $(1 + \rho)^4$ factor to maintain the original Gaussian profile's even character near the origin.

2.2 Evolution Variables and Boundary Conditions

The boundary is crucial for evolution in asymptotically AdS₅ spacetimes. To find the most natural variables to evolve in this setting, we first need to gain some intuition on how the fields behave near the boundary at $\rho = 1$. To begin, let us again use (1.67) to decompose the metric $g_{\mu\nu}$ into a pure AdS₅ piece $\hat{g}_{\mu\nu}$ and a deviation $h_{\mu\nu}$. From the point of view of the evolution equations (1.31), this decomposition allows us to analytically eliminate a subset of asymptotically singular terms representing the pure AdS solution. From the point of view of the boundary conditions (1.70),

¹The q^4 prefactor on the right side of (2.5) means that we are not deforming the CFT by the dimension 4 operator dual to the massless scalar ϕ .

this decomposition guides our choice of variables that are most suitable for Cauchy evolution.

Our choice of evolution variables is largely motivated by considerations similar to those that arise when numerically solving hyperbolic partial differential equations (PDEs) whose domain includes a formally singular boundary, where one seeks solutions that remain regular at the boundary (see for example [49], where this method was introduced to study the evolution of gravitational waves in axisymmetry in a domain that includes the axis of symmetry). Before listing the variables that we use to represent the metric deviation in AAdS spacetime, let us first colloquially describe the reasoning behind their definitions. We will not *prove* that the following is a correct (or complete) characterization of the AAdS boundary behavior of our coupled system of PDEs (1.71),(1.18),(1.31); rather we will take the empirical approach that if by using this regularization scheme we are able to obtain stable, convergent numerical solutions, then this strongly suggests that the regularization is consistent, at least for the set of initial data considered. Though note that in [34] a complete characterization of boundary conditions consistent with stable evolution for *linearized* gravitational perturbations on an AdS *background* was given. As discussed in Appendix A, the boundary conditions we describe below are consistent with the Friedrich self-adjoint extension of the operator describing the scalar sector of gravitational perturbations. Thus, insofar as the linear problem guides the full non-linear problem, we can have some confidence that the following prescription is well-posed.

To illustrate, consider a function $f(t, q, \chi, \theta, \phi)$ that can be expanded in a power series in q , where the boundary is located at $q = 0$:

$$f = f_0 + f_1 q + f_2 q^2 + f_3 q^3 + \dots \tag{2.7}$$

Here, $f_0, f_1, f_2, f_3, \dots$ are functions of t, χ, θ, ϕ . Now suppose that for a regular solution (which in our case means a solution consistent with the desired AAdS fall-off) the first n terms of the RHS are required to be zero, and that the n -plus-first term describes the leading-order behavior for the particular physical solution of interest. At first glance, this would suggest that we need to supply $n + 1$ boundary conditions. However, if f satisfies a hyperbolic PDE with “standard” characteristic structure i.e. with an inward and outward propagating mode in each spatial direction, then we are usually only free to choose 1 boundary condition, effectively fixing the mode propagating into the domain. Furthermore, at a singular boundary where we demand regularity, one is often not free to choose even this ingoing mode—the outgoing mode together with regularity completely fixes it. As proposed in [49], a solution is to *define* a new evolution variable \bar{f} via

$$f(t, q, \chi, \theta, \phi) \equiv \bar{f}(t, q, \chi, \theta, \phi)q^{n-1}, \quad (2.8)$$

and demand that \bar{f} satisfy a Dirichlet condition $\bar{f}(t, q = 0, \chi, \theta, \phi) = 0$ at the boundary. Plugging this into (2.7) gives

$$\bar{f} = \dots + f_{n-2}q^{-1} + f_{n-1} + f_nq + f_{n+1}q^2 + \dots \quad (2.9)$$

One can see that if we choose regular initial data for \bar{f} that has $\bar{f}(t = 0, q = 0) = 0$, this eliminates all the components of f with undesired fall-off at $t = 0$. This will give a regular solution (analytically) for all time if the differential equation for f admits a unique solution consistent with the desired fall-off. Note that by factoring out $n - 1$ powers of q , we have assumed that the nature of the boundary is such that we are *not* free to specify the leading-order behavior encoded in f_n as a formal boundary condition, i.e. initial data together with evolution should uniquely determine it (if this were not the case, one could factor out an additional power of q , and explic-

ity set f_n). As described in more detail in Appendix A, this is consistent with the analysis of [34] on admissible boundary conditions for linearized gravitational perturbations of AdS. This is also the picture that arises in more formal derivations of the fluid/gravity correspondence in terms of derivative expansions of the field equations, where demanding normalizability at the boundary and regularity in the bulk (outside of black hole singularities) effectively constrains the gravitational dynamics of the bulk to have as many “degrees of freedom” as the dual boundary fluid dynamics. For a review, see for example [50].

Applying the above reasoning to our metric fields $g_{\mu\nu}$, we construct regularized metric variables $\bar{g}_{\mu\nu}$ that asymptotically fall-off as $\bar{g}_{\mu\nu} \sim q$:

$$\begin{aligned}
g_{tt} &= \hat{g}_{tt} + q(1 + \rho)\bar{g}_{tt} \\
g_{t\rho} &= \hat{g}_{t\rho} + q^2(1 + \rho)^2\bar{g}_{t\rho} \\
g_{t\chi} &= \hat{g}_{t\chi} + q(1 + \rho)\bar{g}_{t\chi} \\
g_{\rho\rho} &= \hat{g}_{\rho\rho} + q(1 + \rho)\bar{g}_{\rho\rho} \\
g_{\rho\chi} &= \hat{g}_{\rho\chi} + q^2(1 + \rho)^2\bar{g}_{\rho\chi} \\
g_{\chi\chi} &= \hat{g}_{\chi\chi} + q(1 + \rho)\bar{g}_{\chi\chi} \\
g_{\theta\theta} &= \hat{g}_{\theta\theta} + q(1 + \rho)(\rho^2 \sin^2 \chi)\bar{g}_{\psi} \\
g_{\phi\phi} &= \hat{g}_{\phi\phi} + q(1 + \rho)(\rho^2 \sin^2 \chi \sin^2 \theta)\bar{g}_{\psi}
\end{aligned} \tag{2.10}$$

The term in the metric $g_{\mu\nu}$ that is conformal to S^2 can be kept track of by a single variable \bar{g}_{ψ} , since we are considering solutions that preserve an $SO(3)$ symmetry that acts to rotate this S^2 ; the $\rho^2 \sin^2 \chi$ and $\rho^2 \sin^2 \chi \sin^2 \theta$ that appear in (2.10) are factored out to reflect this invariant S^2 . Additionally, the Taylor expansion of tensorial quantities in polar-like coordinates are typically either even or odd in ρ about $\rho = 0$; the $(1 + \rho)$ that appear in (2.10) have been factored out to ensure that the $\bar{g}_{\mu\nu}$ have the same even/odd character as the $g_{\mu\nu}$ in the limit $\rho \rightarrow 0$.

Using the regularized variables defined in (2.10), the boundary conditions (1.70) can be fully captured by a simple set of Dirichlet boundary conditions at spatial infinity:

$$\begin{aligned}
\bar{g}_{tt}|_{\rho=1} &= 0 \\
\bar{g}_{t\rho}|_{\rho=1} &= 0 \\
\bar{g}_{t\chi}|_{\rho=1} &= 0 \\
\bar{g}_{\rho\rho}|_{\rho=1} &= 0 \\
\bar{g}_{\rho\chi}|_{\rho=1} &= 0 \\
\bar{g}_{\chi\chi}|_{\rho=1} &= 0 \\
\bar{g}_{\psi}|_{\rho=1} &= 0.
\end{aligned} \tag{2.11}$$

We use standard results for the origin regularity conditions, which in our context read:

$$\begin{aligned}
\partial_\rho \bar{g}_{tt}|_{\rho=0} &= 0 \\
\partial_\rho \bar{g}_{t\chi}|_{\rho=0} &= 0 \\
\partial_\rho \bar{g}_{\rho\rho}|_{\rho=0} &= 0 \\
\partial_\rho \bar{g}_{\chi\chi}|_{\rho=0} &= 0 \\
\partial_\rho \bar{g}_{\psi}|_{\rho=0} &= 0 \\
\bar{g}_{t\rho}|_{\rho=0} &= 0 \\
\bar{g}_{\rho\chi}|_{\rho=0} &= 0.
\end{aligned} \tag{2.12}$$

Similar regularity conditions apply on axis:

$$\begin{aligned}
\partial_\chi \bar{g}_{tt}|_{\chi=0,\pi} &= 0 \\
\partial_\chi \bar{g}_{t\rho}|_{\chi=0,\pi} &= 0 \\
\partial_\chi \bar{g}_{\rho\rho}|_{\chi=0,\pi} &= 0 \\
\partial_\chi \bar{g}_{\chi\chi}|_{\chi=0,\pi} &= 0 \\
\partial_\chi \bar{g}_\psi|_{\chi=0,\pi} &= 0 \\
\bar{g}_{t\chi}|_{\chi=0,\pi} &= 0 \\
\bar{g}_{\rho\chi}|_{\chi=0,\pi} &= 0.
\end{aligned} \tag{2.13}$$

Elementary flatness imposes an additional relation among the metric variables on the axis, ensuring that no conical singularities arise there. Given our axial Killing vector ∂_ϕ , with norm-squared $\xi = g_{\phi\phi}$, this statement is made precise by the condition [51]

$$\left. \frac{g^{\mu\nu} \partial_\mu \xi \partial_\nu \xi}{4\xi} \right|_{\chi=0,\pi} = 1, \tag{2.14}$$

which evaluates to the following in terms of our regularized metric variables:

$$\bar{g}_{\chi\chi}|_{\chi=0,\pi} = \rho^2 \bar{g}_\psi|_{\chi=0,\pi}. \tag{2.15}$$

We ensure that this relationship is satisfied by explicitly setting $\bar{g}_{\chi\chi}$ in terms of \bar{g}_ψ on the axis as dictated by (2.15), instead of applying the regularity condition for $\bar{g}_{\chi\chi}$ as displayed in (2.13).

To find the appropriate regularized source function variables \bar{H}_μ , we insert the above expressions (2.10) for the metric components into the definition (1.11) to find how the source functions deviate from their AdS₅ values \hat{H}_μ near the boundary. Factoring out the appropriate powers of q so that $\hat{H}_\mu(q=0) = 0$, and adding powers

of $(1 + \rho)$ to maintain the same expansions near the origin, we obtain

$$\begin{aligned}
H_t &= \hat{H}_t + q^3(1 + \rho)^3 \bar{H}_t \\
H_\rho &= \hat{H}_\rho + q^2(1 + \rho)^2 \bar{H}_\rho \\
H_\chi &= \hat{H}_\chi + q^3(1 + \rho)^3 \bar{H}_\chi
\end{aligned} \tag{2.16}$$

with boundary conditions:

$$\begin{aligned}
\bar{H}_t|_{\rho=1} &= 0 \\
\bar{H}_\rho|_{\rho=1} &= 0 \\
\bar{H}_\chi|_{\rho=1} &= 0
\end{aligned} \tag{2.17}$$

origin regularity conditions:

$$\begin{aligned}
\partial_\rho \bar{H}_t|_{\rho=0} &= 0 \\
\partial_\rho \bar{H}_\chi|_{\rho=0} &= 0 \\
\bar{H}_\rho|_{\rho=0} &= 0.
\end{aligned} \tag{2.18}$$

and axis regularity conditions:

$$\begin{aligned}
\partial_\chi \bar{H}_t|_{\chi=0,\pi} &= 0 \\
\partial_\chi \bar{H}_\rho|_{\chi=0,\pi} &= 0 \\
\bar{H}_\chi|_{\chi=0,\pi} &= 0.
\end{aligned} \tag{2.19}$$

We also need a regularized massless scalar field variable $\bar{\phi}$ that asymptotically falls off as $\bar{\phi} \sim q$, so we let

$$\phi = q^3(1 + \rho)^3 \bar{\phi}. \quad (2.20)$$

with boundary condition:

$$\bar{\phi}|_{\rho=1} = 0 \quad (2.21)$$

origin regularity condition:

$$\partial_\rho \bar{\phi}|_{\rho=0} = 0. \quad (2.22)$$

and axis regularity condition:

$$\partial_\chi \bar{\phi}|_{\chi=0,\pi} = 0. \quad (2.23)$$

2.3 Source Functions

2.3.1 Gauge Choice

Choosing GH gauge conditions in AAdS₅ spacetimes is somewhat more subtle than in the usual asymptotically flat case. Roughly speaking, it turns out that it is not enough to simply demand that the metric and source functions satisfy the requisite rates of fall-off approaching the boundary as indicated in (2.10) and (2.16); rather, there are further restrictions amongst the leading-order behavior of certain fields that need to be explicitly enforced, so that the requisite fall-off is preserved during evolution.

To show this more clearly, we expand the regularized metric variables $\bar{g}_{\mu\nu}$, source functions \bar{H}_μ , and scalar field $\bar{\phi}$ in power series about $q = 0$

$$\bar{g}_{\mu\nu} = \bar{g}_{(1)\mu\nu}(t, \chi, \theta, \phi)q + \bar{g}_{(2)\mu\nu}(t, \chi, \theta, \phi)q^2 + \mathcal{O}(q^3) \quad (2.24)$$

$$\bar{H}_\mu = \bar{H}_{(1)\mu}(t, \chi, \theta, \phi)q + \bar{H}_{(2)\mu}(t, \chi, \theta, \phi)q^2 + \mathcal{O}(q^3) \quad (2.25)$$

$$\bar{\phi} = \bar{\phi}_{(1)}(t, \chi, \theta, \phi)q + \bar{\phi}_{(2)}(t, \chi, \theta, \phi)q^2 + \mathcal{O}(q^3) \quad (2.26)$$

and substitute these expressions into the field equations (1.31). Since the GH form of the field equations results in PDEs where the principle part of each equation is a wave operator acting on the metric (this fact guides our numerical solution method), we will schematically write this perturbative expansion of the field equations for the leading component $\bar{g}_{(1)\mu\nu}$ of $\bar{g}_{\mu\nu}$ as follows

$$\tilde{\square}\bar{g}_{(1)\mu\nu} = \dots \quad (2.27)$$

where we use the symbol $\tilde{\square}$ to denote a wave-like operator active within the (t, χ, θ, ϕ) subspace, and containing terms of the form $c_0 \cdot \partial^2 \bar{g}_{(1)\mu\nu} / \partial t^2 - c_1 \cdot \partial^2 \bar{g}_{(1)\mu\nu} / \partial \chi^2 + \dots$. Here, c_0, c_1, \dots are coefficient functions that are in general different for each component of the field equations, but are regular and finite on the boundary. Their particular form is unimportant here, as we are interested in highlighting the leading-order terms sourcing the wave-like equation on the RHS of (2.27).

In this notation, the field equations near $q = 0$ read

$$\begin{aligned}
\tilde{\square}\bar{g}_{(1)tt} &= (-8\bar{g}_{(1)\rho\rho} + 4\bar{H}_{(1)\rho})q^{-2} + \mathcal{O}(q^{-1}) \\
\tilde{\square}\bar{g}_{(1)t\rho} &= (-60\bar{g}_{(1)t\rho} - 8\cot\chi\bar{g}_{(1)t\chi} + 24\bar{H}_{(1)t} - \bar{g}_{(1)tt,t} \\
&\quad + 2\bar{g}_{(1)t\chi,\chi} + 2\bar{g}_{(1)\rho\rho,t} - \bar{g}_{(1)\chi\chi,t} - 2\bar{g}_{(1)\psi,t} - 2\bar{H}_{(1)\rho,t})q^{-2} + \mathcal{O}(q^{-1}) \\
\tilde{\square}\bar{g}_{(1)t\chi} &= \mathcal{O}(q^{-1}) \\
\tilde{\square}\bar{g}_{(1)\rho\rho} &= (-8\bar{g}_{(1)tt} - 24\bar{g}_{(1)\rho\rho} + 8\bar{g}_{(1)\chi\chi} + 16\bar{g}_{(1)\psi} + 16\bar{H}_{(1)\rho})q^{-2} + \mathcal{O}(q^{-1}) \\
\tilde{\square}\bar{g}_{(1)\rho\chi} &= (-60\bar{g}_{(1)\rho\chi} - 8\cot\chi\bar{g}_{(1)\chi\chi} + 8\cot\chi\bar{g}_{(1)\psi} + 24\bar{H}_{(1)\chi} \\
&\quad + \bar{g}_{(1)tt,\chi} - 2\bar{g}_{(1)t\chi,t} + 2\bar{g}_{(1)\rho\rho,\chi} + \bar{g}_{(1)\chi\chi,\chi} - 2\bar{g}_{(1)\psi,\chi} - 2\bar{H}_{(1)\rho,\chi})q^{-2} + \mathcal{O}(q^{-1}) \\
\tilde{\square}\bar{g}_{(1)\chi\chi} &= (8\bar{g}_{(1)\rho\rho} - 4\bar{H}_{(1)\rho})q^{-2} + \mathcal{O}(q^{-1}) \\
\tilde{\square}\bar{g}_{(1)\psi} &= \sin^2\chi(8\bar{g}_{(1)\rho\rho} - 4\bar{H}_{(1)\rho})q^{-2} + \mathcal{O}(q^{-1}), \tag{2.28}
\end{aligned}$$

and again we re-emphasize that $\tilde{\square}$ is used to schematically denote a regular wave operator, though its specific form is in general different for each equation. For reference, we also list the leading-order behavior of the GH constraints (1.19):

$$\begin{aligned}
C_t &= (20\bar{g}_{(1)t\rho} - 8\bar{H}_{(1)t} + \bar{g}_{(1)tt,t} - 2\bar{g}_{(1)t\chi,\chi} + \bar{g}_{(1)\rho\rho,t} + \bar{g}_{(1)\chi\chi,t} + 2\bar{g}_{(1)\psi,t})q^4 + \mathcal{O}(q^5) \\
C_\rho &= (8\bar{g}_{(1)tt} + 8\bar{g}_{(1)\rho\rho} - 8\bar{g}_{(1)\chi\chi} - 16\bar{g}_{(1)\psi} - 8\bar{H}_{(1)\rho})q^3 + \mathcal{O}(q^4) \\
C_\chi &= (20\bar{g}_{(1)\rho\chi} - 8\bar{H}_{(1)\chi} - \bar{g}_{(1)tt,\chi} + 2\bar{g}_{(1)t\chi,t} + \bar{g}_{(1)\rho\rho,\chi} - \bar{g}_{(1)\chi\chi,\chi} + 2\bar{g}_{(1)\psi,\chi})q^4 + \mathcal{O}(q^5). \tag{2.29}
\end{aligned}$$

In order for the evolution to be consistent with each metric component's desired fall-off indicated in (2.10), the leading-order “source” on the right-hand side of each equation in (2.28) must scale as q^0 due to the Dirichlet boundary conditions (2.11). This implies that all terms of order q^{-2} and q^{-1} must vanish, and it would thus appear as though there were an additional hierarchy of constraints that need to be satisfied

before the leading-order dynamics in the q^0 term becomes manifest (note that these constraints are *not* simply the GH constraints (2.29)). This is, in part, an artifact of having decomposed the field equations in a near-boundary expansion such as (2.24): when solving the full equations consistently (i.e., with a Cauchy evolution scheme and initial data satisfying the constraints, along with stable, consistent boundary conditions as discussed in the previous sections), one usually expects that the evolution will “conspire” to preserve what appears as constraints in the perturbative expansion. However, there are two potential complications in the AAdS case, highlighted in the above by the fact that the leading-order power in the expansions *diverge* as q^{-2} .

First, in the GH method, one is free to choose \bar{H}_μ as the gauge, and though the structure of the field equations guarantee that the resultant solution will be consistent, there is *no* guarantee that a given choice of \bar{H}_μ will preserve the desired asymptotic fall-off of the metric (2.10). Case in point, suppose that we started with some initial value $\bar{H}_\mu(t = 0)$, and wanted to evolve to a gauge that in time becomes harmonic with respect to pure AdS, namely $\bar{H}_\mu(t \gg 0) = 0$ so that $H_\mu(t \gg 0) = \hat{H}_\mu$ in (2.16). Then (2.28) for $\bar{g}_{(1)tt}$ immediately tells us that either $\bar{g}_{(1)\rho\rho}$ must evolve to 0, or $\bar{g}_{(1)tt}$ ceases to remain regular. Whichever scenario unfolds, this choice of gauge leads to a representation of the metric that is not consistent with the fall-off assumed in (2.10), and as discussed in Sec. 2.2, it would generically be difficult (or even impossible) to come up with a numerical scheme to stably evolve such a situation.

Second, the form of the equations in (2.28) *imply* that regularity requires a delicate cancellation between terms in the near-boundary limit. Thus any truncation error introduced by a numerical scheme must be sufficiently small to effectively scale by some high power of q in the limit. In a typical finite difference scheme, the closest point to the boundary will be $q = h$, where h is the mesh-spacing there. Naively then, from (2.28) one would expect to need a discretization scheme that has local convergence order $n + 2$ to obtain global n^{th} order convergence of the solution. Fortu-

nately, this naive argument apparently does not hold with our code and the situations we have explored to date: we observe global second-order convergence using second-order accurate finite difference discretization. We are not sure why this is so; again, it could simply be that the near-boundary expansion is giving a misleading picture of the nature of evolution of the full set of equations, or it could be due to the particular asymptotic gauge choice we use, described in the remainder of this section.

We have experimented with a small handful of gauge choices which were unstable, including evolution to harmonic with respect to AdS ($\bar{H}_\mu(t > 0) \rightarrow 0$, though as argued above one expects problems with this), and a fixed gauge ($\partial\bar{H}_\mu/\partial t = 0$, and we note that our initial data is fully consistent with all the “constraints” in (2.28) and (2.29)). When a numerical solution is unstable, it is often difficult to isolate the source: the gauge could be inconsistent in the sense discussed above, the discretization scheme could be unstable for the particular set of equations, there is a bug, etc. So here we simply list the asymptotic gauge condition we have empirically found to be stable (see the following section for an explicit expression of the particular source functions used in this study):

$$\begin{aligned}
\bar{H}_t|_{\rho=1} &= \frac{5}{2} \bar{g}_{t\rho}|_{\rho=1} \\
\bar{H}_\rho|_{\rho=1} &= 2 \bar{g}_{\rho\rho}|_{\rho=1} \\
\bar{H}_\chi|_{\rho=1} &= \frac{5}{2} \bar{g}_{\rho\chi}|_{\rho=1}.
\end{aligned}
\tag{2.30}$$

This choice was in part motivated by the asymptotic form of the field equations, in that these conditions, in conjunction with the GH constraints (2.29) explicitly eliminate many of the order q^{-2} terms that appear in (2.28). However, this is almost certainly not a unique choice for stability, and one can anticipate that modifications would be required if, for example, the code is used to explore situations with less symmetry, or

to study scenarios where the boundary theory is “deformed” in a manner that alters the leading-order AAdS asymptotics.

2.3.2 Implementing the Gauge Choice

As described in Sec. 2.3.1, we are not free to arbitrarily choose the leading-order behavior of the source functions approaching the AdS boundary if subsequent evolution of the field equations is to preserve the desired asymptotic form for the metric (1.70). Specifically, we want to consider a class of gauges that satisfy the asymptotic conditions (2.30).

A naive implementation of (2.30), wherein one would set $H^\mu(t > 0)$ *everywhere* on the grid to the values prescribed by (2.30), would result in a discontinuous gauge at $t = 0$, as our method of solving for the initial data in general gives a different form for $H^\mu(t = 0)$ on the interior. This is rather common in GH evolution i.e. the initial data provides source functions that are different from that of the target gauge, and the usual way to deal with this is to construct a hybrid gauge that smoothly transitions in time from the initial gauge to the target gauge. The specific transition we use is as follows. Denote the source functions coming from the initial data by $\bar{H}_\mu^{(0)} \equiv \bar{H}_\mu|_{t=0}$, and define the functions F_ν to be the asymptotic constraints trivially extended into the bulk²:

$$\begin{aligned} F_t(t, \rho, \chi) &\equiv \frac{5}{2}\bar{g}_{t\rho}(t, \rho, \chi) \\ F_\rho(t, \rho, \chi) &\equiv 2\bar{g}_{\rho\rho}(t, \rho, \chi) \\ F_\chi(t, \rho, \chi) &\equiv \frac{5}{2}\bar{g}_{\rho\chi}(t, \rho, \chi). \end{aligned} \tag{2.31}$$

²Of course, a more general implementation could allow for an arbitrary gauge in the bulk that only asymptotically approaches (2.30) as $\rho \rightarrow 1$, though for the spacetimes we have evolved to-date this simple choice has worked well.

Then, we choose

$$\begin{aligned}\bar{H}_\mu(t, \rho, \chi) &= \bar{H}_\mu^{(0)}(t, \rho, \chi) [g(t, \rho)] \\ &+ F_\nu(t, \rho, \chi) [1 - g(t, \rho)],\end{aligned}\tag{2.32}$$

with

$$g(t, \rho) = \exp(-z(t, \rho)^4),\tag{2.33}$$

$$z(t, \rho) = \frac{t}{\xi_2 f(\rho) + \xi_1 [1 - f(\rho)]},\tag{2.34}$$

and

$$f(\rho) = \begin{cases} 1 & \rho \geq \rho_2 \\ 1 - y^3(6y^2 - 15y + 10) & \rho_2 \geq \rho \geq \rho_1 \\ 0 & \text{otherwise} \end{cases},\tag{2.35}$$

where $y(\rho) = (\rho_2 - \rho)/(\rho_2 - \rho_1)$, and ξ_1, ξ_2, ρ_1 and ρ_2 are user-specified constants. The time-transition function g is such that $g(0, \rho) = 1$, $\dot{g}(0, \rho) = 0$, $\ddot{g}(0, \rho) = 0$, and $\lim_{t \rightarrow \infty} g(t, \rho) = 0$; it is designed to give (2.32) the correct initial and target values, and transition between the two in a continuous fashion. The function $f(\rho)$, on the other hand, is such that $f(\rho_1) = 0$, $f'(\rho_1) = 0$, $f''(\rho_1) = 0$ and $f(\rho_2) = 0$, $f'(\rho_2) = 0$, $f''(\rho_2) = 0$; it is designed to let the transition occur with characteristic time ξ_1 for radii $\rho < \rho_1$, interpolating to a characteristic time of ξ_2 for radii $\rho \geq \rho_2$. It is important near the boundary to reach the target gauge quickly, as this is where the delicate cancellations made possible by the gauge (2.30) are crucially needed. Accordingly, ξ_2 is generally set to a small number. On the other hand, it may not be desirable to have such rapid gauge dynamics in the interior, and ξ_1 thus allows us to independently control the characteristic gauge evolution time there. On a typical run, we set $\rho_1 = 0.0, \rho_2 = 0.95, \xi_1 = 0.1, \xi_2 = 0.0025$.

2.3.3 Initializing the 5-metric at $t = 0$

Our goal in this section is to describe a choice of $\bar{g}_{\nu\sigma}|_{t=0}$, $\partial_t \bar{g}_{\nu\sigma}|_{t=0}$ such that the source functions at $t = 0$, as evaluated via (1.11), are compatible with our target gauge (2.30). (The spatial components of the initial data $\bar{g}_{ij}|_{t=0}$ and $\partial_t \bar{g}_{ij}|_{t=0}$ come from the solution to the constraint equations described in Sec. 2.1). In the notation of the power-series expansion about $q = 0$ performed in the previous section, the leading-order coefficients of (1.11) evaluated using (2.10) read

$$\begin{aligned}
\bar{H}_{(1)t} &= \frac{5}{2}\bar{g}_{(1)t\rho} + \frac{1}{8}\bar{g}_{(1)tt,t} - \frac{1}{4}\bar{g}_{(1)t\chi,\chi} + \frac{1}{8}\bar{g}_{(1)\rho\rho,t} \\
&\quad + \frac{1}{8}\bar{g}_{(1)\chi\chi,t} + \frac{1}{4}\bar{g}_{(1)\psi,t} \\
\bar{H}_{(1)\rho} &= \bar{g}_{(1)tt} + \bar{g}_{(1)\rho\rho} - \bar{g}_{(1)\chi\chi} - 2\bar{g}_{(1)\psi} \\
\bar{H}_{(1)\chi} &= \frac{5}{2}\bar{g}_{(1)\rho\chi} - \frac{1}{8}\bar{g}_{(1)tt,\chi} + \frac{1}{4}\bar{g}_{(1)t\chi,t} + \frac{1}{8}\bar{g}_{(1)\rho\rho,\chi} \\
&\quad - \frac{1}{8}\bar{g}_{(1)\chi\chi,\chi} + \frac{1}{4}\bar{g}_{(1)\psi,\chi}.
\end{aligned} \tag{2.36}$$

Similarly, the leading-order coefficients of (2.30) read

$$\begin{aligned}
\bar{H}_{(1)t} &= \frac{5}{2}\bar{g}_{(1)t\rho} \\
\bar{H}_{(1)\rho} &= 2\bar{g}_{(1)\rho\rho} \\
\bar{H}_{(1)\chi} &= \frac{5}{2}\bar{g}_{(1)\rho\chi}.
\end{aligned} \tag{2.37}$$

Inspection of the above relations, together with our choice of time symmetry ($\partial_t \bar{g}_{ij}|_{t=0} = 0$), shows that the following is required to leading order approaching $\rho = 1$:

$$\bar{g}_{tt}|_{t=0} = (\bar{g}_{\rho\rho} + \bar{g}_{\chi\chi} + 2\bar{g}_{\psi})|_{t=0} \tag{2.38}$$

$$\partial_t \bar{g}_{tt}|_{t=0} = 0 \tag{2.39}$$

$$\partial_t \bar{g}_{t\chi}|_{t=0} = \partial_\chi \bar{g}_{\chi\chi}|_{t=0}. \tag{2.40}$$

In practice we impose (2.39) and (2.40) over the entire computational domain, and impose (2.38) in an asymptotic sense: we set $\bar{g}_{tt}|_{t=0} = 0$ for $\rho < \rho_0$, where $\rho_0 < 1$ is a user-specified parameter, and smoothly transition to (2.38) as $\rho \rightarrow 1$. In this way, we keep the form of $\bar{g}_{tt}|_{t=0}$ as simple as possible in the interior. The relations (2.36) and (2.37) leave the remaining metric variables $\bar{g}_{t\rho}|_{t=0}$, $\partial_t \bar{g}_{t\rho}|_{t=0}$ and $\bar{g}_{t\chi}|_{t=0}$ unconstrained, and we again take the simplest choice and set them to zero. In ADM language, these conditions amount to a choice of initial lapse, shift and their first time derivatives.

2.4 Numerical Solution Methods

The primary challenge in dealing with AAdS spacetimes lies in the nature of the boundary, which must largely be dealt with analytically, as discussed in detail in the previous section. Once this is done, the numerical discretization and solution method is rather conventional. The methods we use are very similar to those described in [27], and so we simply list them here, referring the reader to [27] for the details.

All equations and boundary conditions are discretized using second-order accurate finite difference methods; see Appendix C. The only non-trivial boundary conditions are the Neumann conditions at the origin ($\rho = 0$), and the regularity conditions on the axis ($\chi = 0, \pi$). The discretized Hamiltonian constraint (2.4) is solved using a full approximation storage (FAS) multigrid algorithm with v-cycling, and Newton-Gauss-Seidel iteration for the smoother. The evolution equations for the metric (1.31) and scalar field (1.71) (with energy-momentum tensor (2.2)), are discretized after substituting in the definitions for our regularized metric variables (2.10), scalar field (2.20), and source functions (2.16). The corresponding regular fields ($\bar{g}_{\mu\nu}, \bar{\phi}$) are solved for using an iterative, Newton-Gauss-Seidel relaxation procedure. In this study we have

not explored any dynamical gauge evolution equations for \bar{H}^μ , and simply set them to prescribed functions of the $\bar{g}_{\mu\nu}$ as outlined in the next section.

We use the excision method to solve for black hole spacetimes, which involves *excising* a portion of the grid within the apparent horizon (AH), thus removing the geometric singularity from the computational domain. Due to the causal structure of the spacetime within the horizon, all physical characteristics of the equations flow out of the domain (i.e. into the excised region). Thus excision implies that the usual field equations are still solved on the excision surface, except that centered difference stencils are replaced with sideways stencils where appropriate, in order to reference information that is only from the outside of the excision surface (in other words, *no* boundary conditions are placed there). We search for the AH using a flow method; the excision surface is defined to be a surface with the same coordinate shape as the AH, but some fraction $1 - \delta_{ex}$ smaller, where we typically use $\delta_{ex} \in [0.05, 0.2]$. One issue with using polar-like coordinates is that it incurs a rather severe restriction on the Courant-Friedrichs-Lewy (CFL) factor λ that defines the time step $\Delta t \equiv \lambda \min(\Delta\rho, \Delta\chi)$, where $\Delta\rho$ and $\Delta\chi$ are the mesh spacings in ρ and χ respectively. Roughly speaking, with a uniform discretization in ρ and χ , the condition for stability is $\lambda < \rho_{min}$, where ρ_{min} is the smallest non-zero coordinate within the discrete domain. Ostensibly this occurs next to the origin, where $\rho_{min} = \Delta\rho$, so in the limit of high resolution the time-step size can become prohibitively small. For the tests and results presented here, we sidestep this issue by only studying black hole spacetimes, where excision removes the origin from the computational domain.

Kreiss-Oliger dissipation [52], with reduction of order approaching boundaries as described in [53], is used to help damp unphysical high-frequency solution components that sometimes arise at grid boundaries, in particular the excision surface; we typically use a dissipation parameter of $\epsilon = 0.35$.

We use the PAMR/AMRD ³ libraries to provide support for running in parallel on Linux computing clusters. The libraries also support adaptive mesh refinement (AMR), though all results described here are unigrid.

³<http://laplace.physics.ubc.ca/Group/Software.html>

Chapter 3

Reconstructing Boundary CFT

Observables

3.1 The Stress Energy Tensor of the Dual CFT

Here we briefly mention the most relevant entry in the AdS/CFT dictionary for this dissertation, namely the one that enables us to extract the expectation value $\langle T_{\mu\nu} \rangle_{\text{CFT}}$ of the CFT stress energy tensor from the asymptotic behavior of the metric:¹

$$\langle T_{\mu\nu} \rangle_{\text{CFT}} = \lim_{q \rightarrow 0} \frac{1}{q^2} {}^{(q)}T_{\mu\nu}. \quad (3.1)$$

Here, $q = 1 - \rho$ (though more generally q is a smooth positive scalar with a simple zero at the AAdS boundary), and ${}^{(q)}T_{\mu\nu}$ is the Brown-York quasi-local stress tensor [54].

For AAdS₅ spacetimes, the quasi-local stress tensor defined on a $q = \text{const.}$ time-like

¹The full expression for the boundary stress tensor includes a factor of $1/G$, where G is Newton's constant, corresponding to a scaling as N^2 in the large N gauge theory dual to AdS_5 . We have omitted the factor of $1/G$ from (3.1) in keeping with our standard convention that $G = 1$. When quoting explicit numerical results for the boundary stress tensor, we will also set $L = 1$. By doing so we are restricting to a specific count of degrees of freedom in the boundary theory; but since the scaling of $\langle T_{\mu\nu} \rangle$ is straightforward, there is no significant loss of generality.

hypersurface ∂M_q was constructed in [55], and is given by

$${}^{(q)}T_{\mu\nu}^0 = \frac{1}{8\pi} \left({}^{(q)}\Theta_{\mu\nu} - {}^{(q)}\Theta \Sigma_{\mu\nu} - \frac{3}{L} \Sigma_{\mu\nu} + {}^{(q)}G_{\mu\nu} \frac{L}{2} \right). \quad (3.2)$$

Here, ${}^{(q)}\Theta_{\mu\nu} = -\Sigma^\alpha{}_\mu \Sigma^\beta{}_\nu \nabla_{(\alpha} S_{\beta)}$ is the extrinsic curvature of the time-like surface ∂' , S^μ is a space-like, outward pointing unit vector normal to the surface ∂M_q , $\Sigma_{\mu\nu} \equiv g_{\mu\nu} - S_\mu S_\nu$ is the induced 4-metric on ∂M_q , ∇_α is the covariant derivative operator, and ${}^{(q)}G_{\mu\nu}$ is the Einstein tensor associated with $\Sigma_{\mu\nu}$. The last two terms in (3.2) are counterterms designed to exactly cancel the divergent boundary behavior of the first two terms of (3.2) evaluated in pure AdS₅.

A feature of the stress tensor (3.2) is that it is non-vanishing even when the geometry is that of pure AdS₅. This non-vanishing piece was already noticed in [55], and was correctly identified as the contribution from the Casimir energy of the boundary CFT: this CFT is defined on a manifold with topology $\mathbb{R} \times S^3$, and so can have a non-vanishing vacuum energy. Since this Casimir contribution is non-dynamical, we consider it as part of our background vacuum and simply subtract it from (3.2), obtaining

$${}^{(q)}T_{\mu\nu} = {}^{(q)}T_{\mu\nu}^0 - t_{\mu\nu}. \quad (3.3)$$

Setting $L = 1$, the non-zero components of the Casimir contribution $t_{\mu\nu}$ are $t_{tt} = 3q^2/(64\pi)$, $t_{\chi\chi} = q^2/(64\pi)$, $t_{\theta\theta} = q^2 \sin^2 \chi/(64\pi)$, and $t_{\phi\phi} = t_{\theta\theta} \sin^2 \theta$.

In terms of the regularized metric variables (2.10), and setting $L = 1$, the stress energy tensor of the boundary CFT (3.1) evaluates to

$$\begin{aligned}
\langle T_{tt} \rangle_{\text{CFT}} &= \frac{1}{64\pi} (-24\bar{g}_{\rho\rho,\rho} - 32\bar{g}_{\chi\chi,\rho} - 64\bar{g}_{\psi,\rho}) \\
\langle T_{t\chi} \rangle_{\text{CFT}} &= \frac{1}{2\pi} (-\bar{g}_{t\chi,\rho}) \\
\langle T_{\chi\chi} \rangle_{\text{CFT}} &= \frac{1}{64\pi} (-32\bar{g}_{tt,\rho} + 24\bar{g}_{\rho\rho,\rho} + 64\bar{g}_{\psi,\rho}) \\
\langle T_{\theta\theta} \rangle_{\text{CFT}} &= \frac{\sin^2 \chi}{64\pi} (-32\bar{g}_{tt,\rho} + 24\bar{g}_{\rho\rho,\rho} + 32\bar{g}_{\chi\chi,\rho} \\
&\quad + 32\bar{g}_{\psi,\rho}).
\end{aligned}
\tag{3.4}$$

and $\langle T_{\phi\phi} \rangle_{\text{CFT}} = \sin^2 \theta \langle T_{\theta\theta} \rangle_{\text{CFT}}$.

3.2 Hydrodynamic Description of the Boundary CFT

3.2.1 Extracting Fluid Variables

Essentially all known physical systems at sufficiently high temperature, including those described by quantum field theories, exhibit hydrodynamic behavior on large scales once local thermodynamic equilibrium has been attained. In the gauge/gravity duality, stationary black holes are dual to equilibrium thermal states, and studies have shown that perturbations of the bulk spacetime manifest as hydrodynamic behavior in the boundary CFT. See [50] for a recent review, and [56] for a review of the “blackfolds” approach, which is similar in spirit but connects the dynamics of a perturbed black brane with that of an enclosing world-volume via a derivative expansion of the Einstein field equations. Here, we have studied the evolution of initially highly distorted black holes, far from the perturbative regime, and so the question naturally arises: at what time does hydrodynamics become a good description of the bound-

ary state? More precisely, we would like to know whether the extracted $\langle T_{\mu\nu} \rangle_{\text{CFT}}$ on the $\mathbb{R} \times S^3$ boundary is that of the particular kind of fluid predicted by the duality, namely an $\mathcal{N} = 4$ SYM fluid with equation of state $\epsilon = 3P$ (where ϵ and P are the energy density and isotropic pressure in the rest frame of the fluid, respectively), and transport coefficients that match those found via holographic methods [57].

In a low-energy effective description, the hydrodynamic stress tensor can be expressed as a velocity-gradient expansion, i.e. as a power series in the covariant gradients of a local fluid 4-velocity one form u_ν :

$$T_{\mu\nu} = (\epsilon + P)u_\mu u_\nu + P g_{\mu\nu} - 2\eta\sigma_{\mu\nu} + \Pi_{\mu\nu}, \quad (3.5)$$

where we have introduced the (symmetric, traceless) shear tensor

$$\sigma^{\mu\nu} = \perp^{\mu\alpha} \perp^{\nu\beta} \nabla_{(\alpha} u_{\beta)} - \frac{1}{d-1} \nabla_\alpha u^\alpha \perp^{\mu\nu}, \quad (3.6)$$

and subsumed all higher-order terms under $\Pi_{\mu\nu}$. All covariant differentiation is performed with respect to the boundary metric $g_{\mu\nu} dx^\mu dx^\nu = -dt^2 + d\chi^2 + \sin^2 \chi (d\theta^2 + \sin^2 \theta d\phi^2)$, and $\perp^{\mu\nu}$ in (3.6) is the projector onto the spatial slices orthogonal to the fluid 4-velocity

$$\perp^{\mu\nu} = g^{\mu\nu} + u^\mu u^\nu. \quad (3.7)$$

In this sub-section, we will for now ignore the higher-order terms, i.e. we set $\Pi_{\mu\nu} = 0$. In terms of mapping from stress tensor to hydrodynamic variables this should be a good approximation except in situations where the shear $\sigma_{\mu\nu}$ of the flow becomes small, which does occur periodically during the evolution of the distorted black holes discussed here. These higher order terms would lead to additional problems regarding the uniqueness of the mapping that we will now attempt. In the sub-section following this one, we will employ a different strategy and will instead extract a minimal subset,

then, assuming an $\mathcal{N} = 4$ SYM fluid, test for consistency with higher order transport coefficients (instead of trying to directly measure all these quantities, as we will now proceed to do).

Let us first identify a set of independent fluid variables which we can use to characterize the stress tensor. This set certainly includes ϵ and P , the energy density and isotropic pressure in the rest frame of the fluid, respectively. Given the $SO(3)$ symmetry of our solutions, the (unit) 4-velocity vector must take the form $u^\mu = \gamma(1, v, 0, 0)$ in (t, χ, θ, ϕ) coordinates, with $\gamma = 1/\sqrt{1-v^2}$. This gives us a third fluid variable to add to our list: v , the χ -coordinate velocity of the flow. As for the shear $\sigma_{\mu\nu}$, notice that it is symmetric, traceless and satisfies the identity $u^\mu \sigma_{\mu\nu} = 0$. Together with the imposed $SO(3)$ symmetry, these imply that $\sigma_{\mu\nu}$ only has one degree of freedom in $d = 4$ dimensions. Thus defining $\sigma_{\chi\chi} = \sigma$, one can straightforwardly show that the only other non-zero components of $\sigma_{\mu\nu}$ are:

$$\sigma_{t\chi} = -v\sigma, \quad \sigma_{tt} = v^2\sigma, \quad \sigma_{\theta\theta} = \frac{\sigma_{\phi\phi}}{\sin^2\theta} = -\frac{\sin^2\chi}{2\gamma^2}\sigma. \quad (3.8)$$

Given how η and σ always appear as a product in (3.5), we treat the two as a single quantity $\eta\sigma$ for the purposes of extraction. Thus, ignoring the higher-order terms $\Pi_{\mu\nu}$, the variables $(\epsilon, P, v, \eta\sigma)$, each of which is a function of (t, χ) in general, completely describes a conformal fluid flow on $\mathbb{R} \times S^3$ that preserves our $SO(3)$ symmetry.

On the gravity side, the quantities we measure are the components of the boundary stress tensor, which we denote $T_{\mu\nu} \equiv \langle T_{\mu\nu} \rangle_{\text{CFT}}$ in this section and the next, for the sake of brevity. In $SO(3)$ symmetry, there are 5 non-zero stress tensor components,

4 of which are independent. We can relate these 4 to the fluid variables via (3.5):

$$\begin{aligned}
T_{tt} &= (\epsilon + P) \frac{1}{1 - v^2} - P - 2\eta\sigma v^2 \\
T_{t\chi} &= -(\epsilon + P) \frac{v}{1 - v^2} + 2\eta\sigma v \\
T_{\chi\chi} &= (\epsilon + P) \frac{v^2}{1 - v^2} + P - 2\eta\sigma \\
T_{\theta\theta} &= \sin^2 \chi (P + \eta\sigma(1 - v^2))
\end{aligned} \tag{3.9}$$

where $T_{\phi\phi} = \sin^2 \theta T_{\theta\theta}$. Inverting these relations in favor of the rest-frame hydrodynamic quantities $(\epsilon, P, v, \eta\sigma)$, and defining the auxiliary quantities

$$\begin{aligned}
\Xi &\equiv \sqrt{(T_{\chi\chi} + 2T_{t\chi} + T_{tt})(T_{\chi\chi} - 2T_{t\chi} + T_{tt})} \\
T_\psi &\equiv \frac{T_{\theta\theta}}{\sin^2 \chi},
\end{aligned} \tag{3.10}$$

we obtain

$$\begin{aligned}
\epsilon &= \frac{1}{2} (T_{tt} - T_{\chi\chi} + \Xi) \\
P &= \frac{1}{6} (\Xi + T_{\chi\chi} + 4T_\psi - T_{tt}) \\
v &= \frac{\Xi - T_{\chi\chi} - T_{tt}}{2T_{t\chi}} \\
\eta\sigma &= \left[-T_{\chi\chi}^3 + T_{\chi\chi}^2 (-\Xi + T_\psi - 2T_{tt}) \right. \\
&\quad \left. + T_{\chi\chi} (T_\psi (\Xi + 2T_{tt}) - T_{tt} (\Xi + T_{tt}) - 4T_{t\chi}^2) \right. \\
&\quad \left. + T_\psi (T_{tt} (\Xi + T_{tt}) + 4T_{t\chi}^2) - 2T_{t\chi}^2 \Xi \right] / [6\Xi],
\end{aligned} \tag{3.11}$$

3.2.2 Extracting Transport Coefficients

In this section, we present an alternative method for comparing $\langle T_{\mu\nu} \rangle_{\text{CFT}}$ with the stress tensor of an $\mathcal{N} = 4$ SYM fluid. To accomplish this, let us first add as many

higher-order terms $\Pi_{\mu\nu}$ to the hydrodynamic stress tensor (3.5) as is presently known, which includes viscous corrections up to second-order in the gradient expansion. This gives four additional higher-order transport coefficients to supplement the shear viscosity η : the stress relaxation time τ_π , the shear vorticity coupling τ_ω , the shear-shear coupling ξ_σ , and the Weyl curvature coupling ξ_C . Our strategy here will be different from the one described in the previous sub-section, where we had first extracted all hydrodynamic variables from the CFT stress tensor components, then exhibited evidence that the conformal constitutive relations hold. Instead, we will now *assume* that the conformal constitutive relations hold at the outset, allowing us to reconstruct the hydrodynamic stress tensor order by order using only the energy density ϵ and the fluid four-velocity u^μ .

This reconstruction takes the form

$$T_{\mu\nu} = \sum_{i=0}^{\infty} T_{\mu\nu}^{(i)} \quad (3.12)$$

where $T_{\mu\nu}^{(0)}$ corresponds to the stress tensor of an ideal relativistic fluid, and $T_{\mu\nu}^{(i)}$ accounts for the i^{th} -order correction in a velocity-gradient expansion. These corrections are explicitly given in [57] for an $\mathcal{N} = 4$ SYM fluid:

$$\begin{aligned} T_{\mu\nu}^{(0)} &= \epsilon u_\mu u_\nu + P \perp_{\mu\nu} \\ T_{\mu\nu}^{(1)} &= -2\eta \sigma_{\mu\nu} \\ T_{\mu\nu}^{(2)} &= -2\eta \left[-\tau_\pi u^\lambda \mathcal{D}_\lambda \sigma_{\mu\nu} + \tau_\omega (\omega_\mu^\lambda \sigma_{\lambda\nu} + \omega_\nu^\lambda \sigma_{\lambda\mu}) \right] \\ &\quad + \xi_\sigma \left[\sigma_\mu^\lambda \sigma_{\lambda\nu} - \frac{\perp^{\mu\nu}}{3} \sigma^{\alpha\beta} \sigma_{\alpha\beta} \right] + \xi_C C_{\mu\alpha\nu\beta} u^\alpha u^\beta \end{aligned} \quad (3.13)$$

where $C_{\mu\alpha\nu\beta}$ is the Weyl tensor and \mathcal{D} is the Weyl covariant derivative defined in [57]. One further input are the constitutive relations for our $\mathcal{N} = 4$ SYM fluid:

$$\begin{aligned}
\epsilon &= \frac{3N_c^2}{8\pi^2} (\pi T)^4 = 3P \\
\eta &= \frac{N_c^2}{8\pi^2} (\pi T)^3 \\
\tau_\pi &= \frac{2 - \ln 2}{2\pi T} \\
\tau_\sigma &= \frac{\ln 2}{2\pi T} \\
\xi_\sigma &= \xi_C = \frac{4\eta}{2\pi T}
\end{aligned} \tag{3.14}$$

where $N_c^2/(8\pi) = 1/(16\pi G)$, and T is the temperature of the fluid which we measure from the energy density ϵ . The raw materials from which each $T_{\mu\nu}^{(i)}$ is built can be written in terms of CFT stress tensor components as

$$\begin{aligned}
\epsilon &= \frac{1}{2} (T_{tt} - T_{xx} + \Xi) \\
u^x &= \frac{-2T_{tx}}{\sqrt{-4T_{tx}^2 + (T_{tt} + T_{xx} + \Xi)^2}}
\end{aligned} \tag{3.15}$$

where Ξ is defined by (3.10).

3.3 Passing to Minkowski Space

Up to a conformal transformation, $\mathbb{R} \times S^3$ is the covering space of Minkowski space, $\mathbb{R}^{3,1}$. Therefore, we can obtain the CFT stress tensor $T_{ab}^{\mathbb{R}^{3,1}}$ on $\mathbb{R}^{3,1}$ by restricting $T_{\mu\nu}^{\mathbb{R} \times S^3}$ to an appropriate patch of $\mathbb{R} \times S^3$, then conformally mapping to Minkowski space. There are many ways of doing this, simply because there are many ways of positioning the Minkowski space patch within $\mathbb{R} \times S^3$. We will mostly focus on one particular choice of patch which admits a fluid flow reminiscent of a head-on heavy ion collision—though, as on $\mathbb{R} \times S^3$, the initial conditions are characterized by full

stopping rather than approximate rapidity independence. More specifically, the $t = 0$ timeslice in $\mathbb{R} \times S^3$ with time-symmetric bulk initial data as described in Sec.1.4.1, corresponds to an $t' = 0$ timeslice in Minkowski space where the fluid is stationary, and compressed into a region which is axisymmetric and significantly oblate. This is intended to be compared to the state of two heavy nuclei which have just achieved full overlap, though because the initial velocity profile is zero, a better analogy may be a quark-gluon plasma in a trap.

The subsequent evolution of the fluid comprises two distinct types of expansion: longitudinal expansion along the axis of symmetry, and radial expansion. Overall, the flow preserves an $SO(3)$ subgroup of the conformal group $SO(4, 2)$ (as it must since the black hole to which it is dual has an $SO(3)$ symmetry), but due to our choice of embedding of Minkowski space in $\mathbb{R} \times S^3$, this $SO(3)$ is not the obvious one composed of rotations around a point in a single timeslice. Rather, it is the conformal $SO(3)$ symmetry used in [30–33] to study generalizations of Bjorken flow. Rotations around the axis of symmetry of the Minkowski space flow form an $SO(2)$ subgroup of the conformal $SO(3)$ symmetry. The rest of this $SO(3)$ is composed of special conformal transformations, corresponding to conformal Killing vectors of Minkowski space.

In order to map $\mathbb{R} \times S^3$, covered by global coordinates $x^\mu = (\tilde{t}, \tilde{\chi}, \tilde{\theta}, \tilde{\phi})$, to $\mathbb{R}^{1,3}$, covered by coordinates $x^a = (t', x_1, x_2, x_3)$, we use the transformations

$$\begin{aligned}
t'/L &= \frac{\sin \tilde{t}/L}{\cos \tilde{t}/L + \cos \tilde{\chi}} \\
x_1/L &= \frac{\sin \tilde{\chi}}{(\cos \tilde{t}/L + \cos \tilde{\chi})} \sin \tilde{\theta} \cos \tilde{\phi} \\
x_2/L &= \frac{\sin \tilde{\chi}}{(\cos \tilde{t}/L + \cos \tilde{\chi})} \sin \tilde{\theta} \sin \tilde{\phi} \\
x_3/L &= \frac{\sin \tilde{\chi}}{(\cos \tilde{t}/L + \cos \tilde{\chi})} \cos \tilde{\theta}.
\end{aligned} \tag{3.16}$$

The appearance of the AdS scale L on the right hand side of (3.16) is essential: only with this factor will (3.16) lead to a conformal mapping of the metric

$$\begin{aligned} ds_{\mathbb{R} \times S^3}^2 &= g_{\mu\nu}^{\mathbb{R} \times S^3} dx^\mu dx^\nu \\ &= -d\tilde{t}^2 + L^2(d\tilde{\chi}^2 + \sin^2 \tilde{\chi}^2 d\tilde{\theta}^2 + \sin^2 \tilde{\chi}^2 \sin^2 \tilde{\theta}^2 d\tilde{\phi}^2) \end{aligned} \quad (3.17)$$

to the standard Minkowski metric

$$ds_{\mathbb{R}^{3,1}}^2 = g_{ab}^{\mathbb{R}^{3,1}} dx^a dx^b = -(dt')^2 + (dx_1)^2 + (dx_2)^2 + (dx_3)^2. \quad (3.18)$$

The appearance of L on the left hand side of (3.16) is inessential: it could be replaced by any quantity with dimensions of length. Doing so would amount to altering Minkowski space by an uniform dilation of both time and space. The conformal mapping (3.16) is accompanied by the following rule for metric components:

$$g_{ab}^{\mathbb{R}^{3,1}} = W^2 \frac{\partial x^\mu}{\partial x^a} \frac{\partial x^\nu}{\partial x^b} g_{\mu\nu}^{\mathbb{R} \times S^3}, \quad (3.19)$$

where

$$W = \frac{1}{\cos \tilde{t}/L + \cos \tilde{\chi}}. \quad (3.20)$$

The Minkowski space patch on $\mathbb{R} \times S^3$ is the connected region including $(\tilde{t}, \tilde{\chi}) = (0, 0)$ where $W > 0$. This region is easily seen to be the region $-\pi < \tilde{t}/L < \pi$ with $0 \leq \tilde{\chi} < \pi - |\tilde{t}/L|$.

We have used coordinates $(\tilde{t}, \tilde{\chi}, \tilde{\theta}, \tilde{\phi})$ on $\mathbb{R} \times S^3$, instead of our previous coordinates (t, χ, θ, ϕ) , in order to preserve our freedom to position the patch in any way we wish on $\mathbb{R} \times S^3$. For example, we could set $\tilde{t} = t - t_0$ in order to “center” the Minkowski space patch on a global time $t = t_0$. For our current purposes of describing a fluid flow reminiscent of a head-on heavy ion collision, the most useful choice is to set $\tilde{t} = t$,

$\tilde{\phi} = \phi$, and

$$\begin{aligned}\tilde{\chi} &= \frac{\pi}{2} - \arctan\left(\frac{\sin \chi \cos \theta}{\sqrt{\cos^2 \chi + \sin^2 \chi \sin^2 \theta}}\right) \\ \tilde{\theta} &= \frac{\pi}{2} - \arctan(\cot \chi \csc \theta).\end{aligned}\tag{3.21}$$

This mapping is an isometry of S^3 , and composing it with the mapping (3.16) gives

$$\begin{aligned}t'/L &= \frac{\sin t/L}{\cos t/L + \sin \chi \cos \theta} \\ x_1/L &= \frac{\sin \chi}{(\cos t/L + \sin \chi \cos \theta)} \sin \theta \cos \phi \\ x_2/L &= \frac{\sin \chi}{(\cos t/L + \sin \chi \cos \theta)} \sin \theta \sin \phi \\ x_3/L &= \frac{\cos \chi}{(\cos t/L + \sin \chi \cos \theta)}.\end{aligned}\tag{3.22}$$

Additionally, one may show by plugging (3.21) into (3.20) that

$$W = \frac{1}{\cos(t/L) + \cos \theta \sin \chi}.\tag{3.23}$$

The reason that the final mapping (3.22) is a good idea for producing a flow reminiscent of a central heavy ion collision is that the origin of Minkowski space maps to an equatorial point $(\chi, \theta) = (\pi/2, 0)$ on S^3 , where the fluid density is at its peak on the initial timeslice. (Note that the coordinate ϕ on S^3 becomes the usual angle ϕ around the symmetry axis in Minkowski space, but the coordinate θ on S^3 is more closely related to transverse radius from the symmetry axis in Minkowski space than it is to the angle of latitude with respect to the symmetry axis.)

The stress tensor transforms under conformal mappings as

$$T_{ab}^{\mathbb{R}^{3,1}} = W^{-2} \frac{\partial x^\mu}{\partial x^a} \frac{\partial x^\nu}{\partial x^b} T_{\mu\nu}^{\mathbb{R} \times S^3}.\tag{3.24}$$

If we assume the inviscid hydrodynamical form of the stress tensor, $T_{\mu\nu} = \epsilon u_\mu u_\nu + \epsilon \perp_{\mu\nu} / 3$, then one can straightforwardly show that $u_a^{\mathbb{R}^{3,1}} = W \frac{\partial x^\mu}{\partial x^a} u_\mu^{\mathbb{R} \times S^3}$ and $\epsilon^{\mathbb{R}^{3,1}} = W^{-4} \epsilon^{\mathbb{R} \times S^3}$. Up to a constant factor specifying the number of degrees of freedom, the temperature of a conformal fluid is $T = \epsilon^{1/4}$. Setting $L = 1$, the quantity we are going to plot is

$$T \equiv W^{-1} \epsilon^{1/4}, \quad (3.25)$$

where $T = T^{\mathbb{R}^{3,1}}$ is (up to the aforementioned constant factor) the temperature in Minkowski space and $\epsilon = \epsilon^{\mathbb{R} \times S^3}$ is the energy density on $\mathbb{R} \times S^3$.

Chapter 4

Dynamics of Deformed AdS Black Holes

We now describe the dynamics of deformed AdS black holes obtained with the code. First, in Sec. 4.1, we demonstrate that our numerical solutions are converging to solutions of the Einstein field equations at a rate that tends towards one that scales quadratically with mesh spacing. In Sec. 4.2, we show solutions of the Hamiltonian constraint with a scalar field source (2.4), demonstrating that this approach is capable of producing initial data containing trapped surfaces. Then, in Sec. 4.3 we show the evolution of initial data describing highly deformed black holes that subsequently shed their asymmetries via quasi-normal ringdown. A proper extraction of quasi-normal modes, and in particular a meaningful comparison with perturbative calculations where these modes can be defined, requires the identification of a reference background metric and a transformation of the solution to a gauge consistent with that of the perturbative calculations. We have made no attempt in this direction, besides matching the areal radius on the extraction sphere, and do in fact see what appear to be gauge modes. Nevertheless, we can extract the leading order linear quasi-normal modes, and for the higher angular number modes, use a simple forced

harmonic oscillator model to identify what appear to be non-linearly excited harmonics of the lower angular modes. In Sec. 4.4 we discuss the extracted boundary stress energy tensor of these solutions and analyse how well the CFT state can be described by hydrodynamics. We find that the extracted stress energy tensor is consistent, essentially to within numerical truncation error, with that of a viscous, conformal fluid from $t = 0$ onwards. We then transform these solutions onto a Minkowski piece of the boundary, and find an initial fluid geometry that resembles a Lorentz-flattened pancake. Defining the beam-line direction as the one along which the initial data is flattened, the evolution of this fluid exhibits both longitudinal and radial flow relative to the beam-line, with most of the energy flowing along the longitudinal directions.

4.1 Convergence Tests

To check the stability and consistency of our numerical solutions we employ a pair of standard convergence tests. Here we show convergence results from one typical representative case, namely strong scalar field initial data with non-trivial χ -dependence. Specifically, the initial data parameters (2.5) used were $A_0 = 10.0$, $R_0 = 0.0$, $\delta = 0.2$, $w_x = 4.0$, $w_y = 16.0$. The resulting evolution describes a highly deformed black hole which settles down to an AdS-Schwarzschild solution with outermost apparent horizon radius $r_h = 5.0$. The physics of this solution will be discussed in the rest of this chapter, together with additional tests showing conservation of the boundary stress energy tensor.

First, we must determine whether the evolution is stable and consistent. Assuming that the solution admits a Richardson expansion, we compute the rate of convergence $Q(t, x^i)$ at each point on the grid for a given field

$$Q(t, x^i) = \frac{1}{\ln(2)} \ln \left(\frac{f_{4h}(t, x^i) - f_{2h}(t, x^i)}{f_{2h}(t, x^i) - f_h(t, x^i)} \right). \quad (4.1)$$

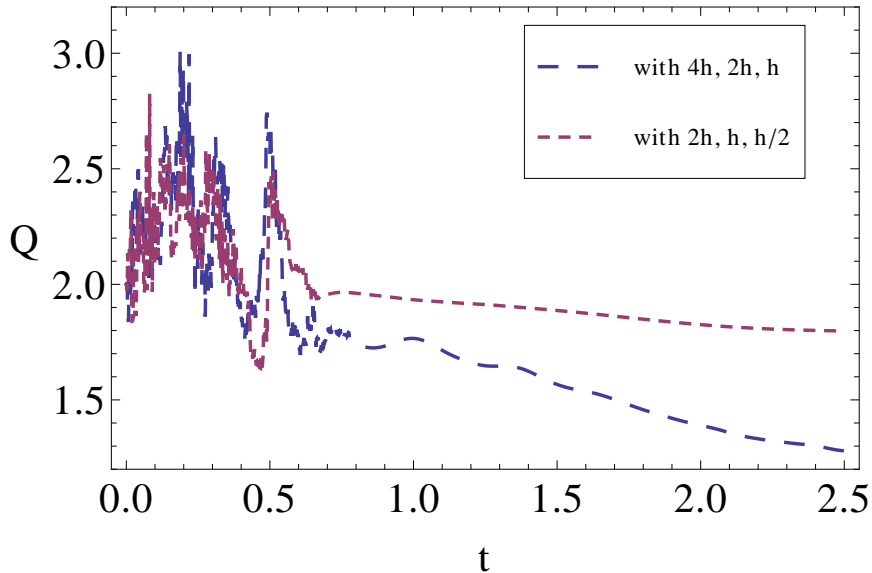


Figure 4.1: Convergence factors (4.1) for the $\bar{g}_{\rho\rho}$ grid function, constructed from a simulation run at 4 different resolutions; the highest resolution run has mesh spacing $h/2$. Here the L^2 -norm of the convergence factors are taken over the entire grid. The trends indicate that this grid function is converging to second-order. Other grid functions exhibit similar trends.

Here, f_Δ denotes one of $\bar{g}_{\mu\nu}, \bar{H}_\mu, \bar{\phi}$ from a simulation with mesh spacing Δ . Given that we use second-order accurate finite difference stencils, with 2 : 1 refinement in Δ between successive resolutions, and similarly in the time-step Δt , since we keep the CFL factor at a constant $\lambda = 0.2$, we expect Q to asymptote to $Q = 2$ in the limit $\Delta \rightarrow 0$.

Second, to determine whether we are converging to the correct solution, i.e. to a solution of the Einstein field equations, we compute an independent residual of the field equations. This is obtained by taking the numerical solution and substituting it into a discretized version of $G_{\mu\nu} + \Lambda_5 g_{\mu\nu} - 8\pi T_{\mu\nu}$. Since the numerical solution was found solving the GH form of the field equations, we do not expect the independent residual to be exactly zero; rather, if the solution is correct the independent residual should be purely numerical truncation error, and hence converge to zero. Thus, we

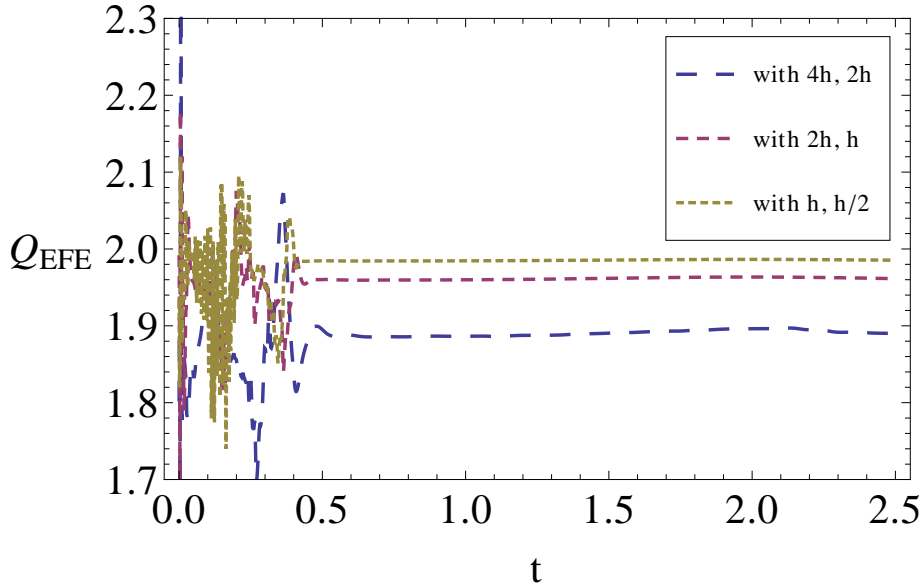


Figure 4.2: Convergence factors for the independent residual (4.2), constructed from simulations run at 4 different resolutions; the highest resolution run has mesh spacing $h/2$. At each point on the grid an L^∞ norm is taken over all components of the independent residual, and what is shown here is then the L^2 -norm of this over the entire grid. The trends in this plot indicate second-order convergence.

can compute a convergence factor for it by using only two resolution results via

$$Q_{EFE}(t, x^i) = \frac{1}{\ln(2)} \ln \left(\frac{f_{2h}(t, x^i)}{f_h(t, x^i)} \right). \quad (4.2)$$

Here, f_Δ denotes a component of $G_{\mu\nu} + \Lambda_5 g_{\mu\nu} - 8\pi T_{\mu\nu}$. Again, given our second-order accurate finite difference stencils and with 2 : 1 refinement in Δ between successive resolutions, we expect Q to approach $Q = 2$ as $\Delta \rightarrow 0$.

Figs. 4.1 and 4.2 show L^2 -norms of (4.1) and (4.2) respectively, obtained from evolving the particular initial data described above. We used 4 different resolutions to help see the trends in the respective Q 's. At early times, the solution is not yet in the asymptotic scaling regime for the convergence factors, however that they are typically greater than 2 indicates that the solution error is nevertheless small. Also,

the trends going to higher resolution, in particular at later times, appear consistent with second-order convergence.

The early-time deviations in Fig. 4.2 coincide with an initial transient associated with the gauge transition described by (2.32), that emanates from the boundary and dissipates as it travels further into the interior. This transient is clearly seen as a temporary dip in the *point-wise* convergence factors for independent residuals near the boundary; taking the L^2 -norm as was done in Fig. 4.2 to some extent masks this dip, though is still visible with the highest resolution curve in that plot. Nevertheless, this transient converges away in the sense that the region of the domain affected shrinks as resolution is increased.

4.2 Strong-field Solutions of the Hamiltonian Constraint

To generate black holes spacetimes, we choose initial data where the deviation from pure AdS is sourced by a highly compact distribution of scalar field energy, with profile given by (2.5). In this dissertation we only consider free, massless scalar fields, so $V(\phi) = 0$ in (2.3). In this section, we begin by focusing on spherically symmetric initial data, so $w_x = w_y = 1$ in (2.5).

Fig. 4.3 summarizes solutions of the Hamiltonian constraint (2.4) by plotting the maximum value of the conformal factor versus the maximum of the scalar field (both maxima occur at the origin of the domain for these initial data). Let us begin by contrasting the qualitative behavior of this plot with its counterpart in the asymptotically flat case, presented in [58]. This earlier work employed the conformal thin sandwich method to solve the constraints. There, it was discovered that there exists a critical point above which no numerical solutions for the initial data could be found, and where the conformal factor diverges as the amplitude approaches the critical

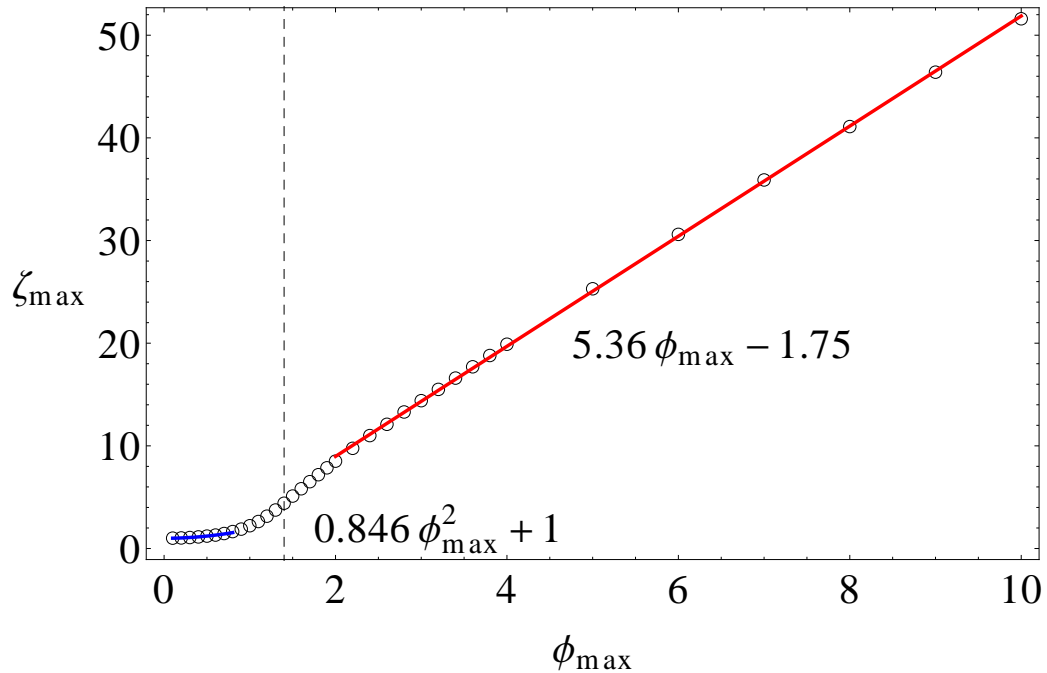


Figure 4.3: Maximum conformal factor vs. maximum amplitude of an initial scalar matter distribution, with Gaussian profile (2.3) with $A = \phi_{\max}$, $\delta = 0.2$ (with AdS scale $L = 1$), $w_x = w_y = 1$ and $R_0 = 0$. We differentiate between “strong-field” and “weak-field” data based on whether there is a trapped surface present on the initial slice or not, respectively. (Though of course this distinction is somewhat arbitrary, particularly since subsequent evolution of weak-field data could eventually result in black hole formation, as argued in [19] even for arbitrarily small amplitude initial data.) The value of ϕ_{\max} beyond which trapped surfaces are found in the initial data is indicated by the dashed vertical line. The open circles denote numerical solutions, while the solid lines are fits to the data, as shown.

point. Even more surprisingly, it was found that generalizing to the extended conformal thin sandwich method gives rise to a branch point instead of a critical point, with solutions along the upper branch exhibiting non-uniqueness for any given set of initial data.

In contrast, we find no divergent behavior in the conformal factor, nor any behavior suggesting the non-uniqueness of solutions ϕ_{\max} , at least in the regime where the cosmological length scale is relevant¹. Furthermore, the linear dependence of

¹We have not investigated the limit where the characteristic scale in the initial data δ is much less than the cosmological scale L , where one might intuitively expect L to become irrelevant in governing

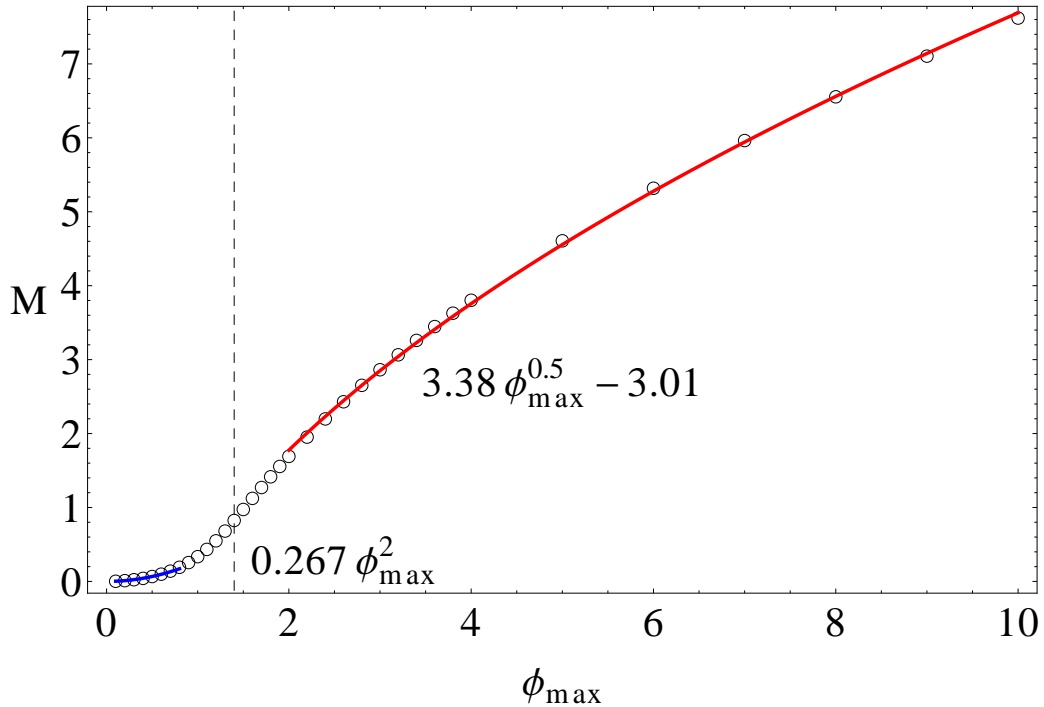


Figure 4.4: AdS mass vs. maximum amplitude of massless scalar matter, with Gaussian profile defined by $A = \phi_{\max}$, $(x_0, y_0) = (0, 0)$, $\delta = 0.2$. Conventions are the same as those used in Fig. 4.3. In cases where trapped surfaces are present (to the right of the dashed vertical line), an estimate of the mass based on the area of the apparent horizon gives a value very close the asymptotic mass plotted here, though systematically smaller (the two values would essentially be indistinguishable on the scale of this figure, hence we only show the asymptotic mass to avoid clutter).

the maximum of the conformal factor versus amplitude for large amplitude data suggests that the AdS₅ Hamiltonian constraint admits conformal solutions for arbitrarily strong initial matter distributions. Of course, given the presence of the cosmological constant and its relevance on these scales, it is not too surprising that we find such qualitatively different behavior compared to the asymptotically flat case. From a more formal perspective, the local existence and uniqueness of solutions to non-linear elliptic PDEs can be understood by applying a maximum principle, where the signs and relative magnitudes of coefficients in the PDE are crucial; from standard

the local nature of the solution, and results consistent with the asymptotically flat case [58] may be recovered.

results [59] in the theory of elliptic PDEs, it is easy to see that a negative cosmological constant helps to ensure that such a maximum principle holds.

Fig. 4.4 shows a plot of the conserved mass M of the spacetime versus scalar field amplitude, computed from the quasi-local stress tensor (3.3) as follows. We take a spatial $t = \text{const.}$ (here $t = 0$) slice in ∂M_q , with induced 3-metric $\sigma_{\mu\nu}$, lapse N and shift N^i such that $\Sigma_{\mu\nu} dx^\mu dx^\nu = -N^2 dt^2 + \sigma_{ij}(dx^i + N^i dt)(dx^j + N^j dt)$, then compute

$$M = \lim_{q \rightarrow 0} \int_{\Sigma} d^3x \sqrt{\sigma} N {}^{(q)}T_{\mu\nu} u^\mu u^\nu \quad (4.3)$$

where u^μ is the time-like unit vector normal to $t = \text{const.}$ Note that for a vacuum AdS-Schwarzschild black hole, this prescription gives a result consistent with the usual definition of its mass from the analytic solution, namely $M = 3\pi (r_0^2/8)$, where $r_0 = r_H \sqrt{1 + r_H^2/L^2}$, given a horizon with areal radius r_H .

4.3 Quasinormal Ringing

As a first application of our evolution scheme, we study the quasi-normal ringdown of an initially highly distorted (i.e. non-spherical) black hole. Here we focus on the dynamics of the bulk, and in the following sections discuss the corresponding dynamics of the CFT boundary stress tensor. For some previous work on the subject see for example [60–65]. For a review of black hole quasi-normal modes in AdS see [66]. Again, we use large-amplitude scalar field data to create an initial slice of the spacetime containing a trapped surface, and here introduce a non-trivial χ -dependence by adjusting the shape of the profile through the parameters w_x and w_y as defined in (2.5). Specifically, unless otherwise stated we choose $R_0 = 0.0$, $\delta = 0.2$, $w_x = 4.0$, $w_y = 16.0$, and vary the amplitude A_0 to control the size of the resultant black hole.

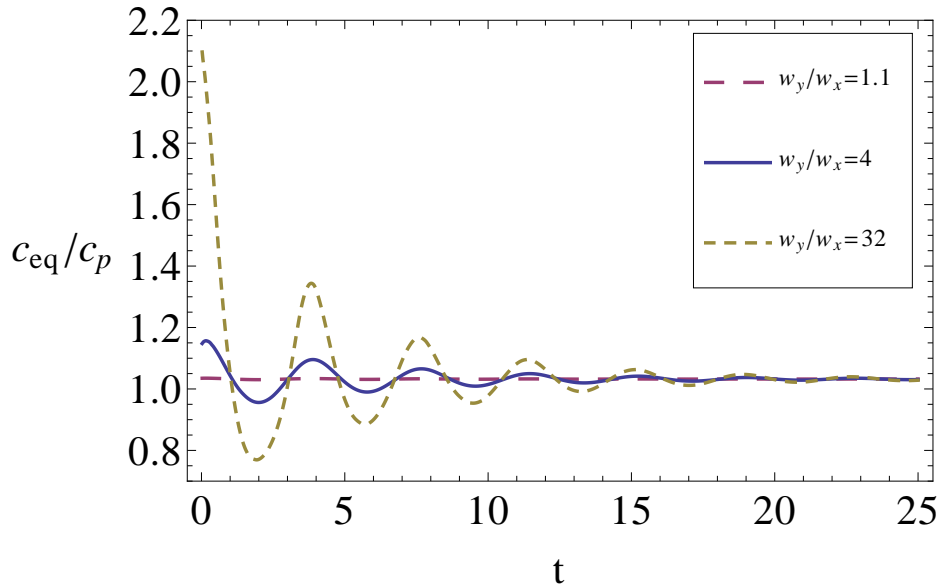


Figure 4.5: The ratio c_{eq}/c_p of proper equatorial to polar circumference of the apparent horizon versus time. w_y/w_x denotes parameters in the initial data describing the scalar field profile (2.5), and $w_y/w_x = 4$ is the canonical case studied in this dissertation, though for interest we also show examples representing a weaker and stronger initial asymmetry. In all cases, the final black hole has radius $r_h \approx 5$. Note that a geometric sphere has $c_{eq}/c_p = 1$, whereas a geometric disk has $c_{eq}/c_p = \pi/2$. Thus, even the $w_y/w_x = 4$ case is initially a rather large deformation of the 3-sphere; the curve for the more extreme case $w_y/w_x = 32$ implies that at early times the Gaussian curvature is negative over at least some regions of the horizon.

First, to demonstrate that we are looking at relatively large perturbations of the spherical black hole, in Fig. 4.5 we plot the ratio of the equatorial c_{eq} to polar c_p proper circumferences of the apparent horizon versus time². A geometric sphere has $c_{eq}/c_p = 1$, whereas a geometric disk $c_{eq}/c_p = \pi/2$. Initial data with parameters w_x, w_y such that $w_y/w_x = 4$, which was the case that was studied in detail in Sec. 4.1, corresponds to a ratio of $c_{eq}/c_p(t = 0) \approx 1.2$, indicating a fairly sizeable initial deformation. For certain quasi-normal mode and hydrodynamic extraction results

²Note that the apparent horizon is to some extent slicing dependent. However, given the symmetries in our problem, in particular that $t = 0$ is a moment of time-symmetry (where we see the largest deformation of the horizon), it is difficult to imagine how the intrinsic geometry of the apparent horizon does not give a good indication of the relative magnitude of the spacetime perturbation.

in the following sections, we will also consider initial data with w_x, w_y such that $w_y/w_x = 32$, which corresponds to a very large initial deformation $c_{eq}/c_p(t=0) \approx 2.2$.

To extract the quasi-normal modes, the first step would be to transform our metric to a gauge consistent with standard perturbative calculations for quasi-normal modes. This is a rather non-trivial step in general, and we do not take it here. Nevertheless, as we shall see, our asymptotic gauge choice is sufficiently close to that of the perturbative calculations. This is supported by the fact that artifacts introduced by our non-standard gauge choice, which take the form of modes that are pure gauge, are very small in amplitude relative to the quasi-normal modes.

The spatial dependence of quasi-normal modes in AdS_5 can be decomposed into the spherical harmonics of S^3 ; see [67]. Recall the standard spherical harmonics on S^2 :

$$Y_{lm}(\theta, \phi) = \sqrt{\frac{2l+1}{4\pi} \frac{(l-m)!}{(l+m)!}} P_l^m(\cos \theta) \exp(im\phi) \quad (4.4)$$

where the associated Legendre polynomials are defined as:

$$P_l^m(x) = \frac{(-1)^m}{2^l l!} \frac{d^{l+m}}{dx^{l+m}} (x^2 - 1)^l. \quad (4.5)$$

The scalar³ spherical harmonics on S^3 are then given by:

$$\begin{aligned} \mathbb{S}(klm) &= (-1)^k i^l (2l)!! \sqrt{\frac{2(k+1)(k-l)}{\pi(k+l+1)!}} \\ &\quad \times C_{k-l}^{l+1}(\cos \chi) \sin^l(\chi) Y_{lm}(\theta, \phi) \end{aligned} \quad (4.6)$$

³In addition to the scalar harmonics, the metric also in general admits vector $\mathbb{V}(klm)$ ($1 \leq l \leq k$) and tensor harmonics $\mathbb{T}(klm)$ ($2 \leq l \leq k$), but our $SO(3)$ symmetry precludes the excitation of these modes: the vector and tensor harmonics require θ dependence (i.e. $l \neq 0$) that our symmetry does not allow.

where the Gegenbauer polynomials are defined as:

$$C_k^a(x) = \frac{(-2)^k \Gamma(k+a)\Gamma(k+2a)}{k! \Gamma(a)\Gamma(2k+2a)} (1-x^2)^{-a+1/2} \times \frac{d^k}{dx^k} (1-x^2)^{k+a-1/2}. \quad (4.7)$$

Our restriction to solutions that preserve a symmetry in θ, ϕ mandates that we have $l = 0, m = 0$.

The time dependence of the quasi-normal modes are described by a sum of damped sinusoids of the form

$$A_n \exp(-i\omega_n t - i\varphi_n). \quad (4.8)$$

Here, A_n is the amplitude of a mode with frequency $\omega_n = \omega_{nr} + i\omega_{ni}$ and phase φ_n . The integer n indexes the mode frequency: $n = 0$ denotes the lowest frequency, or *fundamental*, and each $n > 0$ denotes the n^{th} *overtone*.

4.3.1 Scalar Spherical Harmonics of the Metric

For the metric, the $\mathbb{S}(klm)$ scalar harmonics are restricted by $0 \leq l \leq k$. The $k = 1$ mode is not associated with any physical degrees of freedom [68], and these can be ignored; indeed our choice of initial data where the scalar field profile is symmetric about $\chi = \pi/2$ prevent these from being excited. The $k = 0$ mode corresponds to a perturbation of a black hole that is itself spherically-symmetric in all the S^3 angles χ, θ, ϕ . Thus, as a consequence of Birkhoff's theorem, we might also expect to ignore this $k = 0$ case as we have with $k = 1$. However, despite this reasoning, we *see* non-trivial dynamics in the data's projection onto the $k = 0$ scalar harmonic. To understand why, recall that we *have not* transformed our metric to a gauge that is consistent with the standard one assumed by the perturbative calculations for quasi-normal modes. Consequently, the metric components that we extract generally

contain both physical quasi-normal modes as well as contributions from gauge modes that are introduced by our non-standard choice of time-slicing, and of the r and χ coordinates on each slice. This gauge contribution is of course present in the data for all k , and is most obvious in the $k = 0$ projection since it contains no physical quasi-normal modes. For $k \geq 2$, this gauge contribution manifests itself as a decaying mode (i.e. a mode whose frequency has a negligibly small real part). In the following, we consider the $k \geq 2$ modes of the metric, taking into account this gauge contribution.

Fig. 4.6 shows a representative metric variable projected onto the $\mathbb{S}(200)$ ($k = 2$) scalar harmonic, for a simulation with final state horizon radius $r_h = 5$ and initial asymmetry $w_y/w_x = 4$. The quasi-normal mode frequencies extracted from this representative metric variable are displayed in Table 4.1. This analysis was repeated for several simulations with varying r_h but fixed $w_y/w_x = 4$. Fits to damped sinusoids yield $n = 0$ fundamental frequencies with imaginary parts ω_i that scale as $\sim 1/r_h$, and real parts ω_r that are largely insensitive to these changes in r_h .

Obtaining the $\mathbb{S}(200)$ harmonic's $n = 1$ overtone from the metric variables is more difficult, largely because it decays much more quickly than the $n = 0$ fundamental. To obtain good fits, we focus on an early-time segment of the data, and subtract the $n = 0$ fit, then fit to the remainder. The quasi-normal frequencies extracted in this way are tabulated in Table 4.2. This table shows that the $n = 1$ fundamental frequencies ω_r and ω_i both scale linearly with r_h . To compare with earlier work, notice that these extracted frequencies for the $n = 1$ overtone are a close match to the first set of “fast-modes” found in [65], and that the extracted frequencies for the $n = 0$ fundamental closely match the low-lying “slow-modes” found in the same study.

Discrepancies with the linear quasi-normal mode description start to appear in the next highest scalar harmonic $\mathbb{S}(400)$ ($k = 4$): direct fitting yields a dominant frequency that does not match [65]. The $k = 4$ fundamental mode with frequency

fund.	k=2
$\frac{r_h}{L}=12.2$	$(1.640 \pm 0.007) - i(0.902 \pm 0.067) \frac{L}{r_h}$
$\frac{r_h}{L}=11.3$	$(1.640 \pm 0.005) - i(0.895 \pm 0.058) \frac{L}{r_h}$
$\frac{r_h}{L}=10.5$	$(1.641 \pm 0.002) - i(0.876 \pm 0.039) \frac{L}{r_h}$
$\frac{r_h}{L}=9.0$	$(1.643 \pm 0.003) - i(0.864 \pm 0.028) \frac{L}{r_h}$
$\frac{r_h}{L}=6.5$	$(1.650 \pm 0.0007) - i(0.841 \pm 0.010) \frac{L}{r_h}$
$\frac{r_h}{L}=5.0$	$(1.661 \pm 0.0006) - i(0.837 \pm 0.005) \frac{L}{r_h}$
$\frac{r_h}{L}=4.5$	$(1.666 \pm 0.0006) - i(0.823 \pm 0.004) \frac{L}{r_h}$
$\frac{r_h}{L}=4.0$	$(1.675 \pm 0.0005) - i(0.823 \pm 0.003) \frac{L}{r_h}$
$\frac{r_h}{L}=3.3$	$(1.692 \pm 0.0004) - i(0.808 \pm 0.002) \frac{L}{r_h}$

Table 4.1: The fundamental ($n = 0$) quasi-normal mode frequencies $\omega_r - i\omega_i$ extracted from the metric variable $\bar{g}_{\chi\chi}$. These are shown for various horizon radii r_h of the final state AdS-Schwarzschild black hole and for $SO(4)$ quantum numbers $k = 2, l = 0, m = 0$. Uncertainties are estimated from convergence studies.

1 st overt.	k=2
$\frac{r_h}{L}=12.2$	$(3.497 \pm 0.131) \frac{r_h}{L} - i(2.087 \pm 0.142) \frac{r_h}{L}$
$\frac{r_h}{L}=11.3$	$(3.320 \pm 0.156) \frac{r_h}{L} - i(2.185 \pm 0.174) \frac{r_h}{L}$
$\frac{r_h}{L}=10.5$	$(3.378 \pm 0.339) \frac{r_h}{L} - i(2.120 \pm 0.368) \frac{r_h}{L}$
$\frac{r_h}{L}=9.0$	$(3.256 \pm 0.078) \frac{r_h}{L} - i(2.100 \pm 0.125) \frac{r_h}{L}$
$\frac{r_h}{L}=6.5$	$(3.329 \pm 0.178) \frac{r_h}{L} - i(2.091 \pm 0.091) \frac{r_h}{L}$
$\frac{r_h}{L}=5.0$	$(3.103 \pm 0.264) \frac{r_h}{L} - i(2.626 \pm 0.495) \frac{r_h}{L}$
$\frac{r_h}{L}=4.5$	$(3.217 \pm 0.084) \frac{r_h}{L} - i(2.718 \pm 0.130) \frac{r_h}{L}$
$\frac{r_h}{L}=4.0$	$(3.274 \pm 0.051) \frac{r_h}{L} - i(2.688 \pm 0.070) \frac{r_h}{L}$
$\frac{r_h}{L}=3.3$	$(3.318 \pm 0.059) \frac{r_h}{L} - i(2.914 \pm 0.307) \frac{r_h}{L}$

Table 4.2: The first overtone ($n = 1$) quasi-normal mode frequencies $\omega_r - i\omega_i$ extracted from the metric variable $\bar{g}_{\chi\chi}$. These are shown for various horizon radii r_h of the final state AdS-Schwarzschild black hole and for $SO(4)$ quantum numbers $k = 2, l = 0, m = 0$. Uncertainties are estimated from convergence studies.

$\omega_4 \approx 2.949 + i3.428/r_h$ is present, but is overshadowed by a mode with frequency $\omega_4^{dbl} \approx 3.312 + i1.627/r_h$, which is close to double that of the $k = 2$ fundamental $\omega_2 \approx 1.652 + i0.826/r_h$ that appears in Table 4.1. We expect that this frequency-doubling in the $k = 4$ modes arises from a non-linear mode-coupling, which we attempt to model as a damped harmonic oscillator driven at double the frequency of the $k = 2$ fundamental mode. Given a $k = 2$ fundamental mode $\Psi_2(t) = A_2 \exp(-i\omega_2 t)$, the

$k = 4$ mode $\Psi_4(t)$ in this simple model satisfies

$$\partial_t^2 \Psi_4 + k_4^2 \Psi_4 - \lambda_4 \partial_t \Psi_4 = B \exp(-2i\omega_2 t), \quad (4.9)$$

$\lambda_4 = \omega_{4i}$, $k_4^2 = (\omega_{4r})^2 + (\omega_{4i})^2$ (with the r and i subscripts denoting the real and imaginary components of the corresponding number respectively), and we expect the driving amplitude B to scale as $B \sim (A_2)^2$.

The solution of (4.9) is a sum of the $k = 4$ fundamental and the driven mode

$$\Psi_4(t) = A_4 \exp(-i\omega_4 t) + A_4^{dbl} \exp(-2i\omega_2 t), \quad (4.10)$$

where A_4 is a constant depending on the initial data, and A_4^{dbl} is a (complex) constant depending upon the other parameters of the model via

$$A_4^{dbl} = (\tilde{\omega}_r + i\tilde{\omega}_i)^{-1} B, \quad (4.11)$$

where we have introduced for notational convenience $\tilde{\omega}_i = 4\omega_{2r}(2\omega_{2i} - \omega_{4i})$ and $\tilde{\omega}_r = (\omega_{4r})^2 + (\omega_{4i})^2 - 4((\omega_{2r})^2 - (\omega_{2i})^2 + \omega_{4i}\omega_{2i})$.

$\frac{w_y}{w_x}$	A_4	A_4^{dbl}	A_4^g
1.1	$(1.49 \pm 0.09) \times 10^{-3}$	$(6.44 \pm 0.02) \times 10^{-3}$	$(4.40 \pm 0.03) \times 10^{-4}$
4	2.75 ± 0.01	9.62 ± 0.01	0.508 ± 0.030
32	$(5.39 \pm 0.04) \times 10^1$	$(1.16 \pm 0.01) \times 10^2$	1.59 ± 0.06
$\frac{w_y}{w_x}$	ω_{4i}^g	$\Delta\varphi$	$\frac{A_4^{dbl}}{(A_2)^2} \times 10^3$
1.1	$(1.23 \pm 0.23) \frac{L}{r_h}$	0.832 ± 0.011	4.03 ± 0.02
4	$(1.26 \pm 0.04) \frac{L}{r_h}$	0.873 ± 0.032	4.00 ± 0.02
32	$(1.16 \pm 0.01) \frac{L}{r_h}$	0.894 ± 0.066	4.60 ± 0.02

Table 4.3: Extracted parameters from the $k = 4$ fit corresponding to Fig. 4.7 at $w_y/w_x = 4$, as well as for the largest and smallest w_y/w_x cases considered. The fit includes the fundamental $k = 4$ mode with extracted amplitude A_4 , a mode that has twice the frequency of the $k = 2$ fundamental mode with extracted amplitude A_4^{dbl} , and a putative gauge mode $A_4^g \exp(-\omega_{4i}^g t)$. The model for the mode coupling discussed in the text predicts a phase difference between the frequency-doubled $k = 4$ mode and its $k = 2$ fundamental mode source of $\Delta\varphi \sim 0.842$, and that A_4^{dbl} scales as the square A_2 ; these two quantities are shown in the last two columns of the table, and indicate the solution is reasonably consistent with the model. Uncertainties are estimated via convergence.

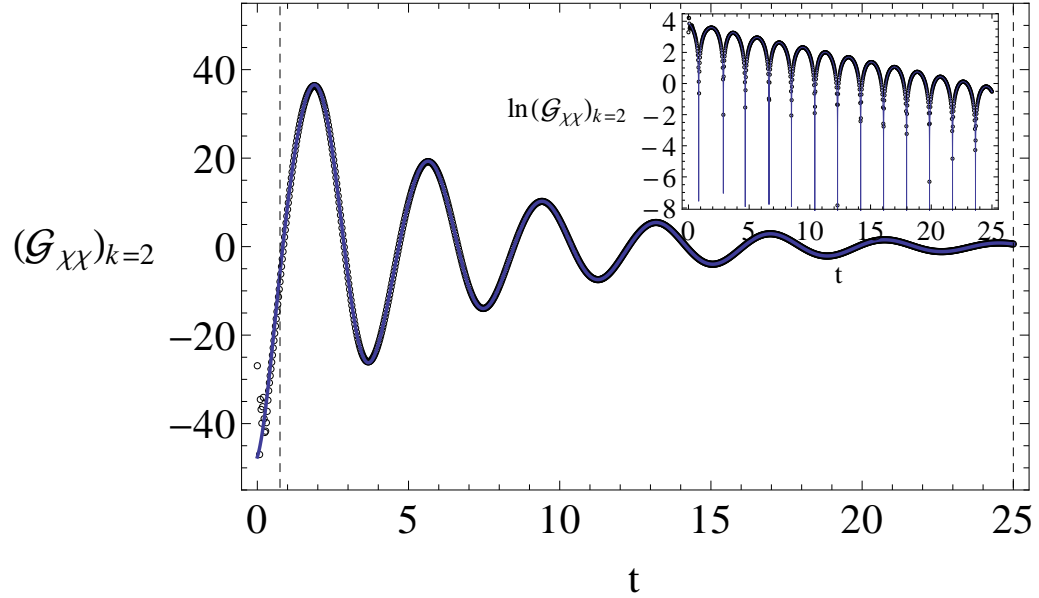


Figure 4.6: The leading-order behavior of the metric variable \bar{g}_{XX} near the boundary $q = 0$, projected onto the $\mathbb{S}(200)$ scalar harmonic by $(\mathcal{G}_{XX})_{k=2} = \int d\Omega_3 (\bar{g}_{XX}/q) \mathbb{S}(200)$, plotted over a global time interval of $t \in [0, 8\pi]$ (open circles). A fit (solid line) $(\mathcal{G}_{XX})_{k=2}^{fit} = A_2 \exp(-i\omega_2 t - i\varphi_2)$ is extracted using the data inbetween the dashed vertical lines, giving $A_2 = 39.8$, $\omega_2 = 1.661 + i0.837/r_h$, and $\varphi_2 = 1.05$. The inset shows a logarithmic plot of the data and the fit over the full global time interval. Other metric variables show similar behavior.

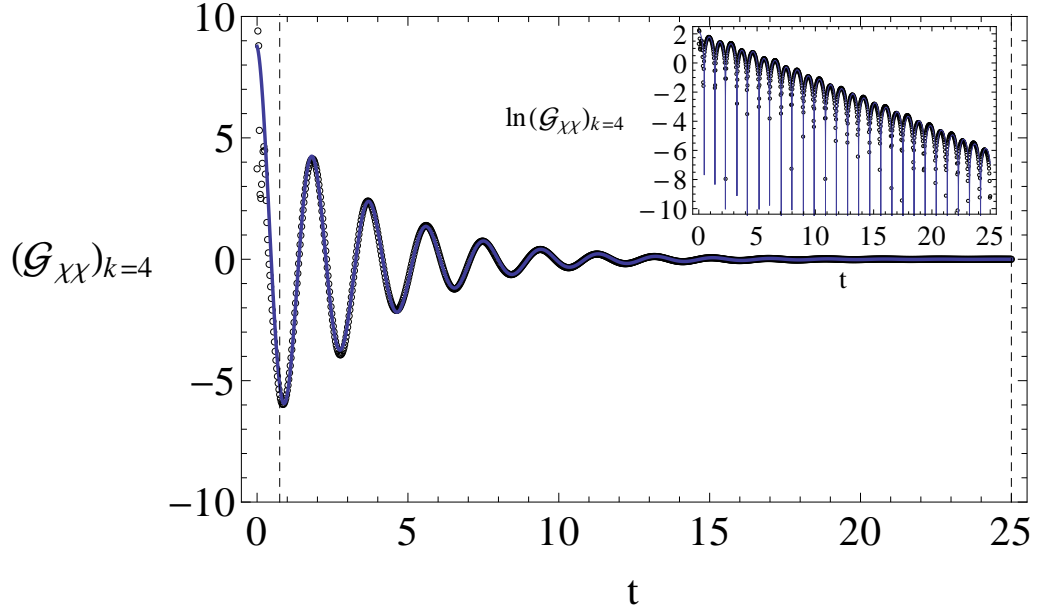


Figure 4.7: The leading-order behavior of the metric variable \bar{g}_{XX} near the boundary $q = 0$, projected onto the $\mathbb{S}(400)$ scalar harmonic by $(\mathcal{G}_{XX})_{k=4} = \int d\Omega_3 (\bar{g}_{XX}/q) \mathbb{S}(400)$, plotted over a global time interval of $t \in [0, 8\pi]$ (open circles). A fit (solid line) $(\mathcal{G}_{XX})_{k=4}^{fit} = A_4^g \exp(-i\omega_{4i}^g t) + A_4 \exp(-i\omega_4 t - i\varphi_4) + A_4^{dbl} \exp(-i\omega_4^{dbl} t - i\varphi_4^{dbl})$ is extracted using the data inbetween the dashed vertical lines. This is a fit to a gauge mode, and two damped sinusoids with fixed frequencies $\omega_4 \approx 2.949 + i3.428/r_h$ and $\omega_4^{dbl} = 2\omega_2 \approx 2 \times (1.652 + i0.826/r_h)$ (see Table 4.3 for the corresponding parameters of the fit). The inset shows a logarithmic plot of the data and the fit over the full global time interval. Other metric variables show similar behavior.

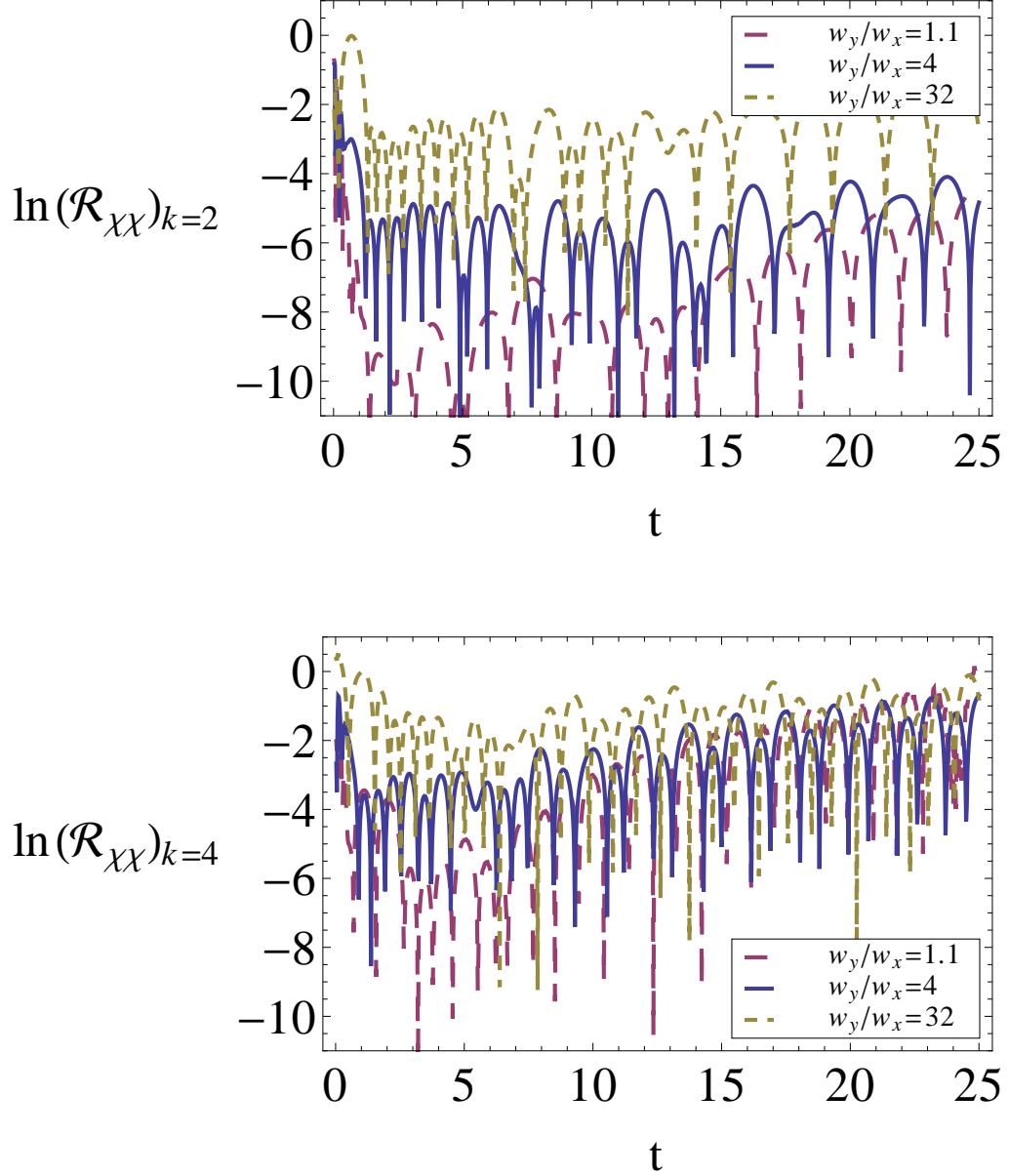


Figure 4.8: The normalized residuals for the $k = 2$ and $k = 4$ fits, corresponding to Fig. 4.6 and Fig. 4.7, respectively, where $(\mathcal{R}_{\chi\chi})_k = \left((\mathcal{G}_{\chi\chi})_k - (\mathcal{G}_{\chi\chi})_k^{fit} \right) / \left| (\mathcal{G}_{\chi\chi})_k^{fit} \right|$. This quantity shows the extent to which the projection of the metric element $\bar{g}_{\chi\chi}$ onto the $\mathbb{S}(k00)$ harmonic *fails* to be described by the sum of the k quasi-normal mode, gauge mode, and for the $k = 4$ case the non-linear mode. At times before $t \approx 1$, the residual becomes large going to smaller t due to a growing phase offset between the data and the fit, and at very early times there is an additional contribution from the early-time transient. There is a slight increase in the residual at late times, because the deformation decays exponentially, so a small phase difference between the fit and data will result in a normalized residual that grows with time.

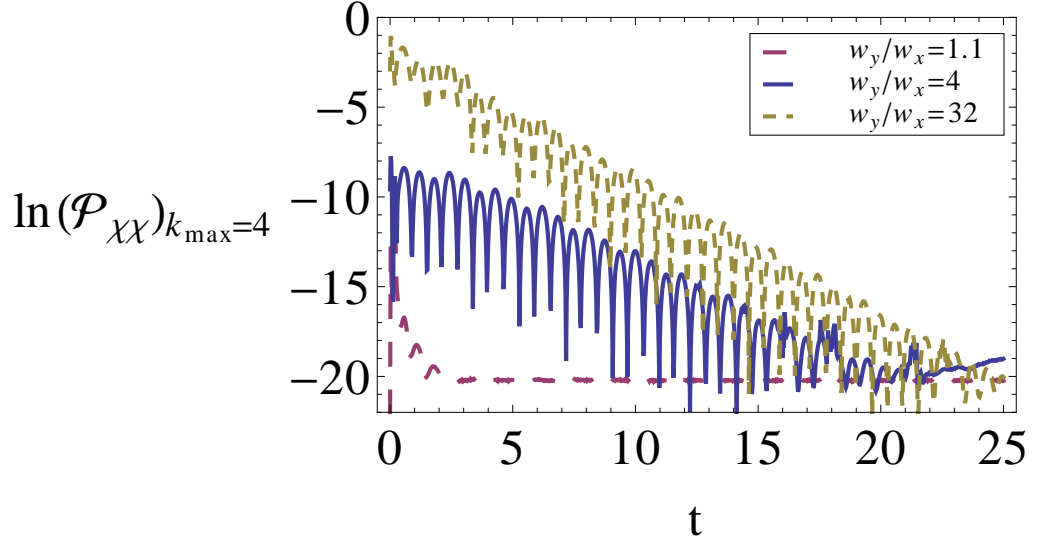
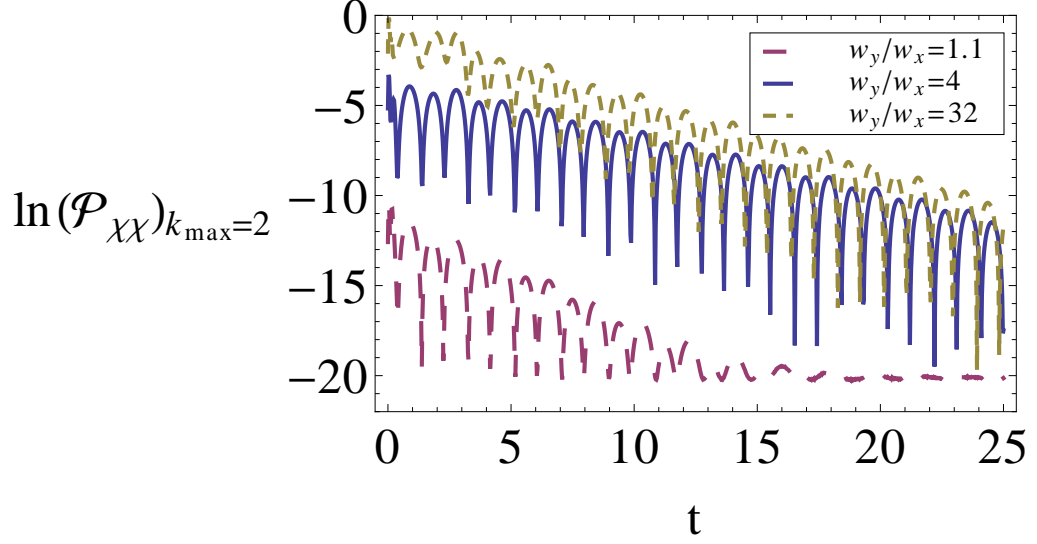


Figure 4.9: The normalized difference $(\mathcal{P}_{\chi\chi})_{k_{max}} = \left(\int d\Omega_3 (\bar{g}_{\chi\chi}/q)^2 - \sum_{k=0}^{k=k_{max}} (\mathcal{G}_{\chi\chi}_k)^2 \right) / \left| \int d\Omega_3 (\bar{g}_{\chi\chi}/q)^2 \right|$. For the $w_y/w_x = 4$ case, the contribution due to the $k > 2$ ($k > 4$) modes constitutes $\approx 2\%$ ($\approx 0.1\%$) of the metric perturbation, and decreases with time (the metric modes decay faster with higher k).

Our strategy is to compare the predictions of this simplified model of non-linear mode-mixing to the parameters extracted from the fits. In particular (4.11) gives us quantitative predictions for the relative amplitude and phase difference between the frequency-doubled $k = 4$ mode and the $k = 2$ fundamental mode that sources it: that the phase difference should be $\Delta\varphi = \arctan(\tilde{\omega}_i/\tilde{\omega}_r)$, and that A_4^{dbl} should scale as $(A_2)^2$. To test these predictions, we fit the $k = 4$ data to two damped sinusoids simultaneously (in addition to the decaying gauge mode), though *fixing* their frequencies to ω_4 and $2\omega_2$. We can then check if the extracted amplitude and phase of the frequency doubled mode matches the model prediction. The results, presented in Table 4.3 for three values of w_y/w_x , and an example fit is shown in Fig. 4.7 for the $w_y/w_x = 4$ case, show good agreement with the model.

To quantify precisely how well the fits describe the actual data, we compute a residual that measures the difference between the data and the fits. This residual quantifies the part of the dynamics that we have not been able to fit to with linear quasi-normal modes supplemented by the pure decay gauge mode, and in the $k = 4$ case, the mode arising from non-linear mode-mixing modeled by (4.9). The solid blue curve of the first panel of Fig. 4.8 depicts a normalized residual that is generated from the fit shown in Fig. 4.6.

To illustrate the dependence on w_y/w_x , this analysis is repeated for the largest and smallest w_y/w_x we have considered. The solid blue curve shows that the fit to the $k = 2$ fundamental quasi-normal mode for $t \gtrsim 1$ captures all but $\approx 1\%$ of the perturbation projected onto the $\mathbb{S}(200)$ harmonic, for the $w_y/w_x = 4$ case. The other curves show that a similar fit does worse for larger w_y/w_x , which is consistent with the expectation that other unmodeled effects (i.e. those not accounted for by the linear quasi-normal modes and our simplified model of the gauge and non-linear effects) should become more significant for data with larger deformations. Similarly, the solid blue curve of the second panel in Fig. 4.8 depicts the normalized residual

corresponding to the fit shown in Fig. 4.7. It shows that for $t \gtrsim 1$, the fit to the fixed-frequency $k = 4$ fundamental mode, the frequency-doubled $k = 2$ mode and single gauge mode captures all but $\approx 5\%$ of the solution projected onto the $\mathbb{S}(400)$ harmonic for $w_y/w_x = 4$. Again, the corresponding residual grows with larger initial asymmetry.

Finally, to quantify how much of the full solution is not accounted for by the $\mathbb{S}(200)$ and $\mathbb{S}(400)$ harmonics that we discussed above, we look at the normalized difference between the square of the full solution integrated over the 3-sphere, and the sum of the squares of all projections onto the $\mathbb{S}(k00)$ harmonics for all $k \leq k_{max}$. The result of this procedure is summarized in Fig. 4.9.

4.3.2 Scalar Spherical Harmonics of the Scalar Field

For perturbations of the scalar field, these $\mathbb{S}(klm)$ scalar harmonics exist for all $k \geq 0$. Fig. 4.10 shows the scalar field projected onto the 3-sphere ($k = 0$), for a simulation with initial $w_y/w_x = 4$ and whose final state black hole has horizon radius $r_h = 5$. The quasi-normal mode frequencies extracted from the scalar field are collected in Table 4.4 for the $n = 0$ fundamental mode and Table 4.5 for the $n = 1$ first overtone.

This was done for several r_h cases, wherein each pair of fundamental and first overtone was found by a simultaneous non-linear least-squares fit to two damped sinusoids, corresponding to the $n = 0$ fundamental and the $n = 1$ overtone, each of the form (4.8). The $n = 0$ fundamental frequencies ω_r and ω_i scale linearly with r_h , and their dependence on k shows that ω_r increases with k and that ω_i decreases with k . The $n = 1$ first overtone frequencies ω_r and ω_i also scale linearly with r_h , as with the $n = 0$ frequencies; however, the dependence on k differs from the $n = 0$ fundamental case in that the ω_r and ω_i both increase with k . To make contact with earlier work on quasi-normal modes in AdS, we note that the frequencies extracted for the $n = 0$ fundamental are a close match to those found in the seminal study [60] on this subject.

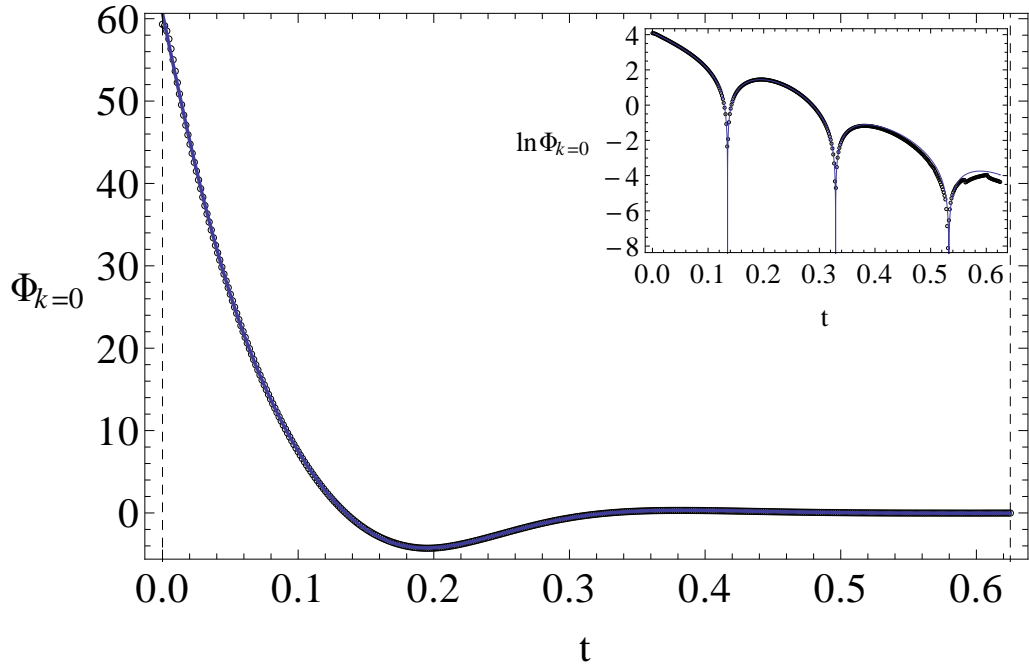


Figure 4.10: The leading-order behavior of the scalar field variable $\bar{\phi}$ near the boundary $q = 1$, projected onto the 3-sphere by $\Phi_{k=0} = \int d\Omega_3 (\bar{\phi}/q) \mathbb{S}(000)$, and plotted over a global time interval of $t \in [0, 0.62]$ (open circles). A fit (solid line) $\Phi_{k=0}^{fit} = A_0 \exp(-i\omega_0 t - i\varphi_0)$ is extracted using the data inbetween the dashed vertical lines, giving $A_0 = 64.4$, $\omega_0 = 3.11r_h - i2.62r_h$, and $\varphi_0 = -0.454$. The inset shows a logarithmic plot of the data and the fit over the full global time interval.

fund.	k=0
$\frac{r_h}{L}=12.2$	$(2.95 \pm 0.13) \frac{r_h}{L} - i(2.67 \pm 0.02) \frac{r_h}{L}$
$\frac{r_h}{L}=11.3$	$(2.95 \pm 0.14) \frac{r_h}{L} - i(2.64 \pm 0.04) \frac{r_h}{L}$
$\frac{r_h}{L}=10.5$	$(2.96 \pm 0.14) \frac{r_h}{L} - i(2.64 \pm 0.05) \frac{r_h}{L}$
$\frac{r_h}{L}=9.0$	$(2.99 \pm 0.15) \frac{r_h}{L} - i(2.63 \pm 0.07) \frac{r_h}{L}$
$\frac{r_h}{L}=6.5$	$(3.06 \pm 0.14) \frac{r_h}{L} - i(2.62 \pm 0.14) \frac{r_h}{L}$
$\frac{r_h}{L}=5.0$	$(3.11 \pm 0.09) \frac{r_h}{L} - i(2.62 \pm 0.20) \frac{r_h}{L}$
$\frac{r_h}{L}=4.5$	$(3.18 \pm 0.06) \frac{r_h}{L} - i(2.67 \pm 0.22) \frac{r_h}{L}$
$\frac{r_h}{L}=4.0$	$(3.21 \pm 0.001) \frac{r_h}{L} - i(2.67 \pm 0.23) \frac{r_h}{L}$
$\frac{r_h}{L}=3.3$	$(3.33 \pm 0.08) \frac{r_h}{L} - i(2.71 \pm 0.20) \frac{r_h}{L}$
fund.	k=2
$\frac{r_h}{L}=12.2$	$(3.96 \pm 0.03) \frac{r_h}{L} - i(2.33 \pm 0.07) \frac{r_h}{L}$
$\frac{r_h}{L}=11.3$	$(3.94 \pm 0.02) \frac{r_h}{L} - i(2.30 \pm 0.08) \frac{r_h}{L}$
$\frac{r_h}{L}=10.5$	$(3.95 \pm 0.01) \frac{r_h}{L} - i(2.29 \pm 0.08) \frac{r_h}{L}$
$\frac{r_h}{L}=9.0$	$(3.95 \pm 0.002) \frac{r_h}{L} - i(2.26 \pm 0.09) \frac{r_h}{L}$
$\frac{r_h}{L}=6.5$	$(3.96 \pm 0.05) \frac{r_h}{L} - i(2.23 \pm 0.07) \frac{r_h}{L}$
$\frac{r_h}{L}=5.0$	$(3.94 \pm 0.05) \frac{r_h}{L} - i(2.21 \pm 0.04) \frac{r_h}{L}$
$\frac{r_h}{L}=4.5$	$(4.00 \pm 0.06) \frac{r_h}{L} - i(2.24 \pm 0.04) \frac{r_h}{L}$
$\frac{r_h}{L}=4.0$	$(3.99 \pm 0.06) \frac{r_h}{L} - i(2.24 \pm 0.03) \frac{r_h}{L}$
$\frac{r_h}{L}=3.3$	$(4.05 \pm 0.08) \frac{r_h}{L} - i(2.27 \pm 0.03) \frac{r_h}{L}$
fund.	k=4
$\frac{r_h}{L}=12.2$	$(4.93 \pm 0.007) \frac{r_h}{L} - i(1.83 \pm 0.05) \frac{r_h}{L}$
$\frac{r_h}{L}=11.3$	$(4.90 \pm 0.003) \frac{r_h}{L} - i(1.80 \pm 0.04) \frac{r_h}{L}$
$\frac{r_h}{L}=10.5$	$(4.92 \pm 0.002) \frac{r_h}{L} - i(1.78 \pm 0.04) \frac{r_h}{L}$
$\frac{r_h}{L}=9.0$	$(4.90 \pm 0.02) \frac{r_h}{L} - i(1.72 \pm 0.02) \frac{r_h}{L}$
$\frac{r_h}{L}=6.5$	$(4.80 \pm 0.01) \frac{r_h}{L} - i(1.65 \pm 0.003) \frac{r_h}{L}$
$\frac{r_h}{L}=5.0$	$(4.79 \pm 0.08) \frac{r_h}{L} - i(1.60 \pm 0.02) \frac{r_h}{L}$
$\frac{r_h}{L}=4.5$	$(4.87 \pm 0.11) \frac{r_h}{L} - i(1.69 \pm 0.04) \frac{r_h}{L}$
$\frac{r_h}{L}=4.0$	$(4.83 \pm 0.12) \frac{r_h}{L} - i(1.76 \pm 0.04) \frac{r_h}{L}$
$\frac{r_h}{L}=3.3$	$(4.9 \pm 0.1) \frac{r_h}{L} - i(1.89 \pm 0.05) \frac{r_h}{L}$

Table 4.4: The fundamental ($n = 0$) quasi-normal mode frequencies $\omega_r - i\omega_i$ extracted from the scalar field variable $\bar{\phi}$, from evolution of initial data as described in the first paragraph of Sec. 4.3. These are shown for various horizon radii r_h of the final state AdS-Schwarzschild black hole with $SO(4)$ quantum numbers $k \geq 0, l = 0, m = 0$. Uncertainties are estimated from convergence studies.

1 st overt.	k=0
$\frac{r_h}{L}=12.2$	$(5.66 \pm 0.24) \frac{r_h}{L} - i(2.90 \pm 0.28) \frac{r_h}{L}$
$\frac{r_h}{L}=11.3$	$(5.65 \pm 0.27) \frac{r_h}{L} - i(2.91 \pm 0.30) \frac{r_h}{L}$
$\frac{r_h}{L}=10.5$	$(5.69 \pm 0.30) \frac{r_h}{L} - i(2.94 \pm 0.32) \frac{r_h}{L}$
$\frac{r_h}{L}=9.0$	$(5.76 \pm 0.38) \frac{r_h}{L} - i(3.00 \pm 0.36) \frac{r_h}{L}$
$\frac{r_h}{L}=6.5$	$(5.98 \pm 0.62) \frac{r_h}{L} - i(3.19 \pm 0.42) \frac{r_h}{L}$
$\frac{r_h}{L}=5.0$	$(6.20 \pm 0.96) \frac{r_h}{L} - i(3.54 \pm 0.51) \frac{r_h}{L}$
$\frac{r_h}{L}=4.5$	$(6.41 \pm 1.13) \frac{r_h}{L} - i(3.82 \pm 0.57) \frac{r_h}{L}$
$\frac{r_h}{L}=4.0$	$(6.58 \pm 1.36) \frac{r_h}{L} - i(4.24 \pm 0.68) \frac{r_h}{L}$
$\frac{r_h}{L}=3.3$	$(7.02 \pm 1.78) \frac{r_h}{L} - i(5.34 \pm 1.04) \frac{r_h}{L}$
1 st overt.	k=2
$\frac{r_h}{L}=12.2$	$(6.36 \pm 0.26) \frac{r_h}{L} - i(3.28 \pm 0.15) \frac{r_h}{L}$
$\frac{r_h}{L}=11.3$	$(6.36 \pm 0.31) \frac{r_h}{L} - i(3.32 \pm 0.16) \frac{r_h}{L}$
$\frac{r_h}{L}=10.5$	$(6.41 \pm 0.35) \frac{r_h}{L} - i(3.37 \pm 0.14) \frac{r_h}{L}$
$\frac{r_h}{L}=9.0$	$(6.50 \pm 0.45) \frac{r_h}{L} - i(3.52 \pm 0.16) \frac{r_h}{L}$
$\frac{r_h}{L}=6.5$	$(6.78 \pm 0.71) \frac{r_h}{L} - i(4.02 \pm 0.08) \frac{r_h}{L}$
$\frac{r_h}{L}=5.0$	$(7.15 \pm 1.02) \frac{r_h}{L} - i(4.96 \pm 0.17) \frac{r_h}{L}$
$\frac{r_h}{L}=4.5$	$(7.45 \pm 1.19) \frac{r_h}{L} - i(5.61 \pm 0.32) \frac{r_h}{L}$
$\frac{r_h}{L}=4.0$	$(7.71 \pm 1.44) \frac{r_h}{L} - i(6.67 \pm 0.76) \frac{r_h}{L}$
$\frac{r_h}{L}=3.3$	$(8.04 \pm 1.74) \frac{r_h}{L} - i(9.35 \pm 2.38) \frac{r_h}{L}$
1 st overt.	k=4
$\frac{r_h}{L}=12.2$	$(7.60 \pm 0.17) \frac{r_h}{L} - i(4.11 \pm 0.17) \frac{r_h}{L}$
$\frac{r_h}{L}=11.3$	$(7.59 \pm 0.23) \frac{r_h}{L} - i(4.31 \pm 0.14) \frac{r_h}{L}$
$\frac{r_h}{L}=10.5$	$(7.63 \pm 0.26) \frac{r_h}{L} - i(4.56 \pm 0.14) \frac{r_h}{L}$
$\frac{r_h}{L}=9.0$	$(7.74 \pm 0.39) \frac{r_h}{L} - i(5.22 \pm 0.10) \frac{r_h}{L}$
$\frac{r_h}{L}=6.5$	$(8.04 \pm 0.79) \frac{r_h}{L} - i(7.92 \pm 0.41) \frac{r_h}{L}$
$\frac{r_h}{L}=5.0$	$(7.40 \pm 1.43) \frac{r_h}{L} - i(8.69 \pm 1.87) \frac{r_h}{L}$
$\frac{r_h}{L}=4.5$	$(7.63 \pm 2.19) \frac{r_h}{L} - i(8.78 \pm 1.74) \frac{r_h}{L}$
$\frac{r_h}{L}=4.0$	$(7.77 \pm 1.82) \frac{r_h}{L} - i(9.94 \pm 3.02) \frac{r_h}{L}$
$\frac{r_h}{L}=3.3$	$(7.68 \pm 1.32) \frac{r_h}{L} - i(12.7 \pm 4.7) \frac{r_h}{L}$

Table 4.5: The first overtone ($n = 1$) quasi-normal mode frequencies $\omega_r - i\omega_i$ extracted from the scalar field variable $\bar{\phi}$, from evolution of initial data as described in the first paragraph of Sec. 4.3. These are shown for various horizon radii r_h of the final state AdS-Schwarzschild black hole and for harmonics with $SO(4)$ quantum numbers $k \geq 0, l = 0, m = 0$. Uncertainties are estimated from convergence studies.

4.4 Dual Boundary CFT

In the remainder of this chapter, we finish our discussion by studying the boundary behavior that corresponds to the representative numerical solutions we have analyzed thus far. Specifically, we will extract the stress tensor of the boundary CFT that is dual to an asymptotically AdS spacetime describing the quasi-normal ringdown of a deformed black hole with initial asymmetry $w_y/w_x = 4$ or $w_y/w_x = 32$, which settles down at late times to the AdS Schwarzschild solution with horizon radius $r_h = 5$.

4.4.1 Conserved and Traceless CFT Stress Tensor

First, for a consistency check of expressions (3.4), we test whether (to within truncation error) the stress tensor is traceless and whether it is conserved with respect to the Levi-Civita connection on the $\mathbb{R} \times S^3$ boundary. Results for the trace and two non-trivial components of the divergence are displayed in Fig. 4.11 and 4.12, respectively. These plots demonstrate that as resolution is increased, we are indeed converging to a CFT stress tensor that is conserved and traceless, i.e. to matter that obeys the hydrodynamic equations of motion, and whose equation of state is consistent with conformal invariance. Note that the early-time transient related to the initial gauge dynamics discussed in Sec. 4.1 is also visible in these plots, though as with the independent residual it also converges away in the sense that it occupies a smaller region of the spacetime domain with increased resolution.

In Figs. 4.13, 4.14, 4.15 and 4.16 we display representative components of the boundary CFT stress tensor on $\mathbb{R} \times S^3$ spacetime diagrams, specifically the energy density $\langle T_{tt} \rangle_{\text{CFT}}$ and S^2 component of the pressure $\langle T_{\theta\theta} \rangle_{\text{CFT}}$ for the $w_y/w_x = 4$ and $w_y/w_x = 32$ cases. At $t = 0$ the boundary state is clearly inhomogeneous, and in time evolves to a homogeneous state in a manner that mirrors the quasi-normal decay of the spacetime to a static black hole.

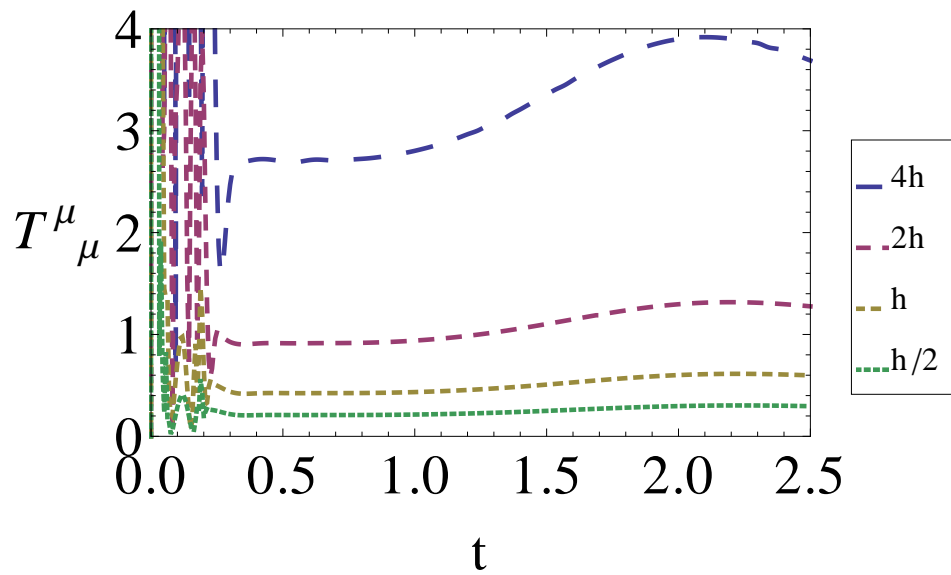


Figure 4.11: The trace $\langle T^\mu_\mu \rangle_{\text{CFT}}$ of the boundary stress tensor, constructed from a simulation run at 4 different resolutions, labeled by the mesh spacing relative to the highest resolution run h . Here the L^2 -norm of $\langle T^\mu_\mu \rangle_{\text{CFT}}$ is taken over the entire grid, and the trends indicate convergence to a trace-free stress tensor with increasing resolution.

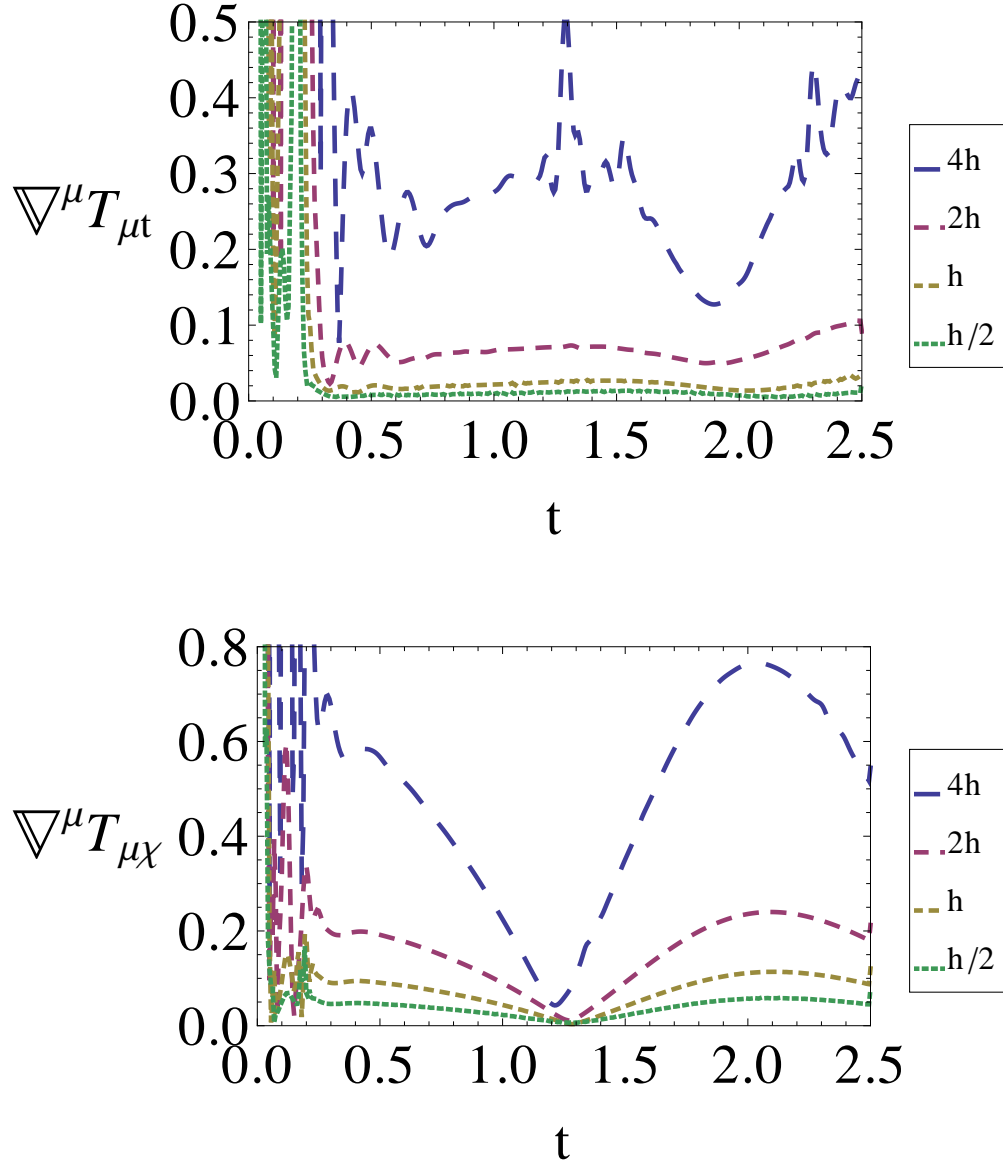


Figure 4.12: Two components of the divergence of the stress tensor, $\nabla^\mu \langle T_{\mu t} \rangle_{\text{CFT}}$ (top) and $\nabla^\mu \langle T_{\mu \chi} \rangle_{\text{CFT}}$ (bottom), constructed from a simulation run at 4 different resolutions, labeled by the mesh spacing relative to the highest resolution run $h/2$. The L^2 -norm of the respective components are taken over the entire grid, and the trends indicate convergence to a conserved stress tensor with increasing resolution.

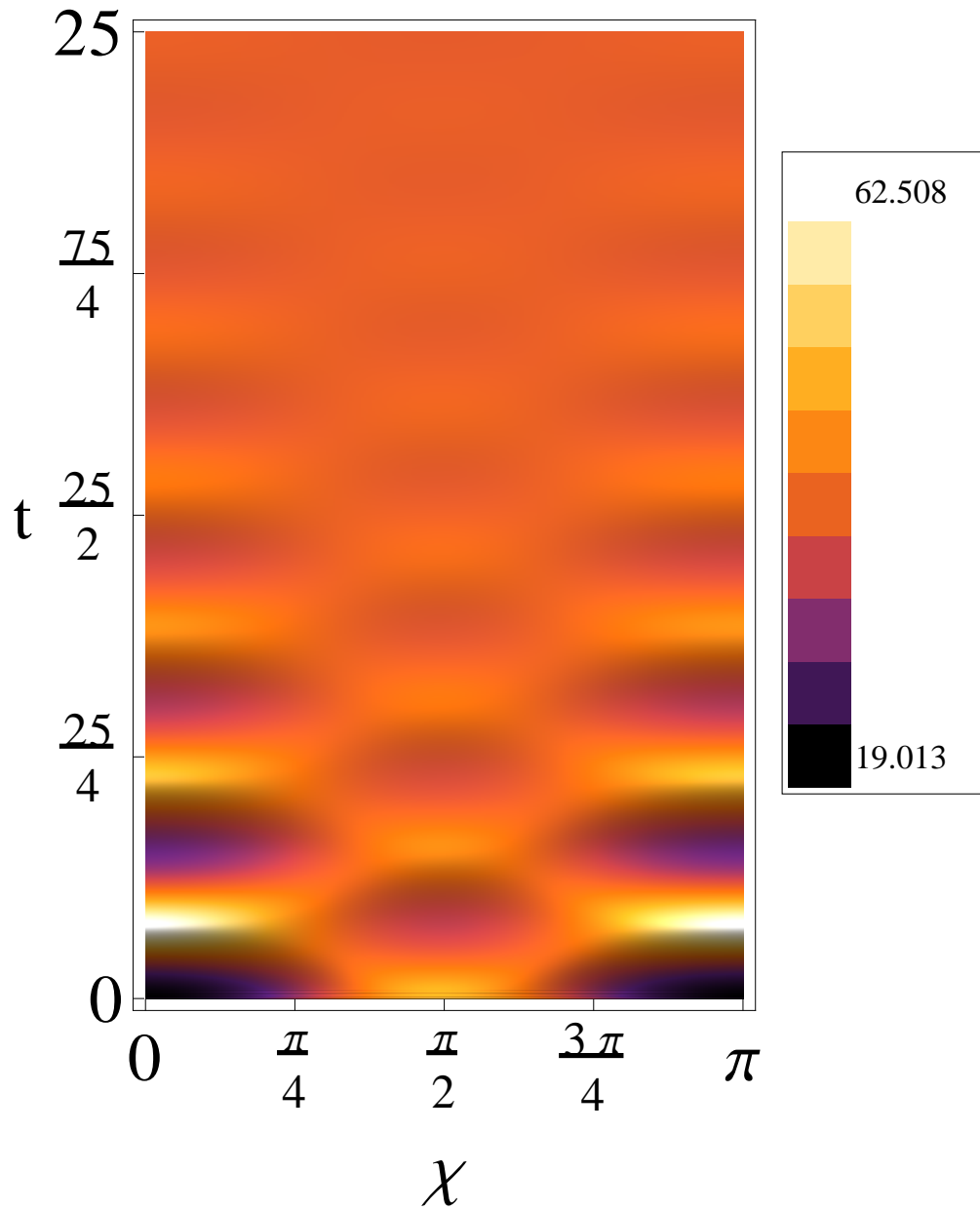


Figure 4.13: The energy density $\langle T_{tt} \rangle_{\text{CFT}}$ of the boundary CFT, displayed on a (t, χ) spacetime diagram, extracted from the $r_h = 5$ quasi-normal black hole ringdown simulation described in Sec. 4.3, with initial $w_y/w_x = 4$.

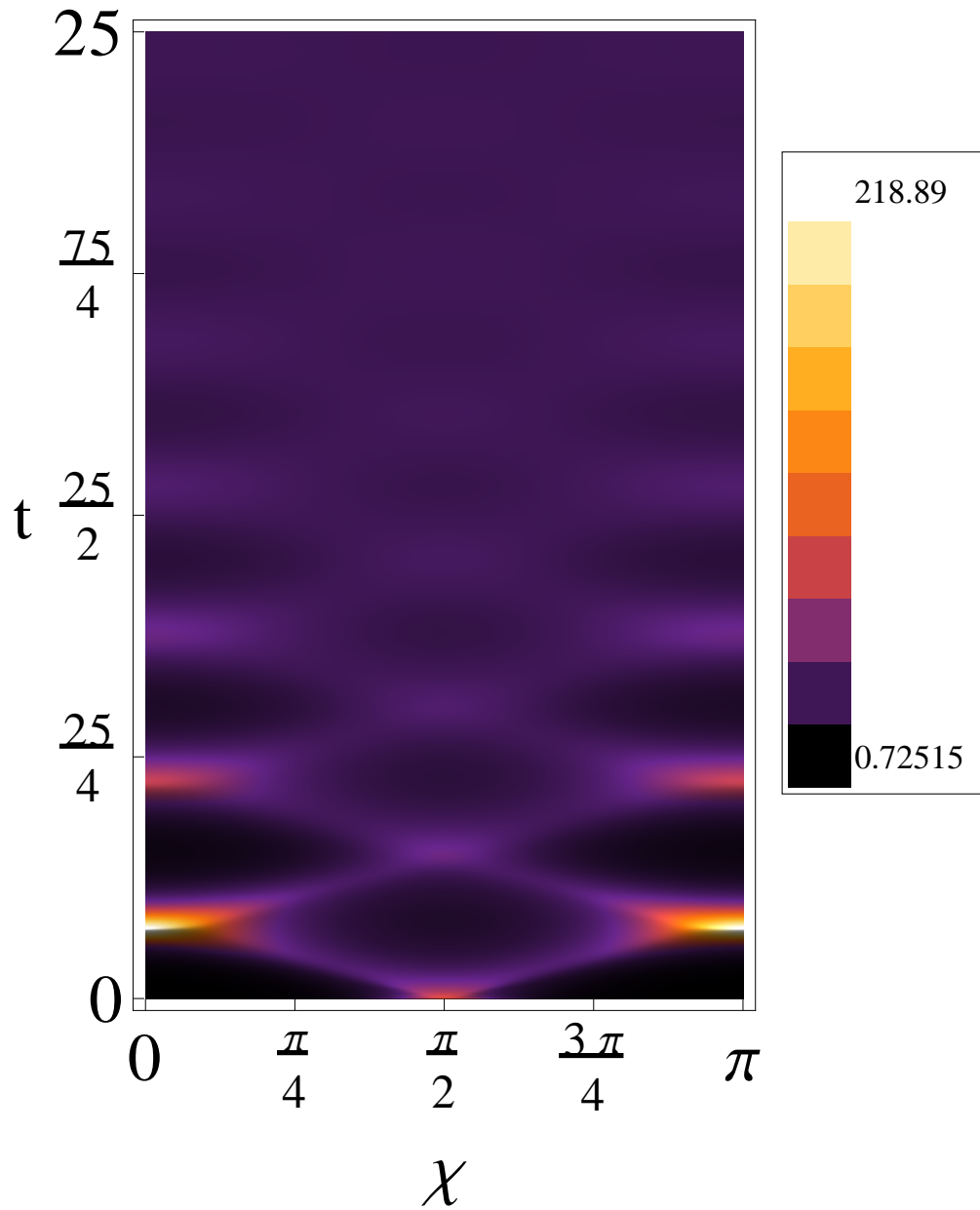


Figure 4.14: The energy density $\langle T_{tt} \rangle_{\text{CFT}}$ of the boundary CFT, displayed on a (t, χ) spacetime diagram, extracted from the $r_h = 5$ quasi-normal black hole ringdown simulation described in Sec. 4.3, with initial $w_y/w_x = 32$.

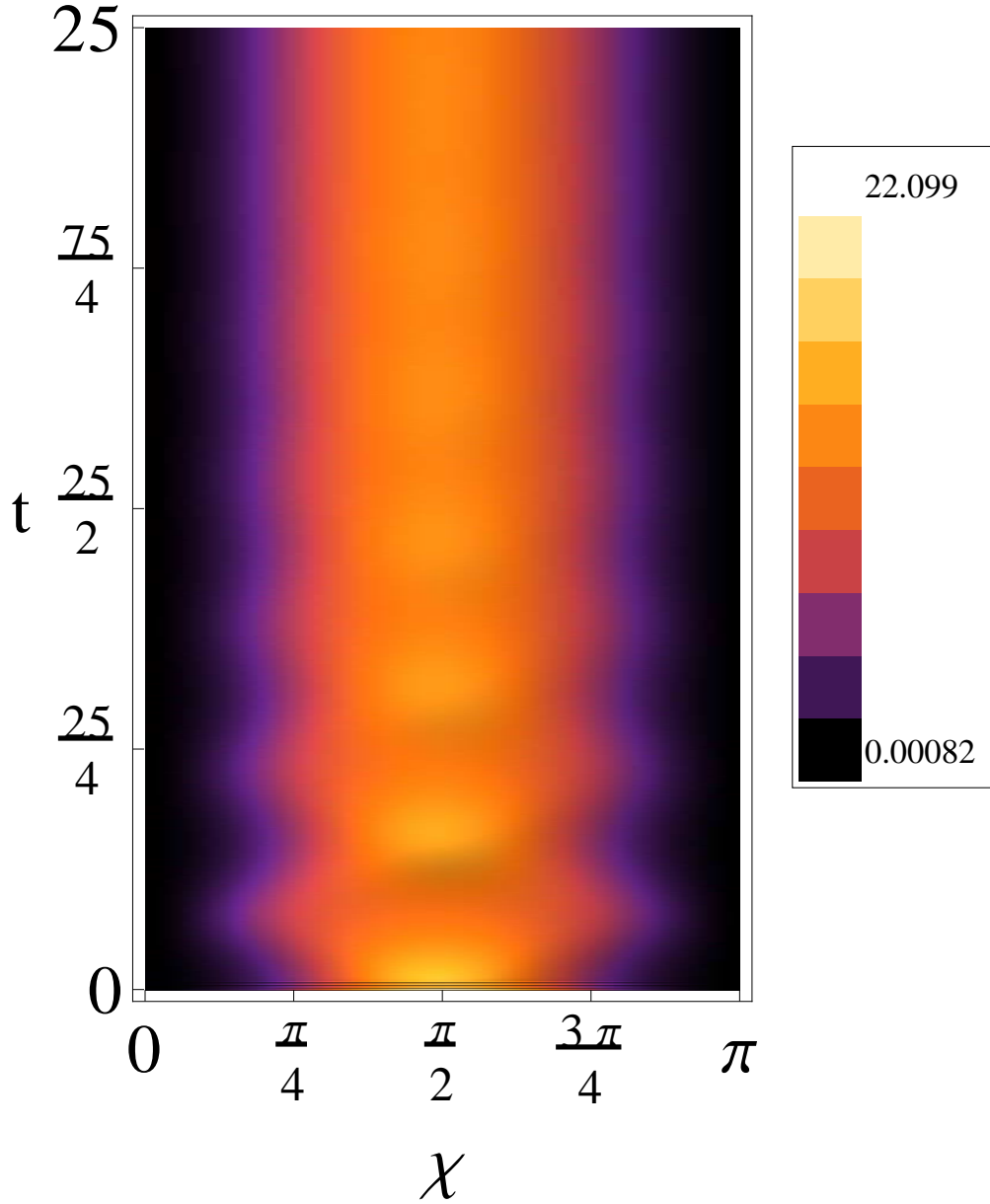


Figure 4.15: The S^2 component $\langle T_{\theta\theta} \rangle_{\text{CFT}}$ of the boundary CFT stress tensor, displayed on a (t, χ) spacetime diagram, extracted from the $r_h = 5$ quasi-normal black hole ringdown simulation described in Sec. 4.3, with initial $w_y/w_x = 4$.

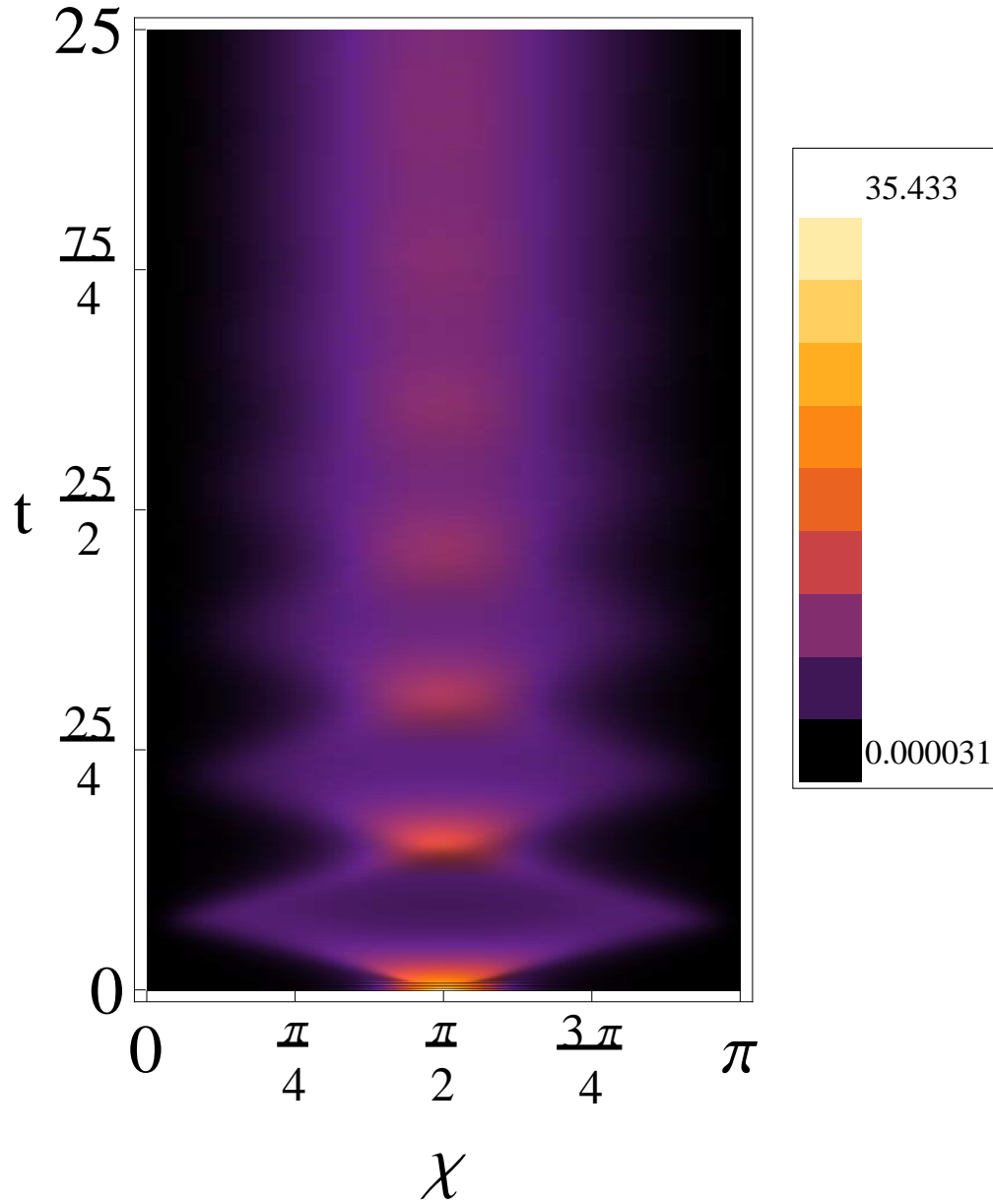


Figure 4.16: The S^2 component $\langle T_{\theta\theta} \rangle_{\text{CFT}}$ of the boundary CFT stress tensor, displayed on a (t, χ) spacetime diagram, extracted from the $r_h = 5$ quasi-normal black hole ringdown simulation described in Sec. 4.3, with initial $w_y/w_x = 32$.

4.4.2 Fluid Variables

In Sec. (4.4.1), we showed that convergence trends in the solution imply that in the continuum limit, $\langle T_{\mu\nu} \rangle_{\text{CFT}}$ is conserved and traceless. Thus, two necessary ingredients are already satisfied: conservation is required for the effective hydrodynamic variables to satisfy the Navier-Stokes equations, and for an isotropic fluid, tracelessness implies $\epsilon = 3P$. In this section we show that one *can* map $\langle T_{\mu\nu} \rangle_{\text{CFT}}$ to a corresponding set of hydrodynamic variables, and that essentially from the *initial time*, their behavior *is* consistent with that of an $\mathcal{N} = 4$ SYM fluid, at least to within truncation error.

Let us now map the boundary CFT stress tensor components $\langle T_{\mu\nu} \rangle_{\text{CFT}}$ to hydrodynamic variables as described in Sec. 3.2.1, using (3.11). By itself, the mapping (3.11) is not profound: the stress tensor with our symmetries has four independent components, and we have simply mapped them to a new set of four variables $(\epsilon, P, v, \eta\sigma)$. The crucial question though is whether these variables behave as those of a conformal fluid. The answer appears to be *yes*, even for these initially highly distorted black holes⁴.

To support this claim, we first note that in all cases we have looked at to date, we are able to perform the inversion (3.11) to obtain real-valued hydrodynamic variables that satisfy $\epsilon \geq 0$, $P \geq 0$ and $v \in (-1, 1)$. Fig. 4.17 shows an example of $v(t, \chi)$, from the $r_h = 5$ quasi-normal ringdown case discussed before. This suggests the stress tensor is consistent with that of *some* fluid. To check that it is a conformal fluid, in the top panel of Fig. 4.19 we show the quantity $(\epsilon - 3P)/\epsilon$ resulting from the evolution at several different resolutions, using the same initial data (to contrast with Fig. 4.11, here we are not merely testing that the stress tensor is traceless, but rather the more restrictive property that it arises from fluid flow where in the rest frame of the flow

⁴A few of the explicit examples shown here correspond to a “moderately” distorted initial black hole, with $r_h = 5$ and $c_{eq}/c_p(t=0) \approx 1.2$ —see Fig. 4.5, though the same conclusions hold for the most distorted cases we have looked at to date ($c_{eq}/c_p(t=0) \approx 2.2$), where the fluid velocity reaches a maximum $|v| \approx 0.54$ —see Fig. 4.17.

the pressure is isotropic). At any given resolution, this quantity is certainly nonzero due to truncation error; however, except for a transient at the initial time, the trends show that it is *converging to zero*, at or better than first order⁵. In other words, this says that after the initial transient, the boundary stress tensor behaves like a fluid with equation of state $\epsilon = 3P$ *to within numerical truncation error*. Fig. 4.20 is a close-up of the early transient behavior seen in Fig. 4.19, and as before for the convergence of the solution discussed in Sec. 4.1, it appears to be converging away in the sense that it affects a smaller region in time as resolution increases.

An alternative way to present this information is displayed in the bottom panels of Fig.’s 4.19 and 4.20. Here, assuming first order convergence of the extracted quantities, we take the finest resolution result as the continuum solution with an uncertainty (from truncation error) given by the magnitude of the difference between the finest and next-to-finest resolution results; this error is shown as the shaded region about the finest resolution curve. For subsequent time-series plots we will display the data in this format.

From this data we might also try to extract the lowest-order transport coefficient, namely the shear viscosity η , but here we encounter the two primary limitations of this sub-section’s extraction method. First, this method only allows us to extract the product $\eta\sigma$, so in order to find η we must divide by an independent calculation of σ . Such a calculation may be achieved by substituting the extracted velocity field into (3.6), which yields $\sigma|_v$, so we can compute $\eta\sigma/\sigma|_v \approx \eta$. Given our time-symmetric initial data, this $\sigma|_v$ has zeros at $t = 0$, and periodically after that. Even though the “true” $\eta\sigma$ necessarily has zeros at exactly the same times, the extracted $\eta\sigma$ will not, because we have ignored the $\Pi_{\mu\nu}$ higher-order contributions in the map. Thus, such a calculation of $\eta\sigma/\sigma|_v \approx \eta$ has the unattractive feature of diverging

⁵That the rate of convergence is closer to first order is due to how we extrapolate the solution to the boundary to extract the stress tensor components—the underlying solution for the metric still shows second-order convergence as discussed in Sec. 4.1.

whenever $\sigma|_v = 0$. Secondly, and more crucially, this method does not readily extend to allow the extraction of the higher-order transport coefficients. To remedy these shortcomings, we will now make use of the method described in Sec. 3.2.2 to analyze the hydrodynamic behavior of $\langle T_{\mu\nu} \rangle_{\text{CFT}}$.

4.4.3 Transport Coefficients

We are now in the position to ask whether the boundary flow is consistent with an $\mathcal{N} = 4$ SYM fluid, and if so, the extent to which higher-order corrections are important in describing it. We address these questions by comparing each of the reconstructed stress tensors $\sum_{i=0}^{i_{max}} T_{\mu\nu}^{(i)}$ for $i_{max} = 0, 1, 2$ to the full boundary CFT stress tensor of the numerical solution, as described in Sec. 3.2.2. The results of this comparison are summarized in Figs. 4.23 and 4.24 for a representative stress tensor component (normalized by the energy density ϵ). The plots in Fig. 4.23 are from the $w_y/w_x = 4$ solution, where the maximum velocity in the flow reaches ≈ 0.12 (see Fig. 4.17), and Fig. 4.24 is from the most asymmetric initial data case $w_y/w_x = 32$ that exhibits a maximum velocity of ≈ 0.54 . For the former case, the solution converges to behavior that is different from ideal hydrodynamics by at most $\approx 0.5\%$ (modulo the transient near $t = 0$); the inclusion of first-order and second-order corrections successively decrease this difference to a level which is essentially zero to within truncation error. The analogous plots for the larger asymmetry case in Fig. 4.24 show deviations from ideal hydrodynamics of up to 2.5% ; adding first order corrections reduces the maximum deviation to $\approx 1.5\%$, and second-order corrections to just under $\approx 1\%$. This is a rather remarkable level of consistency, in particular considering the trends in Fig. 4.24 as successively higher order viscous corrections are added.

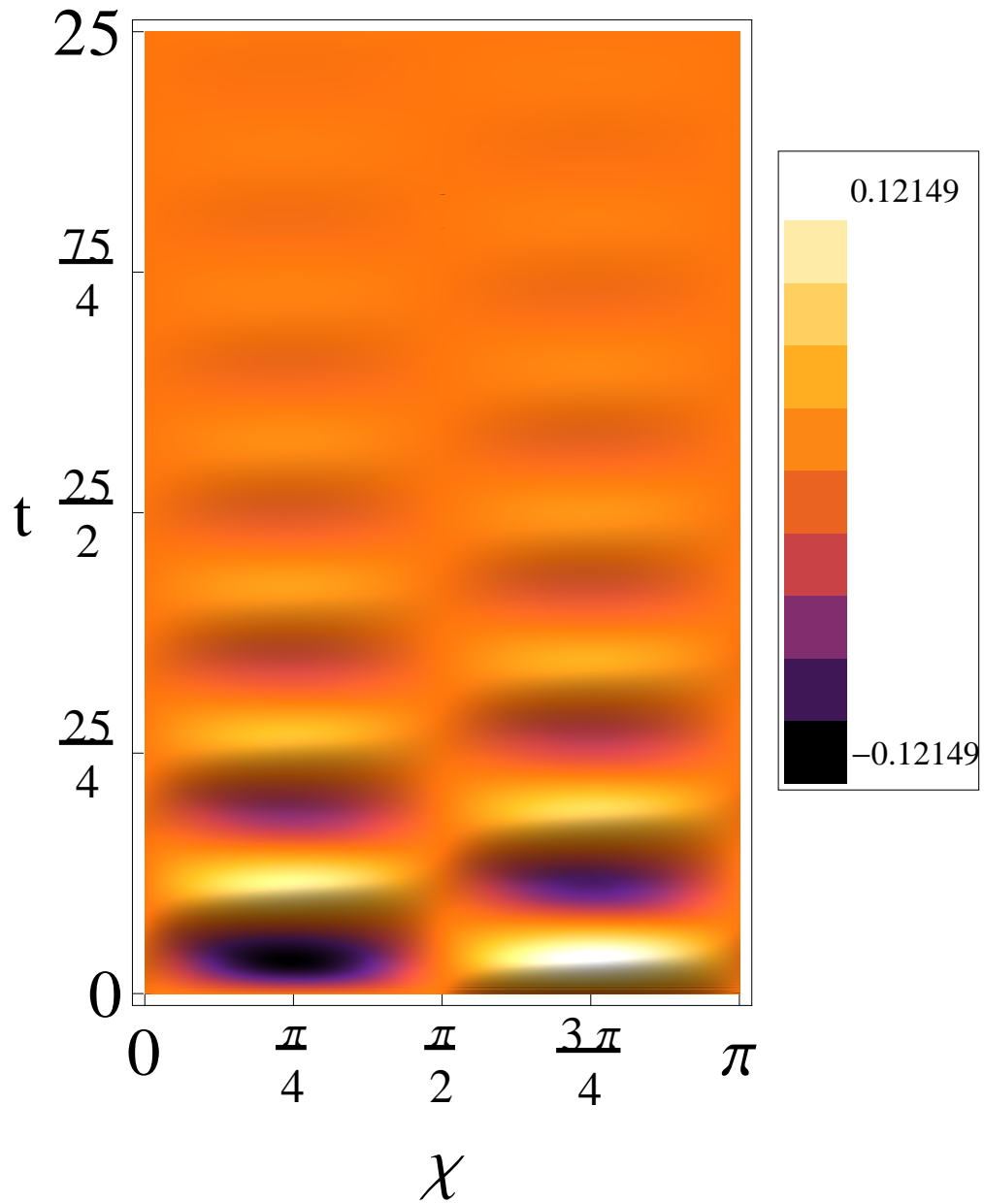


Figure 4.17: The velocity field v of the fluid describing the boundary CFT, displayed on a t, χ spacetime diagram, extracted from the $r_h = 5$ quasi-normal black hole ringdown simulation described in Sec. 4.3, with initial $w_y/w_x = 4$.

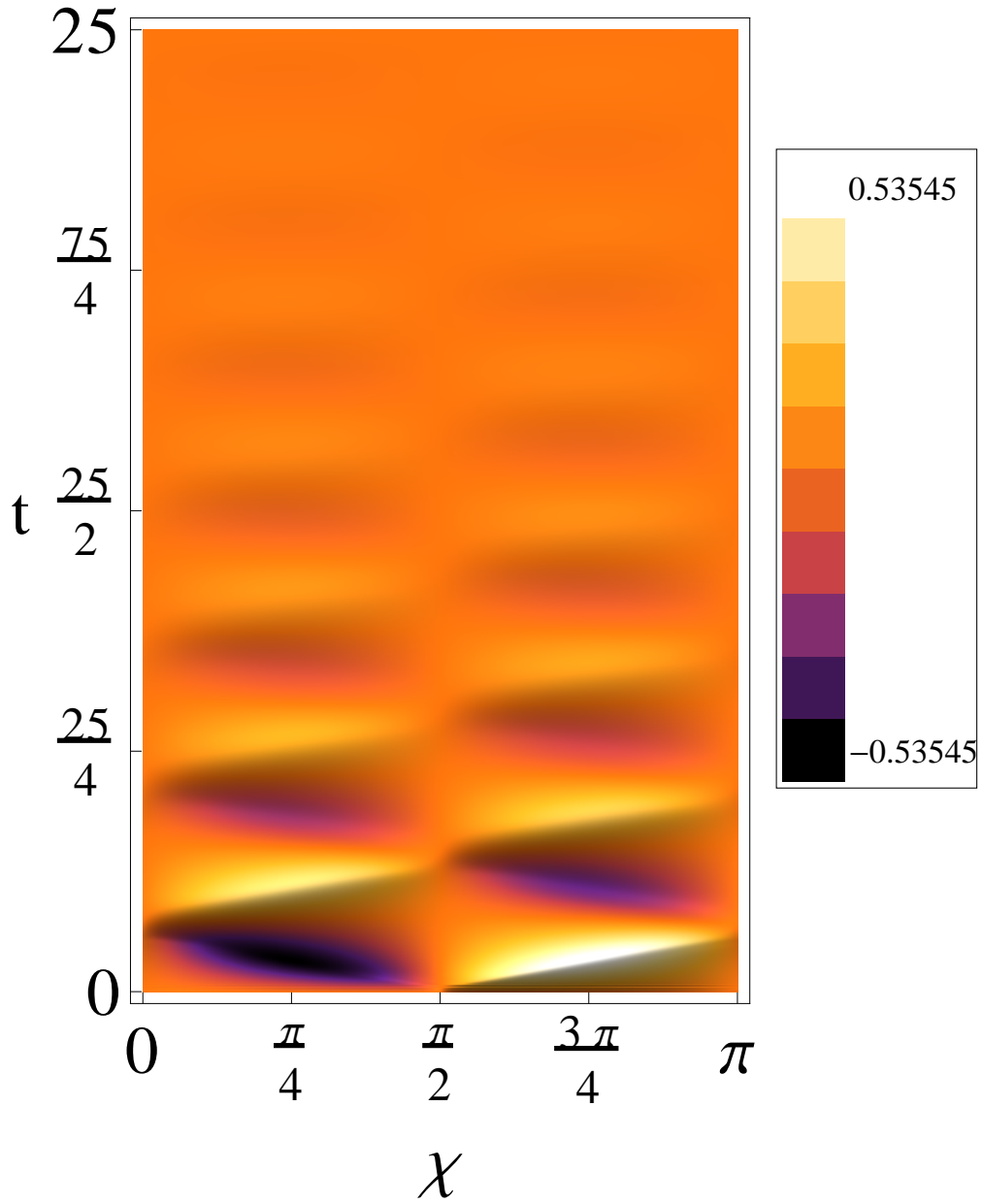


Figure 4.18: The velocity field v of the fluid describing the boundary CFT, displayed on a t, χ spacetime diagram, extracted from the $r_h = 5$ quasi-normal black hole ringdown simulation described in Sec. 4.3, with initial $w_y/w_x = 32$.

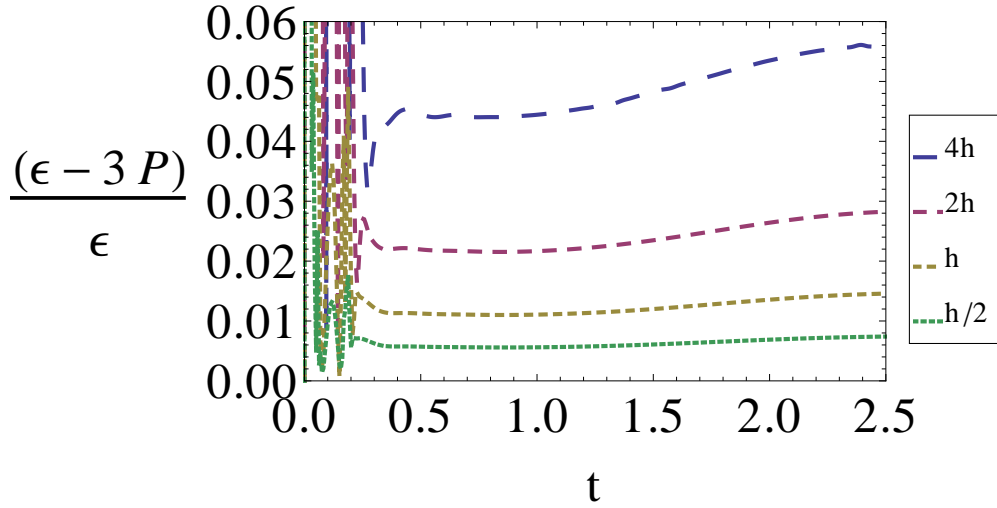


Figure 4.19: The quantity $(\epsilon - 3P)/\epsilon$, which measures the extent to which the hydrodynamic description is that of a fluid with equation of state $\epsilon = 3P$, constructed from simulations run at 4 different resolutions, labeled by the mesh spacing relative to the highest resolution run $h/2$. What is shown at each time is the L^2 -norm of $(\epsilon - 3P)/\epsilon$ taken over the entire grid. Except possibly for an early transient (see Fig. 4.20), that this quantity is converging to zero shows that $\epsilon = 3P$ to within truncation error.

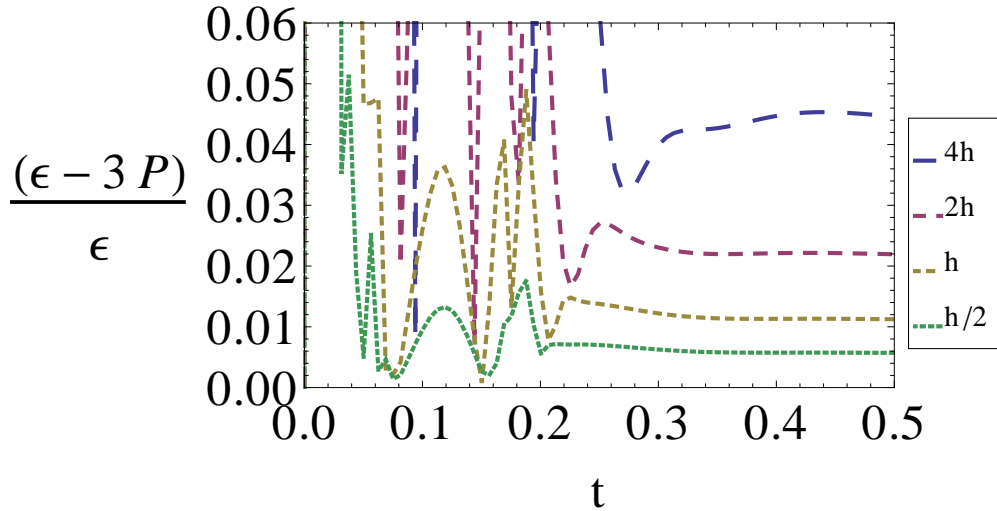


Figure 4.20: An expanded view of Fig. 4.19 at early times.

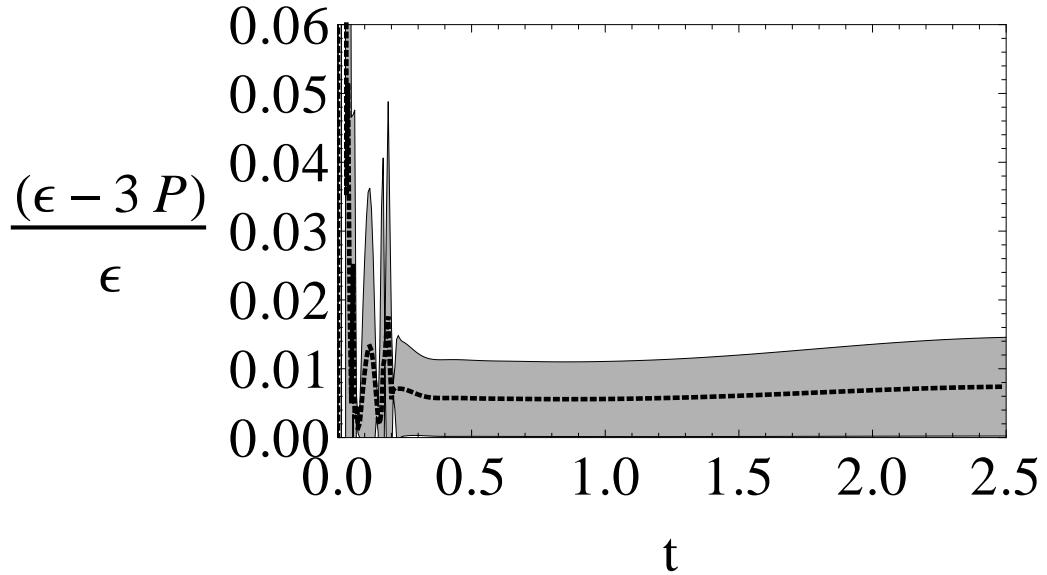


Figure 4.21: The quantity $(\epsilon - 3P)/\epsilon$, where the finest resolution data in Fig. 4.19 is interpreted as the continuum solution to within an uncertainty (shaded region). This uncertainty is obtained from the magnitude of the difference between the highest and next to highest resolution data in Fig. 4.19 (this assumes first order convergence of the extracted quantities).

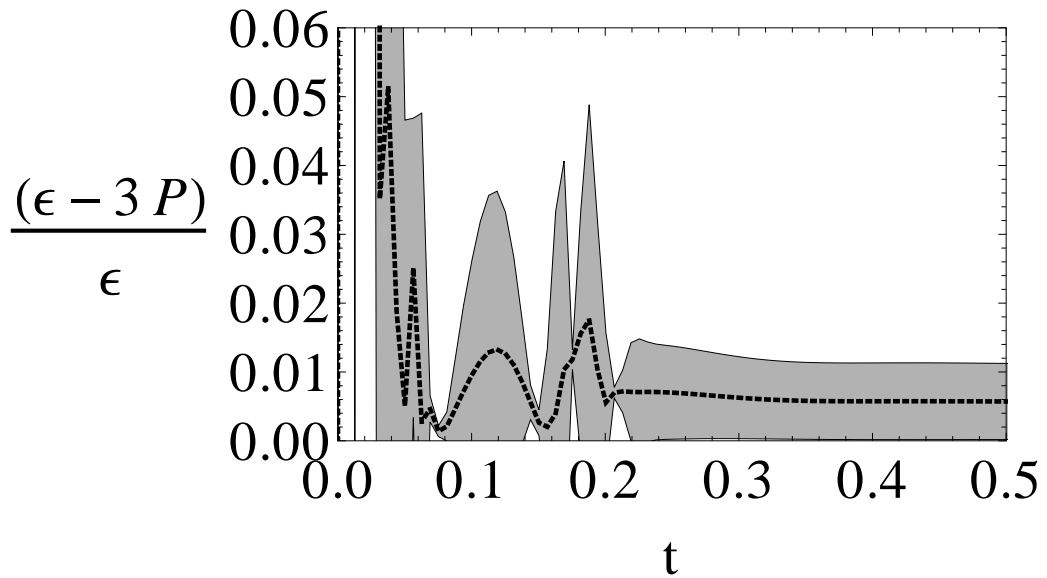


Figure 4.22: An expanded view of Fig. 4.21 at early times.

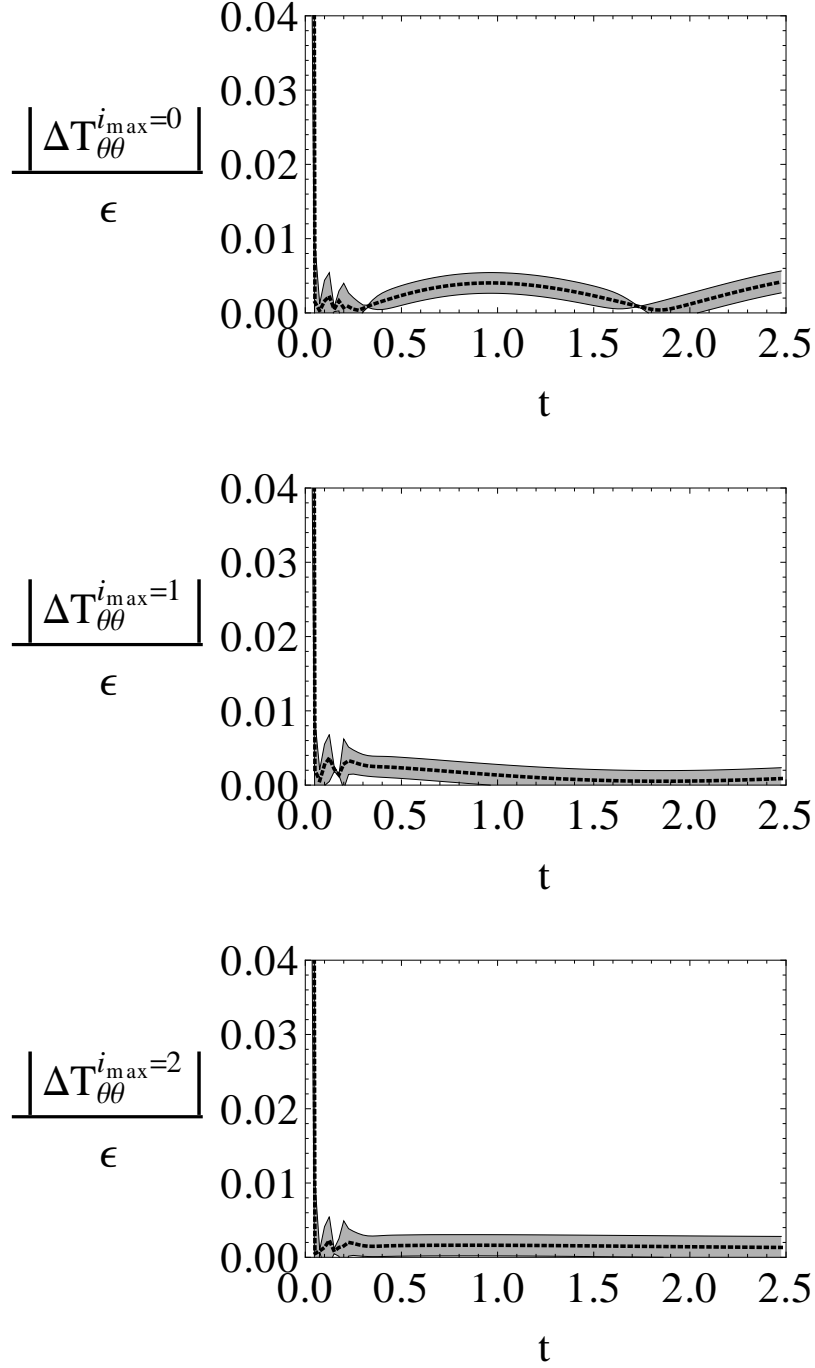


Figure 4.23: The normalized mismatch between $\langle T_{\mu\nu} \rangle_{\text{CFT}}$ and the reconstructed hydrodynamic $\sum_{i=0}^{i_{\text{max}}} T_{\mu\nu}^{(i)}$ with viscous corrections up to order $i_{\text{max}} = 0, 1, 2$, for a simulation with initial $w_y/w_x = 4$, and final $r_h = 5$. Here, $\Delta T_{\mu\nu}^{i_{\text{max}}} \equiv \langle T_{\mu\nu} \rangle_{\text{CFT}} - \sum_{i=0}^{i_{\text{max}}} T_{\mu\nu}^{(i)}$. In each panel, the highest resolution data (dashed line) is displayed with an estimated uncertainty (shaded region). Ideal hydrodynamics (top) shows a small mismatch; this is reduced after including 1st order viscous corrections (middle), and is zero to within truncation error when 2nd order viscous corrections are added (bottom).

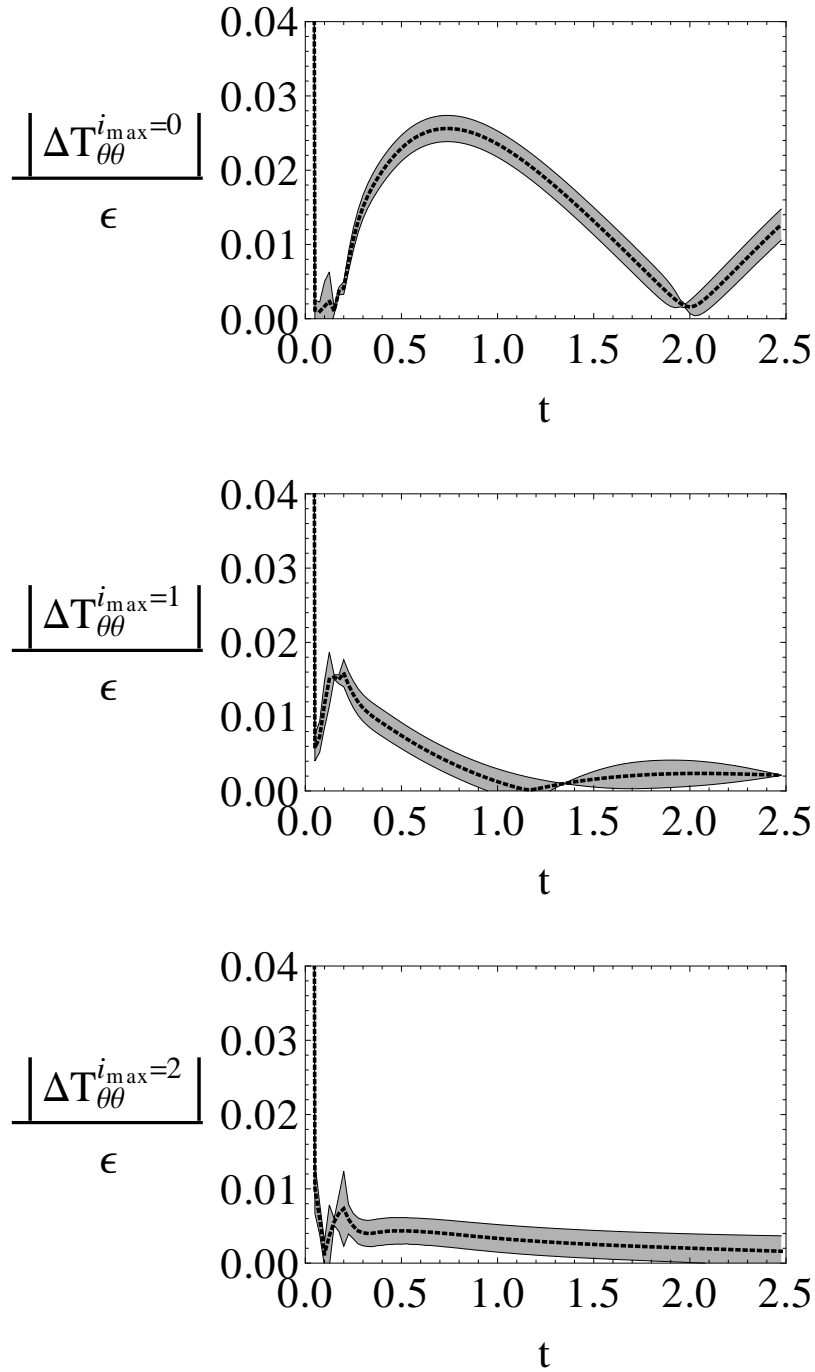


Figure 4.24: The same set of plots as described in Fig. 4.23, though here from the simulation of the $w_y/w_x = 32$ initial data. Notice the larger relative mismatches at a given order of the expansion compared to the $w_y/w_x = 4$ case in Fig. 4.23, and that there is still a small residual even after including all corrections through second order. The trend going from ideal (top) to second order viscous hydrodynamics (bottom) suggests that third and higher order corrections could further reduce the mismatch.

4.4.4 CFT on a Minkowski Piece of the Boundary

Thus far, in the field theory dual of deformed black holes, we have focused on fluid flows on the boundary of global AdS₅, namely $\mathbb{R} \times S^3$. As is clear from section 4.4.1, and in particular from Fig. 4.14, the fluid flow is essentially a compressive wave which starts with its peak at the equator of S^3 and then travels to the poles and back, oscillating and damping out toward a static configuration where the temperature on S^3 is everywhere constant. In this section, we would like to make closer contact with real-world fluid flows by conformally mapping our extracted boundary solution on $\mathbb{R} \times S^3$ onto a corresponding flow in Minkowski space.

The conformal mapping described in Sec. 3.3 can be used to compute the temperature (3.24) in Minkowski space. We do this using data from the same simulation that generated Fig. 4.14; this simulation is characterized by an initial asymmetry of $w_y/w_x = 32$. Each panel in Fig. 4.25 is taken from a $t' = \text{const}$ slice. The temperature is displayed as an $x_\perp - x_3$ profile, where we define x_\perp as

$$x_\perp = \sqrt{x_1^2 + x_2^2}, \quad (4.12)$$

and x_1 , x_2 , and x_3 are as defined in (3.16). Since the transformation to Minkowski space preserves the original ϕ -symmetry in global AdS, one can recover the full spatial dependence by simply rotating each of these $x_\perp - x_3$ profiles about the x_3 axis.

We are justified in defining the temperature (3.25) starting at Minkowski time $t' = 0$ because, by construction, our initial data perfectly conforms to the inviscid hydrodynamic ansatz. Moreover, again by construction, the velocity field vanishes exactly on the initial timeslice. Thus we are describing a version of the Landau-Khalatnikov full-stopping scenario [69, 70], but with radial flow explicitly included. The results of section 4.4.3, in particular Figs. 4.23 and 4.24, show that hydrodynamics

remains approximately valid throughout the evolution, with modest contributions from shear viscosity and small contributions from second-order transport coefficients.

To quantify the initial anisotropy in the temperature profile, we employ two slightly different quantities. The first is $\langle(x_{\perp})^2/\langle(x_3)^2\rangle$, where $\langle A(x_{\perp}, x_3)\rangle = \int dx_{\perp} dx_3 T(x_{\perp}, x_3)^4 A(x_{\perp}, x_3) / \int dx_{\perp} dx_3 T(x_{\perp}, x_3)^4$ is the energy-weighted average of some function $A(x_{\perp}, x_3)$ defined on the initial $t' = 0$ slice and at $\phi = 0$. This quantity evaluates to $\langle(x_{\perp})^2/\langle(x_3)^2\rangle = 6.94$ with the data displayed in Fig. 4.25. Alternatively, we can also obtain the widths δ_{\perp} and δ_3 such that $T^4(\delta_{\perp}, 0) = T^4(0, 0)/2$ and $T^4(0, \delta_3) = T^4(0, 0)/2$. From these, we construct the ratio $(\delta_{\perp})^2/(\delta_3)^2$; this evaluates to $(\delta_{\perp})^2/(\delta_3)^2 = 18.7$ with the data⁶.

⁶The extent to which $\langle(x_{\perp})^2/\langle(x_3)^2\rangle$ and $(\delta_{\perp})^2/(\delta_3)^2$ differ reflects the extent to which the temperature profile deviates from a perfect Gaussian. As a measure of anisotropy, the ratio of widths at half-max $(\delta_{\perp})^2/(\delta_3)^2$ is the more faithful of the two.

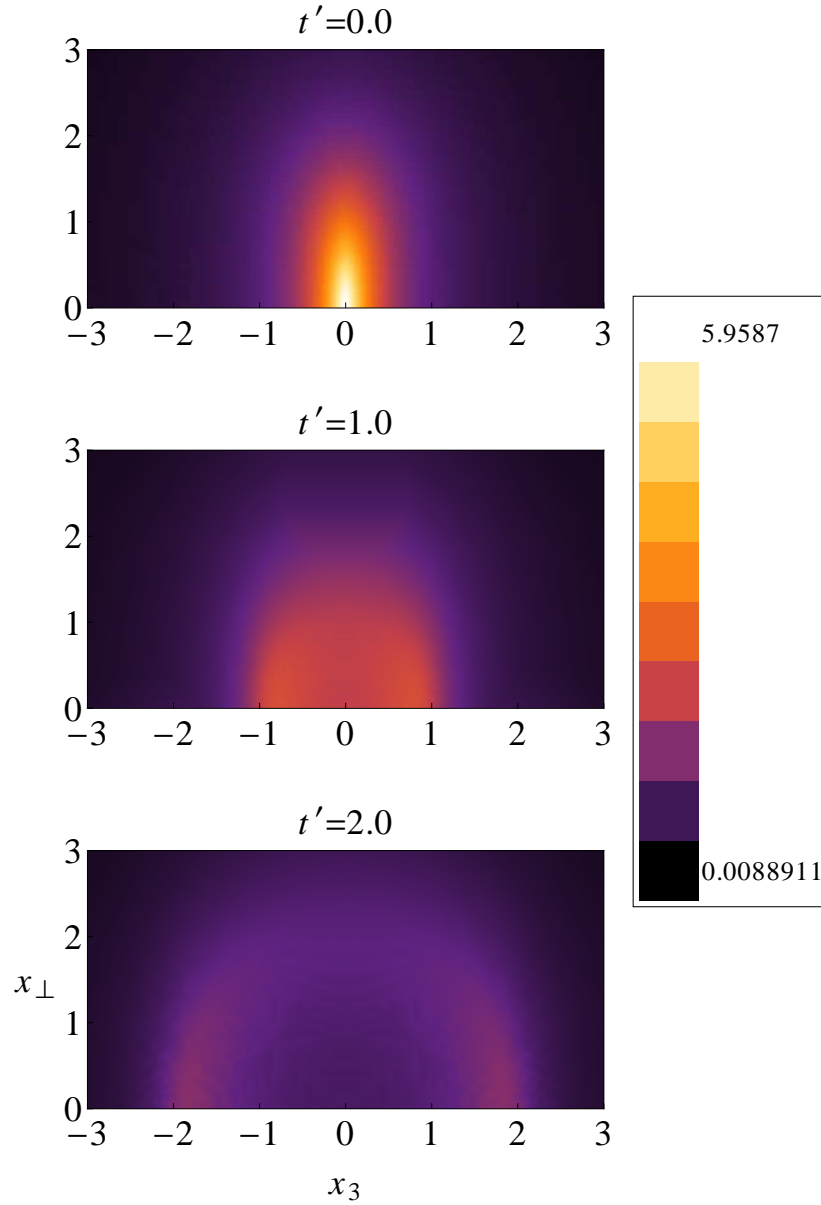


Figure 4.25: Temperature T defined in (3.25), for a simulation run with $w_y/w_x = 32$ initial data, whose final state black hole has horizon radius $r_h = 5$. Each plot depicts the spatial profile of temperature in the $x_\perp - x_3$ plane, taken at a constant t' slice and at $\phi = 0$. One can recover the full spatial dependence by simply rotating each of these $x_\perp - x_3$ profiles about the x_3 axis. By interpreting the x_3 axis as the longitudinal beam-line, and x_\perp as the transverse radius from the x_3 axis, the initial data in the top panel can be thought of as approximating a head-on heavy ion collision at its moment of impact. The subsequent panels shows that the resulting fluid flow exhibits both longitudinal and radial expansion.

Chapter 5

Conclusion

5.1 Discussion

We have described a generalized harmonic scheme for solving the Einstein field equations on asymptotically anti-de Sitter spacetimes in 4+1 dimensions. Though restricting to $SO(3)$ symmetry in the initial code, we expect that many of the methods developed here to achieve stable, consistent evolution will carry over to scenarios with less symmetry. This will be needed to tackle the main motivation for developing this code, namely to obtain the gravity dual to a heavy ion collision, and its subsequent quark-gluon plasma formation.

As a first application, we studied the quasi-normal ringdown of highly distorted black holes, and the corresponding behavior of the stress energy tensor of the dual CFT on the boundary of the spacetime. We find quasi-normal mode frequencies that are consistent with previously published linear modes, as well as modes that can be modeled as arising from non-linear mode-coupling. We further find purely decaying modes that we attribute to gauge. To be certain this is the case would require transforming the solution to coordinates fully compatible with perturbative

calculations, which is a rather non-trivial task numerically, and so we relegate this to a future study.

The boundary stress energy tensor exhibits correspondingly large initial fluctuations, yet we find that its behavior is consistent to better than 1% with that of an $\mathcal{N} = 4$ SYM fluid with equation of state $\epsilon = 3P$, and with corresponding transport coefficients, essentially from $t = 0$ onwards. This is in contrast to the numerical results reported in [23–26], where only after a certain time did the boundary behavior approach that of a fluid. However, those studies looked at scenarios more akin to black hole formation, i.e. beginning with states that do not contain large black holes (or black branes), with the black holes forming at later times. Such processes are expected to be dual to thermalization, whereas our study is that of equilibration beginning from an inhomogeneous though thermal state. Nevertheless, it is curious that the link between Einstein and Navier-Stokes seems to be holding even in these far-from-equilibrium scenarios, and it will be interesting in future work to explore how far this relationship extends. Recently it was shown that the Rayleigh-Plateau instability in a fluid stream and the Gregory-Laflamme instability of a black string are at least qualitatively similar [71]. These findings similarly suggest that, in some situations, the physics described by the Einstein and Navier-Stokes equations could exhibit similarities even in the most non-linear, near-singular regimes.

By passing to an appropriate Minkowski patch of the boundary of global AdS_5 , we are able to extract a fluid flow which starts from a compressed disk and leads to expansion both in the radial and longitudinal directions. The $SO(3)$ symmetry is still present, but as a conformal symmetry rather than an isometry of the flow. This flow exhibits the main qualitative features of the full-stopping scenario in heavy ion collisions, which, though generally considered implausible in light of asymptotic freedom, has some interesting phenomenological successes [72].

5.2 Future Work

A direction for future study that could be accomplished within the simplification of the current $SO(3)$ symmetry is to couple gravity to additional forms of matter. In the context of AdS/CFT, it is interesting to consider tachyonic scalar fields, since these amount to relevant operator insertions in the boundary CFT. As one might expect, the resulting deformation is dramatic: on the gravity side, these tachyonic scalars back-react in such a way as to significantly change the boundary conditions of the metric. The evolution of such systems in the full non-linear regime is unknown, though hopefully methods similar to those introduced here will be able to handle such spacetimes with “deformed” AAdS boundaries. These methods are also applicable to AAdS spacetimes with different boundary topology, which (with the appropriate matter content) are of interest to condensed matter applications of the duality.

The next natural step is to relax our current symmetries, to a gravitational model that admits a boundary description with variations in two spatial directions. This would allow us to model a heavy ion collision in its entirety, beginning at a time before the heavy ions collide. The geometry at the moment of impact could then be allowed to arise dynamically, so that the only tunable parameters in this model would be the type of gravitational objects that act as proxies for the heavy ions, and the speed at which they collide. This dissertation represents a necessary first step towards this type of gravitational model, and towards a more robust comparison between the dynamics of asymptotically AdS spacetimes and real-world quark-gluon plasma flows.

Appendix A

Boundary Conditions for Linearized Gravitational Perturbations of AdS

A theorem due to Fefferman and Graham [48] states that a distinguished coordinate system (z, x^i) exists on the Poincaré patch of any asymptotically AdS₅ spacetime M in which the metric takes the form

$$G = \frac{L^2}{z^2} (dz^2 + g_{ij} dx^i dx^j) \quad (\text{A.1})$$

and that there is a convergent power series solution for the g_{ij} coefficients in (A.1) given by

$$g_{ij} = g_{(0)ij} + g_{(2)ij} z^2 + g_{(4)ij} z^4 + 2h_{(4)ij} z^4 \log z + \mathcal{O}(z^6) \quad (\text{A.2})$$

(the boundary ∂M is located at $z = 0$).

Let us first translate this statement to global AdS₅ coordinates $(t, r, \chi, \theta, \phi)$. Since the Fefferman-Graham theorem, as originally stated, is adapted to the Poincaré patch of AdS, we will have to content ourselves with a partial translation i.e. one that is

only valid in a restricted region of global AdS. The relationship between the Poincaré coordinates (t', z) and the global coordinates (t, r) is given by

$$\frac{z}{L} = \frac{1}{\sqrt{1 + r^2/L^2} \cos t'/L + r/L \cos \chi}. \quad (\text{A.3})$$

Since we are mainly interested in radial dependence, we will restrict ourselves to slices of $t = 0, \chi = \pi/2$, in which case the leading-order relationship between z and r near the boundary at $z = 0$, or equivalently $r \rightarrow \infty$, is simply

$$\frac{z}{L} = \frac{L}{r} + \mathcal{O}(1/r^2). \quad (\text{A.4})$$

In terms of the global coordinate $q = 1/(1+r)$ introduced in Sec. 3.1, and setting $L = 1$ for convenience, to leading-order, we have $z = 1/r + \mathcal{O}(1/r^2) = q + \mathcal{O}(q^2)$ near the $q = 0$ boundary. So the Fefferman-Graham theorem's power series solution in these coordinates on a $t = 0, \chi = \pi/2$ slice reads just like (A.2)

$$g_{ij} = g_{(0)ij} + g_{(2)ij}q^2 + g_{(4)ij}q^4 + 2h_{(4)ij}q^4 \log q + \mathcal{O}(q^6) \quad (\text{A.5})$$

(the boundary ∂M is located at $q = 0$).

The $g_{(0)ij}$ corresponds to the non-radial components of the pure AdS₅ metric. The $g_{(2)ij}$ can be expressed, as was done explicitly in [73], in terms of the Ricci tensor $R_{(0)ij}$ and the scalar curvature $R_{(0)}$ constructed from $g_{(0)ij}$, and is thus fixed. The leading-order dynamics then first appears¹ in the terms controlled by $g_{(4)ij}$. Inspecting (A.5), this implies that the leading-order asymptotics is $g_{ij} \sim q^2$, in agreement with the boundary conditions we wrote down in Sec. 2.2.

We can now show how our metric boundary conditions (1.70) relate to those derived by Ishibashi and Wald in [34]. Working perturbatively, they derive conditions

¹In $D = d + 1$ dimensions, the leading-order dynamics appears in the $g_{(d)ij}$ term, since $g_{(n)ij}$ for $n < d$ are determined by $g_{(0)ij}$.

under which a metric perturbation must have its boundary behavior enforced by explicit boundary conditions. The fields governing the perturbations, which we collectively denote by f , are decomposed in terms of spherical harmonics $\mathbb{S}_k(\Omega^i)$ according to

$$f = \frac{1}{r^{3/2}} \sum_{k_S} \Phi_k(t, r) \mathbb{S}_k(\Omega^i). \quad (\text{A.6})$$

The Φ fields for the tensor and vectors modes of the gravitational perturbations are shown to require no boundary conditions at infinity (see Proposition 3.1 and its preceding discussion in [34]). However, the scalar modes of the gravitational perturbations require boundary conditions, and their corresponding Φ are shown to behave asymptotically as

$$\Phi = G_0(r) [2a_0 \log(1/r) + b_0 + 2L^2/r^2 \log(1/r) + \dots] \quad (\text{A.7})$$

where the function $G_0(r)$ is asymptotically given by

$$G_0(r) \sim \frac{1}{r^{1/2}}. \quad (\text{A.8})$$

In terms of the global coordinate q , the implication is that for the scalar modes of the gravitational perturbations the near-boundary behavior is

$$g_{ij} \sim 2a_0 q^2 \log(q) + b_0 q^2 + 2c_0 q^4 \log(q) + \dots \quad (\text{A.9})$$

For the scalar modes, imposing boundary conditions amounts to setting the ratio b_0/a_0 . Comparing (A.9) to (A.5), we see that the choice picked out by coordinates that are Fefferman-Graham-like near the boundary is $b_0/a_0 \rightarrow \infty$ i.e. $a_0 = 0$. This removes the logarithmic branch controlled by a_0 , so the leading-order asymptotics is $g_{ij} \sim q^2$.

Appendix B

Effect of Scalar Backreaction on Metric Fall-off

Here we compute the effect that a static spherical distribution of massless scalar would have on the AAdS₅ metric. The configuration only has radial dependence $\phi = \phi(r)$, so the metric must take the form

$$ds^2 = - (1 + r^2 + \mathcal{O}(r^{-1})) dt^2 + \frac{1}{\left(1 + r^2 - \frac{\mu(r)}{r}\right)} dr^2 + r^2 d\Omega_3^2 \quad (\text{B.1})$$

where $\mu(r)$ grows slower than r^3 as $r \rightarrow \infty$ in order to preserve the value of the cosmological constant. We have set $L = 1$, so that $\Lambda_5 = -6$. In a previous section, we had used the AdS₅ Klein-Gordon equation (1.72) in spherical symmetry to find the general leading order behavior (1.73) of scalar fields in AdS₅. We now find the metric fall-off behavior when scalar back-reaction is taken into account, limiting ourselves to the $h_{\rho\rho}$ component of the metric deviation and using the compactified coordinate $\rho = r/(1+r)$. In order to find this fall-off, the strategy is to solve for $\mu(r)$ as a power

series in r , from which we can reconstruct

$$h_{\rho\rho} = \left(\frac{\partial r}{\partial \rho}\right)^2 h_{rr} = \frac{\mu(r)}{r} \quad (\text{B.2})$$

where we have used $\partial r/\partial \rho = 1/(1-\rho)^2 \sim r^2$ along with $h_{rr} = g_{rr} - \hat{g}_{rr}$ and

$$g_{rr} = (1 + r^2 - \mu(r)/r)^{-1} = \frac{1}{r^2} \left[1 + \frac{\mu(r)}{r^3} + \mathcal{O}(r^{-5}) \right]. \quad (\text{B.3})$$

We can deduce the asymptotic behavior of $\mu(r)$ from the the Hamiltonian constraint¹

$${}^{(4)}R - 2\Lambda_5 = 16\pi\rho_E. \quad (\text{B.4})$$

where

$${}^{(4)}R = 2\Lambda_5 + \frac{2 + r^2(5 + 3r^2)}{(r + r^3)^2} \mu'(r) + \frac{r(5 + 3r^2)}{(r + r^3)^2} \mu(r) \quad (\text{B.5})$$

is the Ricci scalar associated with the 4-metric on the slice, and

$$\rho_E = \frac{1}{2}(1 + r^2 - \mu(r)/r)(\phi'(r))^2 + \frac{1}{2}m^2\phi^2 \quad (\text{B.6})$$

is the scalar field energy density. Keeping only the terms in (B.4) that dominate at large r , we obtain the form of the Hamiltonian constraint near the boundary

$$\frac{\mu'(r)}{r^2} + \frac{\mu(r)}{r}(\phi'(r))^2 \sim r^2(\phi'(r))^2 + m^2\phi^2. \quad (\text{B.7})$$

The scalar field goes as $\phi(r) \sim r^{-\Delta}$ near the boundary for some Δ , so we see that the right-hand-side of (B.7) goes as $r^{-2\Delta}$. Matching the left and right-hand sides, we conclude that

$$\mu(r) \sim r^{3-2\Delta} \quad (\text{B.8})$$

¹See Sec. 1.4.2.

and consequently,

$$h_{\rho\rho} \sim r^{2-2\Delta}. \quad (\text{B.9})$$

To make use of what we have learnt, first suppose that we have a scalar with negative $m^2 < 0$. From (1.73) and (1.74), a non-zero A branch describes the leading behavior for large r , and is defined by a fall-off power of $\Delta = \Delta_+ = 2 - \sqrt{4 + m^2}$. Then equation (B.9) predicts that matter backreaction induces a metric deviation $h_{\rho\rho} \sim r^{-2+2\sqrt{4+m^2}}$ that is larger than the vacuum metric fall-off we assumed in (2.10) and in (2.11). This case corresponds to a tachyonic scalar configuration. These configurations are stable in AdS as long as its mass satisfies the Breitenlohner-Freedman bound [74] given by $-(D-1)^2/(4L^2) = -4 < m^2$ in $D = 5$ dimensions: it is stable in the sense that its conserved energy functional remains positive in the function space of all fluctuations for which the energy functional remains a convergent integral. The qualitative reason for the positivity of this energy functional in AdS is that despite the negative unbounded potential of the tachyonic scalar, the positive kinetic terms in the energy functional dominate the negative potential terms so long as the scalar falls off sufficiently quickly near the boundary².

For this dissertation, we focus on scalars with $m^2 \geq 0$. Again looking at (1.73), (1.74), notice that we must now turn off the A branch in order to have a scalar field that vanishes at infinity, which is required for any scalar field configuration with finite energy. The result is a localized matter distribution defined by a fall-off power $\Delta = \Delta_+ = 2 + \sqrt{4 + m^2}$. Applying our result (B.9) to this case, we find that backreaction induces a metric deviation $h_{\rho\rho} \sim r^{-2-2\sqrt{4+m^2}}$ that is subleading compared to the vacuum metric fall-off (2.11), and thus leaving it unchanged.

²A scalar with the critical fall-off behavior goes as $\phi \sim r^{\Delta_c}$ for $\Delta_c = (D-1)/2 = 2$ in $D = 5$ dimensions; the BF bound can be inferred from this observation.

Appendix C

Finite Difference Stencils

$f_{,t}$	$(f_{i,j}^{n+1} - f_{i,j}^{n-1})/(2\Delta t)$
$f_{,\rho}$	$(f_{i+1,j}^n - f_{i-1,j}^n)/(2\Delta\rho)$
$f_{,\chi}$	$(f_{i,j+1}^n - f_{i,j-1}^n)/(2\Delta\chi)$
$f_{,tt}$	$(f_{i,j}^{n+1} - 2f_{i,j}^n + f_{i,j}^{n-1})/\Delta t^2$
$f_{,\rho\rho}$	$(f_{i+1,j}^n - 2f_{i,j}^n + f_{i-1,j}^n)/\Delta\rho^2$
$f_{,\chi\chi}$	$(f_{i,j+1}^n - 2f_{i,j}^n + f_{i,j-1}^n)/\Delta\chi^2$
$f_{,t\rho}$	$(f_{i+1,j}^{n+1} - f_{i-1,j}^{n+1} - f_{i+1,j}^{n-1} + f_{i-1,j}^{n-1})/(4\Delta t\Delta\rho)$
$f_{,t\chi}$	$(f_{i,j+1}^{n+1} - f_{i,j-1}^{n+1} - f_{i,j+1}^{n-1} + f_{i,j-1}^{n-1})/(4\Delta t\Delta\chi)$
$f_{,\rho\chi}$	$(f_{i+1,j+1}^n - f_{i+1,j-1}^n - f_{i-1,j+1}^n + f_{i-1,j-1}^n)/(4\Delta\rho\Delta\chi)$

Table C.1: A representative sample of the second order accurate finite difference stencils that are used to represent differential equations by difference equations.

Bibliography

- [1] J. M. Maldacena, *Adv.Theor.Math.Phys.* **2**, 231 (1998), [hep-th/9711200](#).
- [2] S. Gubser, I. R. Klebanov, and A. M. Polyakov, *Phys.Lett.* **B428**, 105 (1998), [hep-th/9802109](#).
- [3] E. Witten, *Adv.Theor.Math.Phys.* **2**, 253 (1998), [hep-th/9802150](#).
- [4] S. S. Gubser and A. Karch, *Ann. Rev. Nucl. Part. Sci.* **59**, 145 (2009), [hep-th/0901.0935](#).
- [5] C. P. Herzog, *J.Phys.A* **A42**, 343001 (2009), [hep-th/0904.1975](#).
- [6] S. A. Hartnoll, *Class.Quant.Grav.* **26**, 224002 (2009), [hep-th/0903.3246](#).
- [7] J. McGreevy, *Adv. High Energy Phys.* **2010**, 723105 (2010), [hep-th/0909.0518](#).
- [8] S. Sachdev (2010), [hep-th/1002.2947](#).
- [9] S. S. Gubser (2010), [hep-th/1012.5312](#).
- [10] G. T. Horowitz (2010), [hep-th/1002.1722](#).
- [11] S. S. Gubser (2011), [hep-th/1103.3636](#).
- [12] F. Pretorius (2007), [gr-qc/0710.1338](#).
- [13] M. D. Duez, *Class.Quant.Grav.* **27**, 114002 (2010), [astro-ph/0912.3529](#).
- [14] M. Campanelli, C. O. Lousto, B. C. Mundim, H. Nakano, Y. Zlochower, et al., *Class.Quant.Grav.* **27**, 084034 (2010), [gr-qc/1001.3834](#).
- [15] J. Centrella, J. G. Baker, B. J. Kelly, and J. R. van Meter, *Rev.Mod.Phys.* **82** (2010), [gr-qc/1010.5260](#).
- [16] F. Pretorius and M. W. Choptuik, *Phys.Rev.* **D62**, 124012 (2000), [gr-qc/0007008](#).
- [17] V. Husain and M. Olivier, *Class.Quant.Grav.* **18**, L1 (2001), [gr-qc/0008060](#).
- [18] D.-i. Hwang, H. Kim, and D.-h. Yeom (2011), [gr-qc/1105.1371](#).

- [19] P. Bizon and A. Rostworowski (2011), [gr-qc/1104.3702](#).
- [20] D. Garfinkle and L. A. Pando Zayas (2011), [hep-th/1106.2339](#).
- [21] V. Husain, G. Kunstatter, B. Preston, and M. Birukou, *Class. Quant. Grav.* **20**, L23 (2003), [gr-qc/0210011](#).
- [22] M. Birukou, V. Husain, G. Kunstatter, E. Vaz, and M. Olivier, *Phys.Rev.* **D65**, 104036 (2002).
- [23] P. M. Chesler and L. G. Yaffe, *Phys. Rev. Lett.* **106**, 021601 (2011), [hep-th/1011.3562](#).
- [24] B. Wu and P. Romatschke (2011), [hep-th/1108.3715](#).
- [25] P. M. Chesler and D. Teaney (2011), [hep-ph/1112.6196](#).
- [26] M. P. Heller, R. A. Janik, and P. Witaszczyk (2011), [hep-th/1103.3452](#).
- [27] F. Pretorius, *Class.Quant.Grav.* **22**, 425 (2005), [gr-qc/0407110](#).
- [28] F. Pretorius, *Phys.Rev.Lett.* **95**, 121101 (2005), [gr-qc/0507014](#).
- [29] H. Bantilan, F. Pretorius, and S. S. Gubser, *Phys.Rev.* **D85**, 084038 (2012), [hep-th/1201.2132](#).
- [30] S. Gubser, *Phys. Rev. D* **82** **D 82** (2010).
- [31] S. S. Gubser and A. Yarom, *Nucl. Phys.* **B846**, 469 (2011), [hep-th/1012.1314](#).
- [32] P. Staig and E. Shuryak, *Phys. Rev.* **C84**, 044912 (2011), [nucl-th/1105.0676](#).
- [33] P. Staig and E. Shuryak, *J. Phys.* **G38**, 124039 (2011), [hep-ph/1106.3243](#).
- [34] A. Ishibashi and R. M. Wald, *Class.Quant.Grav.* **21**, 2981 (2004), [hep-th/0402184](#).
- [35] H. Nastase (2005), [hep-th/0501068v3](#).
- [36] I. A. *et al.* [BRAHMS Collaboration], *Nucl. Phys.* **A 757**, 1 (2005).
- [37] K. A. *et al.* [PHENIX Collaboration], *Nucl. Phys.* **A 757**, 184 (2005).
- [38] B. B. *et al.*, *Nucl. Phys.* **A 757**, 28 (2005).
- [39] J. A. *et al.* [STAR Collaboration], *Nucl. Phys.* **A 757**, 102 (2005).
- [40] J. Bjorken, *Phys. Rev. D* **27**, 140 (1983).
- [41] D. Garfinkle, APS Meeting Abstracts pp. 12004–+ (2002).

- [42] L. Lindblom, M. A. Scheel, L. E. Kidder, R. Owen, and O. Rinne, *Class.Quant.Grav.* **23**, S447 (2006), [gr-qc/0512093](#).
- [43] H. Friedrich, *Communications in Mathematical Physics* **100**, 525 (1985).
- [44] C. Gundlach, J. M. Martin-Garcia, G. Calabrese, and I. Hinder, *Class. Quant. Grav.* **22**, 3767 (2005), [gr-qc/0504114](#).
- [45] R. L. Arnowitt, S. Deser, and C. W. Misner (1962), *gravitation: an introduction to current research*, Louis Witten ed. (Wiley 1962), chapter 7, pp 227-265, [gr-qc/0405109](#).
- [46] E.ourgoulhon, *J. Phys. Conf. Ser.* **91**, 012001 (2007), [gr-qc/0704.0149](#).
- [47] M. Henneaux and C. Teitelboim, *Commun. Math. Phys.* **98**, 391 (1985).
- [48] C. Fefferman and C. R. Graham, in *Élie Cartan et les mathématiques d'aujourd'hui, the mathematical heritage of Élie Cartan, Sémin. Lyon 1984, Astérisque, Numéro Hors Sér., 95–116* (1985).
- [49] D. Garfinkle and G. C. Duncan, *Phys. Rev.* **D63**, 044011 (2001), [gr-qc/0006073](#).
- [50] V. E. Hubeny, S. Minwalla, and M. Rangamani (2011), [hep-th/1107.5780](#).
- [51] H. Stephani, D. Kramer, M. Maccallum, C. Hoenselaers, and E. Herlt, *Exact Solutions of Einstein's Field Equations* (Cambridge University Press, Cambridge, UK, 2003).
- [52] H. Kreiss and J. Oliger, *Global Atmospheric Research Program Publication* **10** (1973).
- [53] G. Calabrese, L. Lehner, O. Reula, O. Sarbach, and M. Tiglio, *Class.Quant.Grav.* **21**, 5735 (2004), [gr-qc/0308007](#).
- [54] J. D. Brown and J. W. York, Jr., *Phys. Rev.* **D47**, 1407 (1993), [gr-qc/9209012](#).
- [55] V. Balasubramanian and P. Kraus, *Commun. Math. Phys.* **208**, 413 (1999), [hep-th/9902121](#).
- [56] R. Emparan (2011), [hep-th/1106.2021](#).
- [57] R. Loganayagam, *JHEP* **05**, 087 (2008), [hep-ph/0801.3701](#).
- [58] H. P. Pfeiffer and J. W. York, Jr., *Phys. Rev. Lett.* **95**, 091101 (2005), [gr-qc/0504142](#).
- [59] J. Jost, *Partial differential equations*, Graduate texts in mathematics (Springer, 2002).
- [60] G. T. Horowitz and V. E. Hubeny, *Phys. Rev.* **D62**, 024027 (2000), [hep-th/9909056](#).

- [61] V. Cardoso, R. Konoplya, and J. P. S. Lemos, Phys. Rev. **D68**, 044024 (2003), [gr-qc/0305037](#).
- [62] P. K. Kovtun and A. O. Starinets, Phys. Rev. **D72**, 086009 (2005), [hep-th/0506184](#).
- [63] R. A. Janik and R. B. Peschanski, Phys. Rev. **D74**, 046007 (2006), [hep-th/0606149](#).
- [64] D. Teaney, Phys. Rev. **D74**, 045025 (2006), [hep-ph/0602044](#).
- [65] J. J. Friess, S. S. Gubser, G. Michalogiorgakis, and S. S. Pufu, JHEP **0704**, 080 (2007), [hep-th/0611005](#).
- [66] E. Berti, V. Cardoso, and A. O. Starinets, Class. Quant. Grav. **26**, 163001 (2009), [gr-qc/0905.2975](#).
- [67] J. Avery, *Hyperspherical Harmonics and Generalized Sturmians* (Kluwer Academic Publishers, Dordrecht, Netherlands, 2000).
- [68] H. Kodama and A. Ishibashi, Prog. Theor. Phys. **110**, 701 (2003), [hep-th/0305147](#).
- [69] L. D. Landau, Izv. Akad. Nauk SSSR Ser. Fiz. **17**, 51 (1953).
- [70] I. M. Khalatnikov, ZhETF **27**, 529 (1954).
- [71] L. Lehner and F. Pretorius, Phys.Rev.Lett. **105**, 101102 (2010), [hep-th/1006.5960](#).
- [72] P. Steinberg, Acta Phys. Hung. **A24**, 51 (2005), [nucl-ex/0405022](#).
- [73] S. de Haro, S. N. Solodukhin, and K. Skenderis, Commun.Math.Phys. **217**, 595 (2001), [hep-th/0002230](#).
- [74] P. Breitenlohner and D. Z. Freedman, Phys. Lett. **B115**, 197 (1982).